UNIVERSIDADE D
COIMBRA

António Pedro de Sousa Monteiro

Hydrothermal Deposition of Antimony Chalcogenide Thin Films for Planar Heterojunction Solar Cells

VOLUME 1

Dissertação no âmbito do Mestrado em Engenharia Física orientada pelo Professor Doutor Paulo Alexandre Franco Ponte Fernandes e pelo Professor Doutor Rui César do Espírito Santo Vilão e apresentada ao Departamento de Física da Faculdade de Ciências e Tecnologia da Universidade de Coimbra.

Setembro de 2023

Hydrothermal Deposition of Antimony Chalcogenide Thin Films for Planar Heterojunction Solar Cells

Host Institution Supervisor:

Paulo Alexandre Franco Ponte Fernandes

University Supervisor:

Rui César do Espírito Santo Vilão

Jury:

Prof. Dr. Manuela Ramos Marques da Silva

Prof. Dr. Maria Helena Almeida Vieira Alberto

Prof. Dr. Paulo Alexandre Franco Ponte Fernandes

Dissertation submitted in partial fulfillment for the degree of Master of Science in Engineering Physics.

Coimbra, September 2023

Agradecimentos

Gostaria de começar por agradecer ao Prof. Dr. Pedro Salomé e à Dr. Jennifer Teixeira por me receberem em Braga e me proporcionarem a oportunidade de trabalhar em instalações de topo, e de vivenciar um ambiente tão enriquecedor e multicultural. Agradeço a toda a equipa do NOA pelos momentos de aprendizagem, mas, sobretudo, pela companhia e convivência, dentro e fora do INL. Em particular, ao Vitor, que, mesmo não sendo meu orientador, me acompanhou desde o início e, de forma incansável, garantiu que tinha todas as condições para realizar este trabalho.

Ao Prof. Dr. Paulo Fernandes, cujo conhecimento e conselhos foram sempre transmitidos com um sorriso, e ao Prof. Dr. Rui Vilão, que me introduziu ao mundo dos semicondutores de filmes finos.

À minha família agradeço profundamente, por me guiar ao longo deste percurso formativo. Em particular, aos meus pais e avós, a quem devo a minha educação, sem nunca ter faltado nada.

Queria deixar uma palavra aos meus amigos, por serem uma fonte de felicidade e companheirismo ao longo destes anos, pelos cafés, saídas à noite, jantares, e por todas as boas memórias que me deixaram.

Finalmente, um beijinho à Joana, que me acompanhou nestes sinuosos cinco anos de faculdade, e cujos obstáculos ultrapassámos, sempre, lado a lado.

Resumo

Os calcogenetos de antimónio, $Sb_2(S_{1-x},Se_x)_3$, são ambientalmente benignos e económicos. A sua estrutura cristalina quasi-unidimensional e características optoeletrónicas vantajosas tornam estes materiais desejáveis, enquanto camada absorvente em células solares de filmes finos, baseadas em arquiteturas de superstrato. Recentemente, o desenvolvimento de um simples método de deposição hidrotermal tem demonstrado capacidade para produzir filmes de calcogeneto de antimónio de alta qualidade, resultando numa eficiência de conversão de energia de ponta de 10.75% para células solares que utilizam um substrato de CdS. Após a deposição, um tratamento químico e uma etapa de recozimento são comummente usados para melhorar a cristalinidade e passivar defeitos da camada absorvente, sendo frequentemente objeto de investigação. Neste trabalho, o processo de fabricação de filmes de $Sb_2(S,Se)_3$ preparados no grupo Nanofabrication for Optoelectronic and Energy Applications (NOEA) do Laboratório Internacional Ibérico de Nanotecnologia (INL) é consolidado, e serve como ponto de partida para estudos futuros. Nomeadamente, o processo de recozimento é otimizado para uma temperatura de 350°C, produzindo filmes cristalinos e livres de contaminantes, garantindo igualmente uma orientação preferencial dos cristalitos. Além disso, um tratamento químico com NaF realizado antes da etapa de recozimento, revelou que a solução alcalina pode promover um gradiente de composição S/Se mais suave ao remover as camadas superiores dos filmes ricas em enxofre, o que tem sido associado na literatura a uma favorecida extração de portadores de carga. Por fim, verificou-se que um substrato de TiO_2 não tóxico é inadequado para a nucleação hidrotermal do $Sb_2(S,Se)_3$, devido à falta de uma ligação química entre as duas camadas, resultando em filmes absorventes com baixa compacidade e células solares com eficiências abaixo de 0.38%.

Palavras-chave: Filmes finos, Células solares, $Sb_2(S,Se)_3$, Deposição hidrotermal, Recozimento

Abstract

Antimony chalcogenides, $Sb_2(S_{1-x},Se_x)_3$, are environmentally benign and cost effective. Their quasi-one-dimensional crystal structure and advantageous optoelectronic characteristics renders them as an emerging technology for the absorber layer in superstrate thin film solar cells. Recently, a simple solution-based hydrothermal deposition method has been shown to produce high quality antimony chalcogenide films, resulting in a state-of-the-art power conversion efficiency of 10.75% for solar cells based on a CdS substrate. Following the deposition, a chemical treatment and an annealing step are frequently used to enhance crystallinity and passivate defects of the absorber layer, and are often the subject of investigation. In this work, the fabrication process of $Sb_2(S, Se)_3$ films prepared at the Nanofabrication for Optoelectronic and Energy Applications (NOEA) group of the International Iberian Nanotechnology Laboratory (INL) is consolidated, and serves as a stepping stone for further studies. Namely, the annealing process is optimized for a temperature of 350°C, by obtaining contaminant-free and crystalline films, while guaranteeing preferential crystallite orientation. Furthermore, a NaF chemical treatment employed prior to the annealing step, revealed that the alkaline solution can promote a mild S/Se composition gradient by etching the sulfur-rich top layers of the films, which has been associated with increased charge extraction. Finally, a non-toxic TiO_2 substrate was deemed inadequate for the hydrothermal nucleation of the $Sb_2(S, Se)_3$ material due to the lack of a chemical bridge between the two layers, resulting in absorber films with low compactness, and prepared solar cells that could not surpass the 0.38% efficiency mark.

Keywords: Thin films, Solar cells, $Sb_2(S, Se)_3$, Hydrothermal deposition, Annealing

Contents

List of Acronyms

INL	International Iberian Nanotechnology Laboratory
NOEA	Nanofabrication for Optoelectronic and Energy Applications
PV	Photovoltaic
BIPV	Building Integrated Photovoltaic
SQ	Shockley-Queisser
PCE	Power Conversion Efficiency
FF	Fill Factor
GB	Grain Boundary
ETL	Electron Transport Layer
HTL	Hole Transport Layer
SLG	Soda Lime Glass
VTD	Vacuum Transport Deposition
TE	Thermal Evaporation
CSS	Close-Space Sublimation
PDT	Post-Deposition Treatment
SIMS	Secondary-Ion Mass Spectroscopy
RTP	Rapid Thermal Processing
UVO	Ultraviolet Ozone
TCO	Transparent Conductive Oxide

XRD	X-Ray Diffraction
FWHM	Full Width at Half Maximum
SEM	Scanning Electron Microscopy
EDS	Electron X-ray Dispersive Spectroscopy
XPS	X-Ray Photoelectron Spectroscopy
UPS	Ultraviolet Photoelectron Spectroscopy
REELS	Reflection Electron Energy Loss
UV-Vis-NIR	Ultraviolet-Visible-Near Infrared
EQE	External Quantum Efficiency
CBD	Chemical Bath Deposition

List of Figures

List of Tables

1 Introduction

1.1 Renewable Energy Sources and Photovoltaic Production

Concerns about climate change, paired with the immediate need for cheap, non-polluting, renewable energy, demand an increased effort by the scientific community to develop solutions that can quickly reach the market. Furthermore, the energetic crisis, aggravated by factors such as the Russian-Ukrainian conflict and subsequent inflation of oil and gas prices, has alerted people to the need for alternative energy sources.

Reports show that the total energy generation from renewable sources accounted for 348 GW in 2022, with investment in renewables growing by 17.2% [1]. In the last decade, the share of renewable energy production has seen an increase of 8.6 percentual points [1] (figure 1.1). Nonetheless, most of the total energy consumed each year still originates from non-renewable sources, and renewable energy production must triple to be on track with carbon neutrality goals.

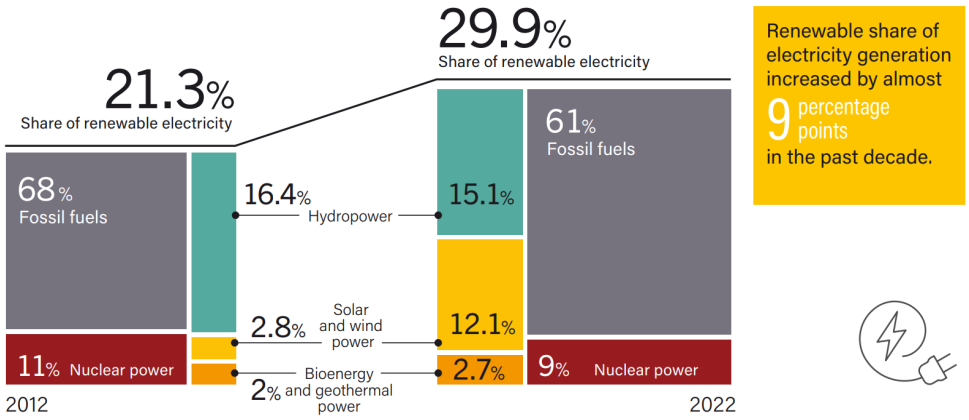

Figure 1.1: Comparison of renewable energy share between 2011 and 2021 (from [1]).

The process of electricity generation through photovoltaic (PV) technology, irrespective of the specific technology employed, is an emissions-free process. Nevertheless, there are potential

environmental, health, and safety concerns associated with the manufacturing stages involved in the fabrication of solar cells and PV modules [2]. In 2021, global solar photovoltaic (PV) capacity accounted for a total of 942 gigawatts (GW) of DC power. By the end of 2022, total production reached a maximum of 1185 GW (figure 1.2), the largest annual capacity increase ever recorded. Solar PV accounted for the bulk of renewable energy production rise, making it the fastest-growing energy technology [1]. In 2022, new solar PV installations in Asia surpassed all other regions for the tenth year in a row, accounting for 64% of the global added capacity, with China possessing an 80% stake of the global manufacturing of solar panels.

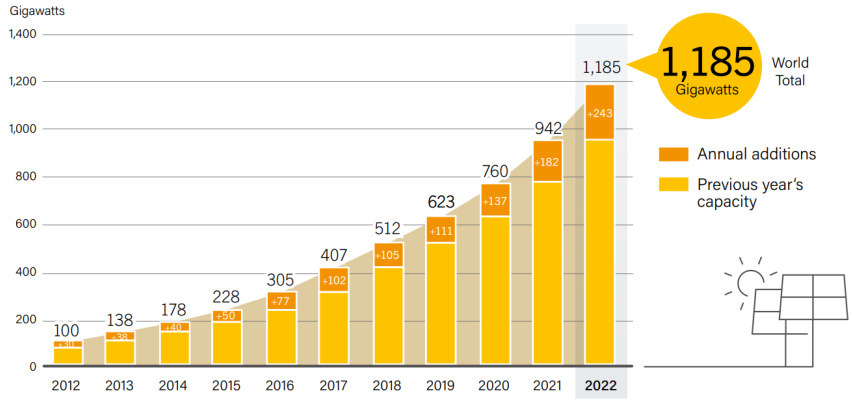

Figure 1.2: Evolution of solar PV global capacity (from [1]).

Nonetheless, there has been a recent increase of about 57% in PV module costs [1], which had been previously declining over the years. This rise in cost was attributed to several factors, including a shortage of silicon and an increase in shipping container expenses from China, the leading module producer globally. Thus, continuous scientific investment in the PV industry is needed, in order to maintain market competitiveness and further push the global solar PV capacity.

1.2 An Overview on Photovoltaic Technologies

First-generation solar cells are made of crystalline silicon (c-Si), both mono and polycrystalline. By 2021, 95% of the marketable PV technology was crystalline silicon-based [3]. Despite its popularity and high state-of-the-art power conversion efficiency (PCE) of 26.8% [3], silicon-based wafers are expensive to build, mostly due to the amount of material used. To maximize industrial competitiveness, two approaches must be followed: to decrease manufacturing costs by using less material and to develop new ways of increasing the efficiency of the cells [4].

The decreased thickness of thin film solar cells represents an economical advantage, while still

being able to obtain decent efficiencies. Second-generation solar cells, such as Copper Indium Gallium Selenide (CIGS), Cadmium Telluride (CdTe) and amorphous silicon (a-Si) are the most widely commercialized thin film solar cells, even though they account for only 5% of the total PV market share (figure 1.3). Their direct bandgap allows for the use of micrometer layers, even enabling the use of these cells in flexible substrates and building integrated photovoltaics (BIPV) [4]. Due to improvements in material engineering and the introduction of novel device architectures, these cells have achieved record efficiencies of 23.4% [5], 22.1% [6] and 10.2% [7] for CIGS, CdTe and a-Si planar solar cells, respectively.

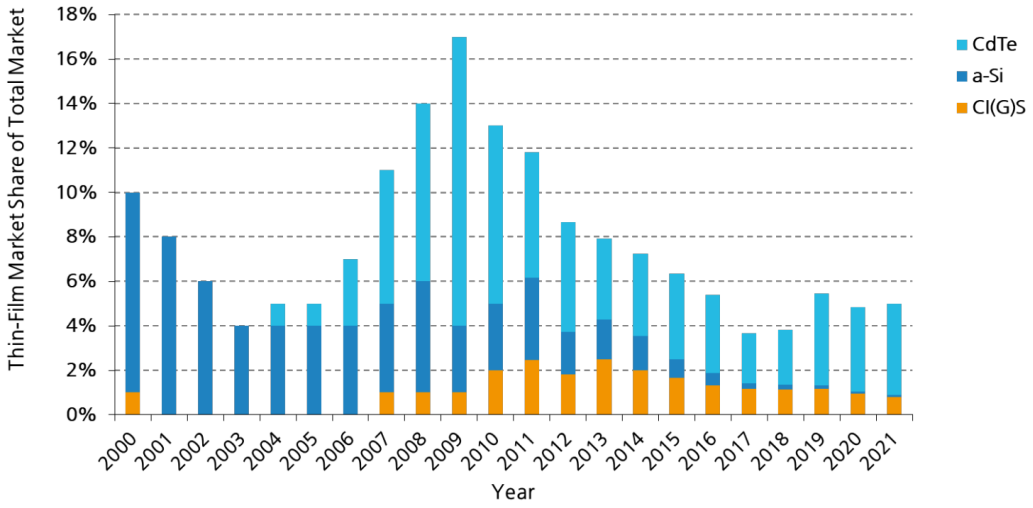

Figure 1.3: Percentage of total global PV production per thin film technology (from [3])

However, the high price and rarity of In and Ga materials, as well as the toxicity of Cd, may limit these technologies in reaching very large-scale use (multi-terawatt production) [8]. Hybrid organic-inorganic methylammonium lead iodide (MAPI) solar cells have emerged in recent years, presenting great potential in terms of performance. Nonetheless, even though it offers high efficiencies for a low-production cost, this technology raises concerns in terms of module reliability, and still relies mostly on the use of toxic materials, such as lead. Thus, other materials composed of environmentally friendly and abundant elements, are needed in order to diversify the offer of cheap, efficient and reliable solar cell technologies. Table 1.1 presents some of the characteristics of different thin film solar cell technologies.

Table 1.1: Characteristics of PV devices for established solar cell technologies, which are important factors to consider when scalling to multi-terawatt production (from [8])

PV technology	Module cost	Module efficiency	Module reliability	Capital expenditures	Environmental concerns	Elemental abundance
Si	Low	High	Good	High	No	High
CdTe	Low	High	Good	Medium	Yes	Low
CIGS	Medium	High	Good	Medium	No	Low
MAPI	Low	High	Bad	Low	Yes	Medium

Many metal sulfide and selenide materials have emerged as new earth-abundant, non-toxic options. Among them, antimony-based chalcogenides, such as Sb_2S_3, Sb_2Se_3, and, more recently, the alloy $Sb_2(S, Se)_3$, have shown increasing potential in PV application, due to their stability, ease of manufacturing, and structural and optoelectronic properties [9]. These characteristics will be further discussed in Chapter 2.

1.3 Introduction to Photovoltaic Cells

Generally speaking, photovoltaic cells convert photonic energy into a DC current, based on semiconductor technology. Usually, a solar cell can be seen as a p-n junction formed by hole-rich (p-doped) and electron-rich (n-doped) semiconductor materials. Due to charge diffusion across the junction, a charge carrier-free region (depletion region) will form in the much thicker p-type layer (called the absorber layer), resulting in an electric field that opposes further diffusion. Photons reaching this depleted region will generate electron-hole pairs by the photoelectric effect, provided that the photon energy is larger than the bandgap of the semiconductor material. The charge carriers will then be separated by the built-in electric field of the p-n junction, resulting in a flow of charges and, consequently, a measurable power output.

In an ideal case, a solar cell can be modeled as a diode in parallel with a current source, representing the photogenerated current, I_{ph} (figure 1.4). Because each photon can only produce one electron-hole pair, the photogenerated current will be proportional to the intensity of the incident radiation.

The diode current, I_D, represents the voltage-dependent current lost to charge recombination, while low shunt resistances, R_{sh}, are usually due to defects in the cell structure. By analyzing the circuit in figure 1.4 and using Kirchhoff's laws, we can conclude that the output current, I, is given by:

$$I = I_{ph} - I_D - I_{sh} \tag{1.1}$$

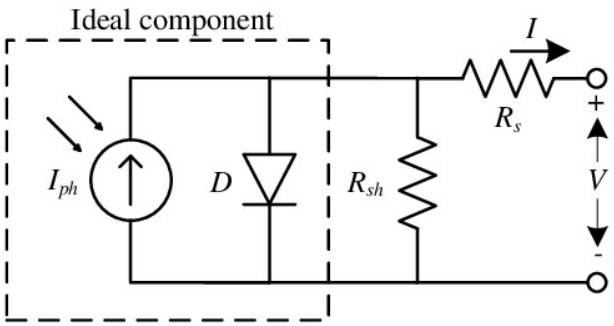

Figure 1.4: Single diode equivalent circuit of a PV cell (from [10]).

By using the ideal diode equation, the expression from 1.1 becomes:

$$I = I_{ph} - I_S \left[\exp\left(\frac{q\,(V + IR_s)}{nkT} \right) - 1 \right] - I_{sh} \tag{1.2}$$

where I_S is the dark saturation current, V is the output voltage, $V_D = V + IR_s$ is the voltage through the diode, n is the ideality factor, q is the charge of the electron, k is the Boltzmann constant and $I_{sh} = \frac{V+IR_s}{R_{sh}}$ is the current lost to shunt resistances. I_S is the current that flows in the absence of light and under a reverse bias voltage, and originates from the intrinsic carrier concentration and recombination rate of the junction [11].

1.3.1 I-V Curve Parameters

The fundamental features of a solar cell are encapsulated in its current versus voltage (I-V) relationship, which can also be represented with the current density in the y axis (J-V curve). In the dark, the cell will act as a diode, and a dark I-V measurement produces the characteristic diode curve. Illuminating the cell will produce a shift to the curve, which will be proportional to the incident light's power, as can be seen in figure 1.5.

The key parameters that characterize the performance of a solar cell can be directly found in the I-V curve and are the open-circuit voltage (V_{OC}), the short-circuit current (I_{SC}), the maximum output power (P_{mp}) and the fill factor (FF). These electrical parameters are used to determine the power conversion efficiency (η) of the solar cell [11].

- **Open-circuit voltage (V_{OC})**: This is the voltage obtained when the load of the solar cell is an open circuit and the output current is zero (I = 0). From equation 1.2, and neglecting the influence of shunt currents, we can conclude that:

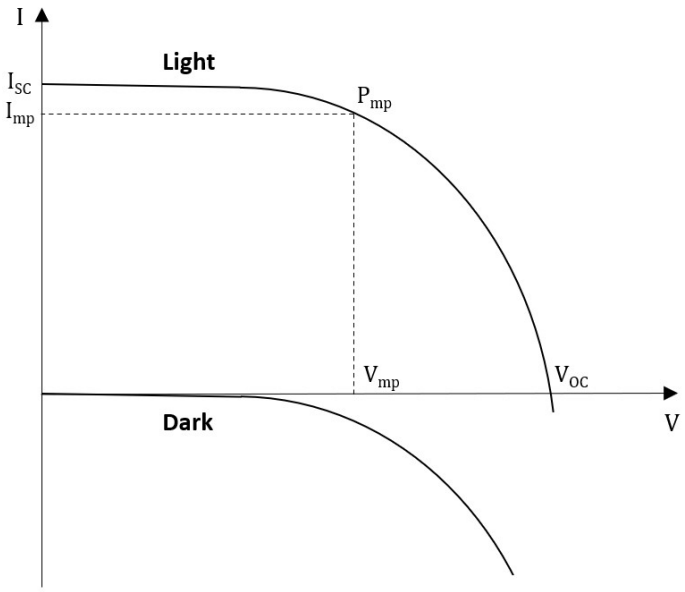

Figure 1.5: I-V curve of a solar cell in the dark and under illumination.

$$V_{OC} = \frac{k_B T}{e} \ln\left(\frac{I_{ph}}{I_S} + 1\right) \tag{1.3}$$

- **Short-circuit current ($\mathbf{I}_{SC}$)**: At low voltages, the diode current from equation 1.1 is negligible, and the produced current corresponds to the short-circuit current, which is the maximum measured output current. For shuntless cells, $\mathrm{I}_{SC} = \mathrm{I}_{ph}$.

- **Peak output power ($\mathbf{P}_{mp}$)**: This is the point of the curve of maximum produced power, where $\mathrm{V} = \mathrm{V}_{mp}$ and $\mathrm{I} = \mathrm{I}_{mp}$. The rectangle defined by equation 1.4 has the largest area for any point in the curve.

$$P_{mp} = V_{mp} \cdot I_{mp} \tag{1.4}$$

- **Fill-factor (FF)**: This parameter is defined as the ratio between the peak power and the product of I_{SC} and V_{OC} (equation 1.5). The fill factor can be seen as the ratio of areas of the rectangles formed by $\mathrm{I}_{mp} \cdot \mathrm{V}_{mp}$ and $\mathrm{I}_{SC} \cdot \mathrm{V}_{OC}$, hence, always less than one. In physical terms, it gives us information on the quality of the interfaces of the solar cell.

$$FF = \frac{V_{mp} \cdot I_{mp}}{V_{OC} \cdot I_{SC}} \tag{1.5}$$

- **Power conversion efficiency (η)**: Arguably the most important parameter to characterize the performance of a photovoltaic device, the efficiency of a cell is defined as the ratio between the maximum output power and the light incident power (equation 1.6)

$$\eta = \frac{P_{\mathrm{mp}}}{P_{\mathrm{in}}} = \frac{V_{\mathrm{OC}} \cdot I_{\mathrm{SC}} \cdot FF}{P_{\mathrm{in}}} \tag{1.6}$$

As we can conclude from equation 1.6, high I_{SC} and V_{OC} are paramount, since they are characteristics of efficient solar devices. Finally, a "square" I-V curve is desired and this property is quantified in the FF parameter. The introduction of non-ideal components, such as series and shunt parasitic resistances, will have a detrimental impact on the performance of the solar cell, as can be seen in equation 1.2. In fact, these components are caused by structural defects and poor contacts, being mainly reflected in a FF decrease, as demonstrated in figure 1.6, affecting the "squareness" of the IV curve [11].

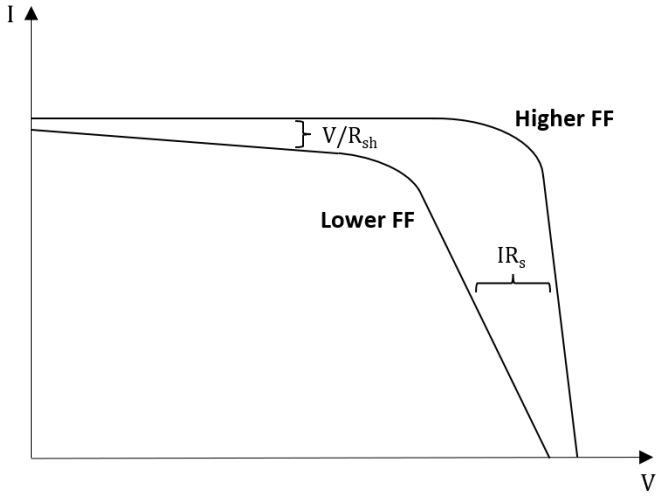

Figure 1.6: Effect of parasitic series and shunt resistances on the I-V curve of solar cells.

1.4 Dissertation Structure and Objectives

This thesis will focus on the study of the $Sb_2(S, Se)_3$ compound, as it possesses advantageous intermediate physical properties between those of Sb_2S_3 and Sb_2Se_3 materials. In particular, we will focus on improving the preparation process of $Sb_2(S, Se)_3$ thin films by a simple hydrothermal method, while investigating not only the influence of post-deposition parameters such as annealing temperature and chemical treatments of the absorber layer, but also the impact of the substrate type on the properties of the final films. Finally, complete $Sb_2(S, Se)_3$-based solar devices will be tested.

In terms of thesis structure, Chapter 2 will present a brief overview on the current literature, by addressing the characteristics and reported preparation methods of $Sb_2(S, Se)_3$ materials for PV applications, and focusing on the here-employed hydrothermal synthesis method. Chapter 3

briefly describes the experimental methods and characterization techniques employed throughout this thesis. Divided in 6 sections, Chapter 4 exhibits some of the obtained results of the study of different parameters of the fabrication of $Sb_2(S, Se)_3$ thin films, while discussing those results on the basis of previous literature. Finally, Chapter 5 presents the conclusions of this work and finishes with some suggestions for further studies.

2 State of the Art

2.1 Antimony Chalcogenide Absorber Materials

Antimony chalcogenides ($Sb_2(S_{1-x}, Se_x)_3$) can be regarded as quasi-binary semiconductors, formed by the solid solution of the isomorphous and isostructural Sb_2Se_3 and Sb_2S_3, which are members of the family of the inorganic binary V_2-VI_3 compounds [12]. $Sb_2(S, Se)_3$ crystallizes in an orthorhombic structure and can be found naturally in the form of the mineral stibnite. Its structure is formed by parallel stacks of $(Sb_4(S, Se)_6)_n$ quasi 1D ribbons (figure 2.1) [13, 14].

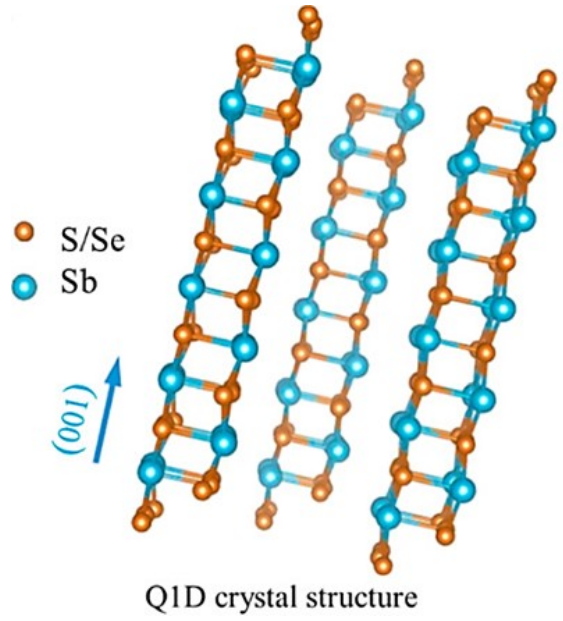

Figure 2.1: $Sb_2(S, Se)_3$ crystal structure with stacks of $(Sb_4(S, Se)_6)_n$ ribbons along the c-axis ([001] direction) (from [15]).

In recent years, antimony chalcogenides have garnered significant attention as a light absorber material for use in photovoltaic (PV) applications. For once, $Sb_2(S, Se)_3$ compounds have benign environmental characteristics: the abundance of Sb, S, and Se elements in the Earth's crust (0.2, 520 and 0.05 ppm, respectively) [13, 15, 16], combined with its low toxicity, are advantageous

properties when compared to more traditional thin film solar cell technologies [9]. Furthermore, $Sb_2(S,Se)_3$ materials have excellent optoelectronic characteristics, such as a high absorption coefficient in the visible region ($\alpha \approx 10^5$ cm^{-1}) and a suitable band gap ($1.1 - 1.7$ eV) that can be tuned by changing the S and Se concentrations [17]. In fact, because Sb_2Se_3 and Sb_2S_3 present sub-optimal bandgap values, adjusting the S and Se composition allows tuning of the bandgap towards the optimal 1.34 eV for heterojunction solar cells at the standard AM1.5G spectrum [18], as per the Shockley-Queisser (SQ) limit. Due to their high absorption coefficient, antimony chalcogenide films with only 800 nm of thickness are sufficient to absorb photons in the 400 to 1000 nm range, the ideal spectral range for photovoltaic conversion [19]. Additionally, electron and hole mobility can benefit from growing films with preferential crystallographic orientation. Table 2.1 summarizes some of the physical properties of antimony triselenide and antimony trisulfide.

Table 2.1: Physical properties of Sb_2Se_3 and Sb_2S_3 (Adapted from [15]).

Property	Symbol	Sb_2Se_3 value	Sb_2S_3 value
Lattice parameters (Å)	a	11.6330	11.2285
	b	11.7800	11.3107
	c	3.9850	3.8363
Density (g cm^{-3})	ρ	5.84	4.63
Bandgap (eV)	$E_{g,d}$ (direct)	1.17	1.84
	$E_{g,i}$ (indirect)	1.03	1.76
Absorption coefficient (cm^{-1})	α	$> 10^5$	10^4 - 10^5
Minority-carrier lifetime (ns)	τ_e	67	23
Electron and hole mobility (cm^2·V^{-1}·s^{-1})	μ_e	15	9.8
	μ_h	42	10
Melting point (K)	T	885	823

The $Sb_2(S,Se)_3$ structure consists of quasi 1D (S,Se)-Sb-(S,Se) ribbons along the [001] crystallographic direction. This one-dimensional crystal structure is one of the major advantages of antimony chalcogenides: because all the atoms at the edge of these ribbons are saturated (highlighted as the red spheres in figure 2.2a), the bonds within the ribbons are stronger than the bonds between the ribbons (weak (S,Se)-(S,Se) bonds). This intrinsic property of antimony chalcogenide crystals ensures that no recombination loss occurs at the grain boundaries (GBs) once the ribbons are vertically oriented in relation to the substrate, promoting anisotropic carrier transport. On the other hand, 3D crystals, such as CdTe, have dangling bonds at GBs (figure 2.2b), which may act as traps, promoting recombination losses of the light generated charge

carriers [20]. For this reason, growing $Sb_2(S, Se)_3$ films with a columnar crystal structure, this is, along a [hk1] direction, is preferential for optimized charge transport and collection.

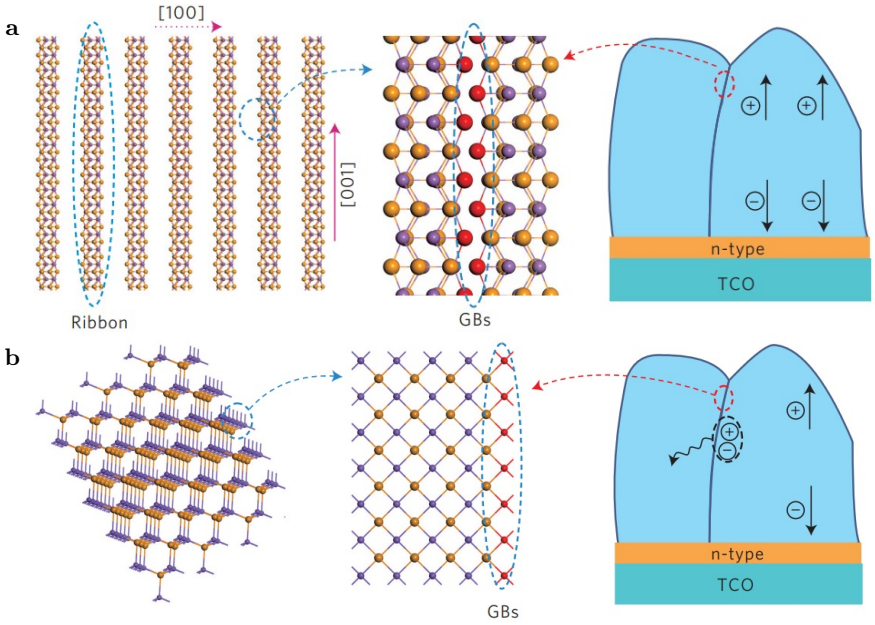

Figure 2.2: **a.** 1D crystal structure of antimony chalcogenides promotes anisotropic carrier transport in the [001] direction due to naturally passivated GBs. **b.** 3D crystal structure of CdTe has dangling bonds at GBs, which causes recombination losses due to defects (from [20]).

The 1D anisotropic characteristics of antimony chalcogenide materials pose a challenge in realizing their full potential, as achieving columnar structure in film growth is essential. Typical crystal planes in antimony chalcogenides include the (120), (211) and (221) planes. Films oriented along the [211] direction have been demonstrated to possess superior performance owing to the angle of 52.6° between the [211]-oriented ribbon and the substrate, resulting in a more vertical structure. On the other hand, [221]-oriented ribbons present a less optimal 46.1° angle (note that [hkl]-oriented direction refers to the normal direction to the (hkl) plane) [21]. Figure 2.3 shows some of the potential orientations that antimony chalcogenide grains can take relative to the substrate. Naturally, a flat [120]-oriented growth is undesirable as the gap between ribbons will pose as a potential barrier and recombination center for charge carriers [21].

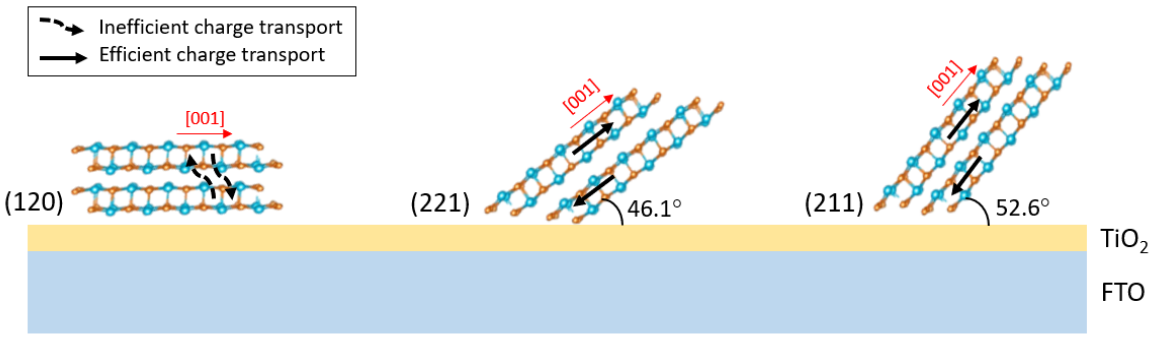

Figure 2.3: Representation of antimony chalcogenide crystal growth along the [120], [221] and [211] orientation with respect to the substrate (Adapted from [21]).

2.2 $Sb_2(S, Se)_3$ Thin Film Solar Cells

The reduced thickness of thin film solar cells presents itself as an economical advantage. Nonetheless, because of their low thickness, these cells require a substrate for mechanical support. When the layers of the cell are deposited using a bottom-up approach, they are said to be arranged in a substrate configuration. In this layout, the deposition starts with the back contact and ends with the top transparent electrode layer on the light-exposed side. When the layers are deposited with a top-down approach (figure 2.4), starting from the light-exposed side and ending with the back contact, the cell is in a superstrate configuration. Consequently, to allow the passage of light in the superstrate configuration, only highly transparent substrates are permitted [9].

Unlike the more traditional p-n architecture of other thin film solar cells, antimony chalcogenide cells usually present a p-i-n or n-i-p structure, adopting the architecture used in perovskite cell technology. In this structure, the (almost) intrinsic semiconductor used as the absorber layer is placed between a n-type electron transport layer (ETL) and a p-type hole transport layer (HTL) [22]. Where the more traditional architecture of thin film solar cells, such as CIGS and CdTe, relies on the formation of a built-in electric field at the p-n junction to enable the separation of charge carriers, the high-conductivity ETL and HTL in p-i-n and n-i-p structures allow for the extraction of photogenerated electrons and holes, respectively. Proper energy band alignment of the ETL and HTL with the absorber material is crucial, as it ensures that charge carriers are efficiently transferred to the appropriate transport layers. Particularly, the conduction band minimum of the ETL should align with the conduction band minimum of the absorber, while the valence band maximum of the HTL should align with the valence band maximum of

the absorber [23]. In the case of antimony chalcogenide solar cells, the superstrate n-i-p architecture is more commonly used. This structure implies that the ETL layer is deposited first onto the transparent substrate [24]. Figure 2.4 presents the typical structure of a $Sb_2(S, Se)_3$ planar heterojunction thin film solar cell.

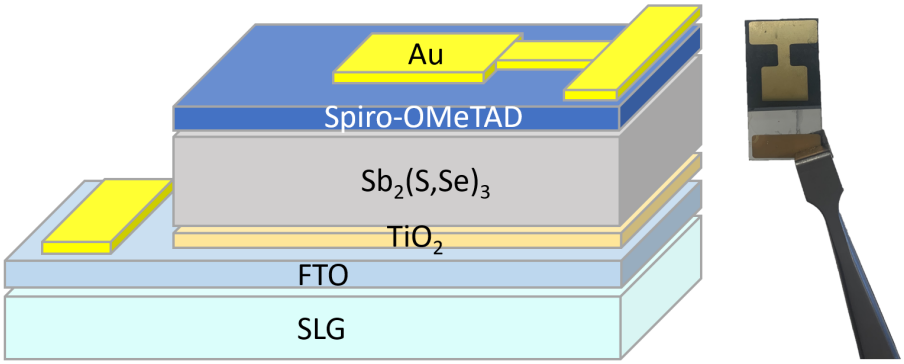

Figure 2.4: Schematics and image of the (superstrate) $TiO_2/Sb_2(S, Se)_3$ planar heterojunction thin film solar cell produced at INL via the hydrothermal method.

Starting from the top layer in figure 2.4, the main aspects of each layer are the following:

- **Back contact (Au):** The metallic back contact transports the photogenerated holes outside the cell. The wide use of gold as the back contact stems from two main characteristics: I) it forms a low resistivity ohmic contact with the hole-transport layer (HTL) due to its deep work function (≈5.1 eV), allowing for efficient hole removal; II) it is a chemically inert, non-reactive metal, and, for that reason, does not undergo any detrimental interfacial reactions with the HTL [25]. Nonetheless, using gold as the back contact in solar cells is only justifiable on a small scale, as it is an expensive material. Consequently, other alternatives, such as graphite combined with silver [26], nickel and copper [25] have been used.

- **Hole-Transport Layer (Spiro-OMeTAD):** Collection performance of photogenerated carriers can be enhanced by implementing a hole-transport layer (HTL) as an intermediary between the absorber and back-contact. The HTL can reduce back contact resistance [27] while facilitating hole extraction and blocking electron flux [28]. 2,2',7,7'-Tetrakis[N,N-di(4-methoxyphenyl)amino]-9,9'-spirobifluorene (Spiro-OMeTAD) is an organic semiconductor and remains one of the most popular HTL materials because of its high hole conductivity and ease of processing [29]. Nonetheless, this material isn't suitable for large-scale

commercial applications, since it is prone to self-degradation, mainly at high temperatures, hindering the long-term stability of solar cells [30]. Furthermore, Spiro-OMeTAD is 10 times more expensive than gold or platinum, making it commercially nonviable.

- **Absorber layer ($Sb_2(S, Se)_3$):** As the name says, this is the layer that absorbs the highest number of photons, exciting electrons into the conduction band (and holes to the valence band). For this reason, the material that forms the absorber layer must guarantee a bandgap that matches the photon-rich region of the solar spectrum. Furthermore, the layer must be sufficiently thick to absorb most of the light reaching the cell. As previously mentioned, $Sb_2(S, Se)_3$ semiconductors have a high absorption coefficient in the visible region ($\approx 10^5$ cm^{-1}) and a suitable band gap (1.1 - 1.7 eV), as well as good minority carrier lifetime (see table 2.1). While its almost 1D crystal structure presents new opportunities for the fabrication of cells with low recombination losses at GBs, the dependence of the transport properties on the anisotropic physical specificities of antimony chalcogenides also adds new challenges for the deposition of this type of structures [9].

- **Electron Transport Layer (TiO_2):** The electron transport layer (ETL) is the n-type semiconductor that facilitates electron transfer from the absorber to the transparent electrode. To avoid carrier losses due to interfacial defects, proper ETL/absorber interface engineering is required, namely focusing on adequate energy band alignment and lattice matching. Currently, CdS is the most commonly used ETL in $Sb_2(S, Se)_3$ solar cells. This is primarily due to its ease of preparation through well-established deposition methods and satisfactory alignment with the conduction band [9]. Nevertheless, the use of CdS presents some drawbacks, mainly related to their toxic nature and a low bandgap (2.4 eV) that may cause current loss due to unintentional absorption of higher energy photons [31]. Moreover, cadmium diffusion into the absorber layer has been observed, leading to potential stability concerns for the devices [9]. Anatase-type titanium dioxide, TiO_2, possesses excellent stability and a wide bandgap of 3.2 eV, which can minimize absorption losses, and thus has increasing potential to be utilized as an ETL in antimony chalcogenide solar cells. However, an inert surface, caused by the high bond energy of titanium and oxygen, still hinders the heterojunction quality of TiO_2-based antimony chalcogenide devices, while causing difficulties on the adsorption of metal chalcogenide materials [32]. A comparative study of TiO_2 and CdS demonstrated that the more favourable band alignment of the CdS ETL resulted in a higher overall V_{OC}, while its parasitic light absorption caused limitations in J_{SC} [33].

- **Transparent conductive oxide (FTO)**: The transparent electrode is typically applied to the front of the cell, where it serves as the anode, or front contact. This layer should possess both high optical transparency and high electrical transport properties, although in general, a compromise must be made between transparency and conductivity [34]. While increasing the free charge carrier density may lower the electrode's resistivity, the optical transparency will suffer due to increased absorption [9]. Sputtered indium tin oxide (ITO) is an established thin film front contact with high conductivity, while maintaining low optical absorption. However, the cost of indium makes ITO an expensive material [34]. Hence, alternatives like the cheaper F-doped tin oxide (FTO) have emerged, while also presenting better thermal stability: studies showed that the sheet resistance of ITO may increase from 18 Ω to 52 Ω following thermal annealing at 450 °C, whereas the sheet resistance of FTO remains constant under the same conditions [35].

2.2.1 Deposition Methods of Antimony Chalcogenide Absorber Layers and State-of-the-Art Performance

Growing $Sb_2(S, Se)_3$ crystals with a 1D columnar structure perpendicular to the substrate is preferable, due to the anisotropic nature of its carrier transport properties. Nevertheless, its practical application is somewhat complex as the 1D materials tend to grow with low-energy crystal faces parallel to the substrate, in order to minimize the system's free energy [36].

Antimony chalcogenide thin films can be prepared through deposition techniques that are either vacuum-based or non-vacuum-based [37]. Vacuum-based deposition methods include techniques such as sputtering, vapour transport deposition (VTD) (figures 2.5c and 2.5d), thermal evaporation (TE) and close spaced sublimation (CSS). In 2019, an optimization of the CSS method allowed for efficiencies up to 9.2% in deposited Sb_2Se_3 devices [38]. In CSS, the powder precursor is placed in close proximity to the substrate in a vacuum chamber. The chamber is heated, causing the precursor material to sublime, and then condensing on the substrate, forming a thin film (figure 2.5a). An optimization of this technique allowed for the growth of Sb_2Se_3 nanorods along the [001] direction, contributing to the high PCE of the cell (figure 2.5b).

Nevertheless, non-vacuum deposition techniques are prefered, as they are more cost-effective, and ultimately have better scalability [37]. Furthermore, state-of-the-art films fabricated by vacuum-based processes will usually require high temperatures to improve the crystallinity,

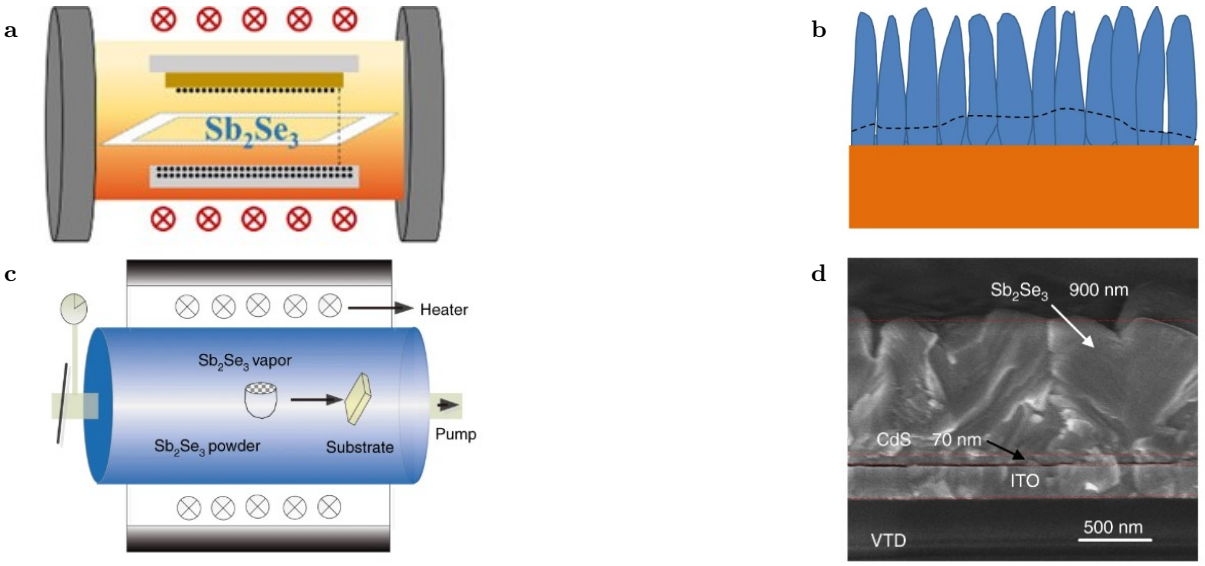

Figure 2.5: **a.** CSS of a Sb_2Se_3 film, where the substrate is coated at small distances (from [39]) **b.** Nanorod grain structure resulting in 9.2% PCE, attained by CSS deposition (from [39]) **c.** In the VTD method, the substrate is exposed to the volatile Sb_2Se_3 precursor (from [40]) **d.** Cross-sectional scanning electron microscopy (SEM) image of a Sb_2Se_3 film, deposited by VTD (from [40]).

which may lead to the decomposition of the films into intermediate species for deposition temperatures higher than 360ºC [41, 42]. In addition, $Sb_2(S, Se)_3$ solar cells fabricated by physical processes, such as VTD, suffer from poor morphology with abundant pinholes [43].

Other than being cheaper, non-vacuum, solution-based methods demonstrate superior potential in optimizing morphology, optical bandgap, composition and other optoelectronic characteristics, namely through the use of doping processes [23]. The more common non-vacuum deposition methods of antimony chalcogenide films usually include spin-coating, chemical bath deposition (CBD), spray-pyrolysis, and, more recently, hydrothermal deposition [37]. Naturally, there are some problems with solution-based deposition methods: vacuum-based techniques usually present smoother morphologies and higher crystallinaty. Still, low-temperature, low-cost and customizable deposition methods are needed, while focusing on producing high-performance antimony chalcogenide devices.

2.2.2 Hydrothermal Deposition of $Sb_2(S, Se)_3$ Films

Hydrothermal deposition methods are a straightforward, inexpensive, and highly versatile technique for the fabrication of antimony chalcogenide films. This approach primarily involves placing the substrates within an autoclave containing the precursor solution (Sb, Se and S sources) and maintaining it at a particular temperature for a specified duration (figure 2.6). The resulting convection currents facilitate the growth of the intended material on the substrate surface.

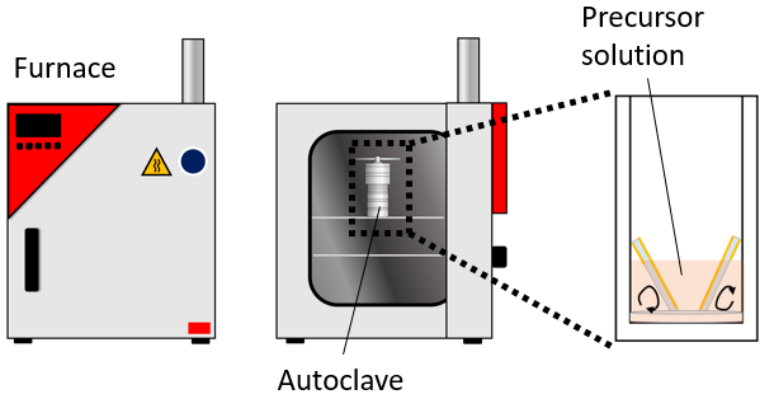

Figure 2.6: Hydrothermal synthesis process for the fabrication of $Sb_2(S, Se)_3$ thin films. A heated autoclave provides the appropriate temperature and pressure conditions for the deposition process.

The highest antimony sulfoselenide solar cell efficiencies reported have been achieved by low-temperature, solution-based hydrothermal deposition approaches. By this deposition technique, the 10% efficiency barrier was broken in 2020 [43], with further improvements of the absorber layer achieving a PCE of 10.7% in 2022 [17] and 10.75% in 2023 [44]. The latter constitutes the highest efficiency of all antimony-based solar cells. Concerning the physical properties of the as-deposited films, this method presents some major advantages with regard to other techniques. Namely, regulation over the Se/S ratio, based on precursor concentration, allows for easy bandgap tuning and, consequently, a higher absorption of photons [45]. Moreover, the hydrothermal synthesis enables precise control over the deposition parameters. For instance, film thickness is proportional to the duration of the hydrothermal process [43]. Finally, high-quality, good morphology and appropriately oriented films have been produced by using this simple deposition technique [45].

Table 2.2 shows some high-impact studies that applied hydrothermal deposition methods of antimony chalcogenide films, as well as the experimental conditions and the resulting efficiency.

Table 2.2: Previous experience of hydrothermal deposition of $Sb_2(S,Se)_3$ films, with Sb, S and Se sources, temperature and duration of the hydrothermal process, substrate and achieved PCE. Precursor quantities are omitted for the sake of simplicity.

Article	Precursor (source)			Temperature (ºC)	Time (h)	Substrate	PCE (%)
	Sb	S	Se				
Liu et al (2021) [41]	$C_4H_4KO_7Sb{\cdot}0.5H_2O$	CH_4N_2S	Na_2SeSO_3	100	2	Glass/FTO/CdS	7.9
Tang et al (2020) [43]	$C_4H_4KO_7Sb{\cdot}0.5H_2O$	$Na_2S_2O_3{\cdot}5H_2O$	CH_4N_2Se	135	0.5 - 5	Glass/FTO/CdS	10.0
Zhao et al (2021) [17]	$C_4H_4KO_7Sb{\cdot}0.5H_2O$	$Na_2S_2O_3{\cdot}5H_2O$	CH_4N_2Se	85 - 120	3	Glass/FTO/CdS	10.7
Wang et al (2020) [46]	$C_4H_4KO_7Sb{\cdot}0.5H_2O$	$Na_2S_2O_3{\cdot}5H_2O$	CH_4N_2Se	130	2	Glass/FTO/$CdCl_2$:CdS	10.5

2.2.3 Post-Deposition Chemical Treatments

Post-deposition treatments (PDT) have been shown to improve the physical and optoelectronic characteristics of light absorbing materials, as well as passivate defects at the interfaces of heterostructures [17]. For instance, PDT using alkali elements, such as NaF [47], KF [47] [48], RbF [49] and CsF [5], have continuously increased the efficiency of CIGS thin film solar cells up to the record efficiency of 23.4% [5]. Nonetheless, the performance of antimony chalcogenide solar cells is still lagging when compared to more traditional thin film technologies, mainly due to a V_{OC} deficiency. In fact, champion antimony chalcogenide cells barely achieve 50% of their V_{OC} SQ limit theoretical value (figure 2.7). Because it is well-known that defect-assisted and interface-induced recombination are related to V_{OC} deficiency, it is necessary to develop new ways to promote defect passivation at interfaces, while promoting proper energy band alignment [50].

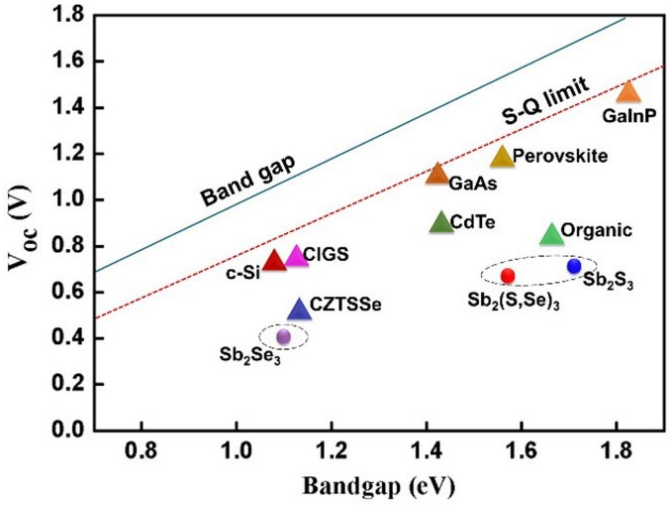

Figure 2.7: V_{oc} values of the different PV technologies champion devices until 2021 (from [50]).

It has come to be understood that post-treatment for each material is unique, and establishing

suitable treatment processes for each compound constitutes a challenge for researchers [17]. Previous works with antimony chalcogenide materials included treatments with decylphosphonic acid (DPA) [51], thioacetamide (TA) [52], $SbCl_3$ [53], and $CuCl_2$ [54], mostly enabling the passivation of interfacial and trap defects and improving PV performance. A study by Wang et al [46] in 2020 achieved an efficiency of 10.5% on hydrothermally synthesized $Sb_2(S,Se)_3$ films by using EDTA (ethylenediaminetetraacetic acid) as an additive to the precursor solution. The addition of EDTA to the solution used during the hydrothermal process allowed for a controlled nucleation of high quality $Sb_2(S,Se)_3$ material.

In 2021, Zhao et al [17] achieved the highest reported PCE of an antimony chalcogenide solar cell by using alkali metal fluorides as a solution post-treatment on hydrothermally deposited films. The applied treatment methods allowed the formation of a mild S/Se grading at the absorber layer (figures 2.8a and 2.8b), favoring good energy alignment of the $Sb_2(S,Se)_3$ film with the HTL (figure 2.8c). This promoted enhanced carrier transport, allowing for champion levels of efficiency. In particular, the NaF-PDT process attained an open-circuit voltage of 0.673 V, a short-circuit current of 23.7 mA/cm^2, and a fill factor of up to 66.8%, obtaining a champion efficiency of 10.7%. NaF-treated cells were also tested for their reproducibility, presenting, on average, an improvement in performance. The long-term stability of the devices was tested after 30 days of storage, retaining 93% of the initial PCE, representing an improvement when compared to control cells.

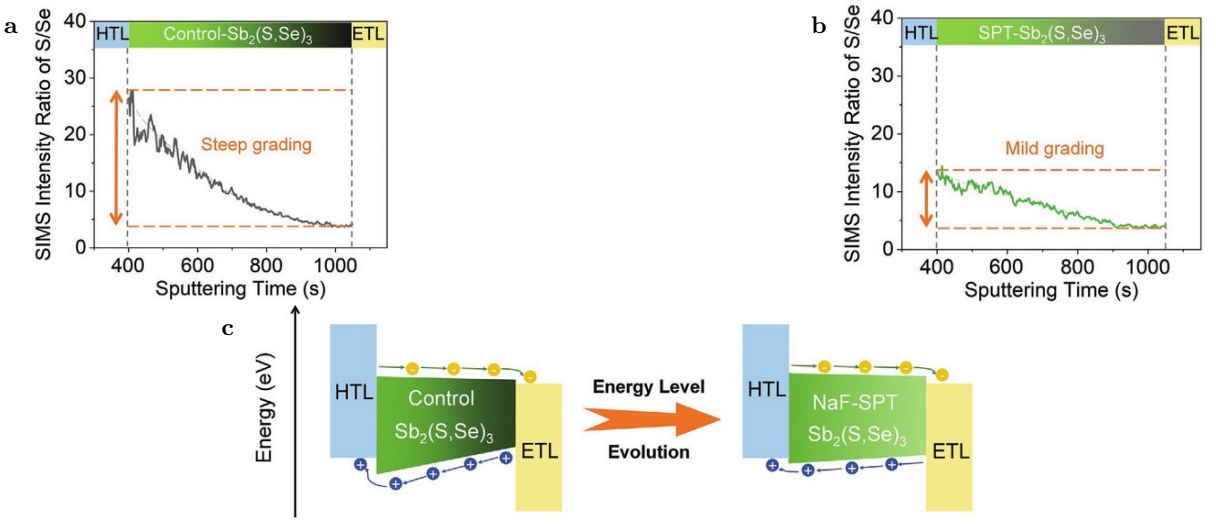

Figure 2.8: **a.** Intensity ratio of control $Sb_2(S,Se)_3$ films obtained by secondary-ion mass spectrometry (SIMS) **b.** Intensity ratio of NaF-treated $Sb_2(S,Se)_3$ films obtained by SIMS **c.** Energy level evolution of the two films. The solution post-treatment promoted an improved energy band alignment with a more spatially flat valence band maximum (from [17]).

2.2.4 Annealing

After the hydrothermal synthesis process, as-deposited $Sb_2(S, Se)_3$ films usually present poor cristallinaty. The disorderly arrangement of atoms hinders the movement of charge carriers and promotes charge recombination due to defects. For this reason, an annealing process is employed in order to increase grain size, promote crystallization and compactness, while eliminating defects, such as dislocations and grain boundaries, thereby improving the electrical performance of the solar cell [55]. Annealed antimony chalcogenide films transform to polycrystalline with orthorhombic structure, with films presenting smooth grain morphology, as demonstrated in figure 2.9 [56, 57]. The procedure involves exposing the thin film to a high temperature for a set duration, typically in a regulated atmosphere. It was observed that the surface of the antimony chalcogenide films underwent oxidation, resulting in a layer of Sb_2O_3, when they were subjected to annealing in an air atmosphere [58]. This is detrimental, as oxidation can provoke current leakage at the interfaces and the introduction of deep trap levels below the conduction band [59] [60]. To avoid oxidation, the annealing process should be performed in an inert gas atmosphere. This is desirable, as inert gases do not engage in chemical reactions with the thin film, thereby reducing the probability of oxidation or any other chemical processes that could harm the efficiency of the solar cell.

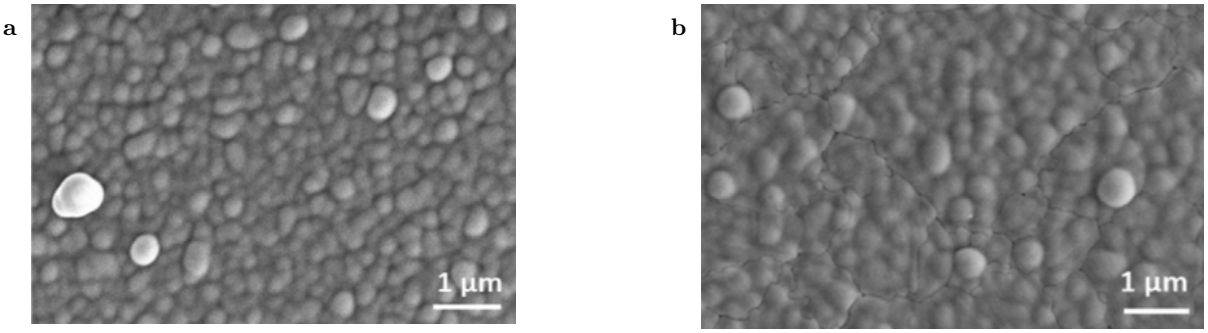

Figure 2.9: **a.** Top-view SEM image of a $Sb_2(S, Se)_3$ film without post-deposition annealing **b.** Top-view SEM image of a $Sb_2(S, Se)_3$ film annealed at 300°C. We can observe that the sample that underwent annealing presents a compact and uniform structure, and well-defined grain boundaries (from [61]).

The annealing temperature can critically influence the morphology and crystal structure of the thin film. An annealing temperature of 300 - 350°C was found to be optimal in improving the film morphology and in increasing grain size, whereas, for temperatures larger than 400°C, annealing promotes crystallographic layering along the [120] orientation, which is harmful to charge carrier transport efficiency [43, 59]. Costa et al [59] also noted a substantial decrease

in the thickness of the films that underwent thermal treatment at these higher temperatures, which could be attributed to the vaporization of the material. For rapid thermal processes, an optimized annealing time of 10 minutes at these temperatures has been shown to produce crystalline $Sb_2(S, Se)_3$ films with minimal surface roughness [43].

Although the 300 - 350°C temperature range has been found to be optimal, the annealing process is affected by the specific fabrication conditions used in each case, and a optimization study may produce better results. This will be one of the parameters tested during this work and the respective results will be presented in Chapter 4.

The following chapter, however, will present a description of the fabrication process of the layers used in the $Sb_2(S, Se)_3$ solar devices, while also briefly addressing the employed characterization techniques for the study of the antimony chalcogenide material.

3 Experimental Section

With this work, we intend to improve the quality of the hydrothermally deposited films of $Sb_2(S, Se)_3$ on SLG/FTO/TiO_2 substrates, performed at NOEA. The structure of the fabricated antimony chalcogenide solar cells can be seen in figure 2.4. For the study of the $Sb_2(S, Se)_3$ layer, the Spiro-OMeTAD HTL and the gold contacts were not deposited. This chapter will focus on the experimental methods used for the deposition of the different layers, as well as provide an overview on the characterization techniques employed to study the deposited thin films.

3.1 Process Flow

3.1.1 Substrate Preparation

The as-prepared samples followed a n-i-p structure. In this configuration, the active layers of the solar cell are deposited onto a transparent substrate, which is typically a glass plate with a transparent conductive oxide (TCO) coating. In the current study, a commercially available (25 x 25 x 1.1) mm TEC-10 substrate consisting of soda-lime glass (SLG) with a fluorine-doped tin oxide (FTO) layer was employed.

The first step of the process was to cut the original TEC-10 FTO (25 x 25 x 1.1) mm substrates in two (25 x 12.5 x 1.1) mm equal pieces, as depicted in figure 3.1. This was defined as the standard substrate size for this work. The substrates were then submerged in acetone and placed in an ultrasonic cleaner for 15 minutes. The process was repeated in isopropanol for 10 minutes and in deionized water for 5 minutes. After the multi-step cleaning procedure, the substrates were blow-dried with a pressurized N_2 gun. Finally, the substrates were subjected to a ozone cleaning under UV light (UVO treatment). This treatment allows for the removal of organic residues from the surface of the conductive oxide, while reducing its surface energy, and increasing wettability or hydrophilicity of the layer, thus allowing for a more appropriate surface for the deposition of the ETL.

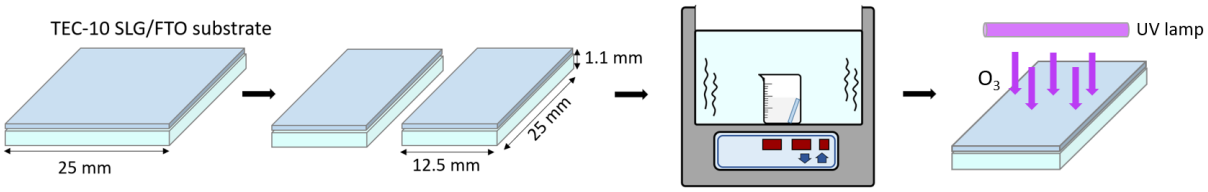

Figure 3.1: Preparation of substrates for the deposition of the active layers. Ultrasonic cleaning followed by a UVO treatment ensures that there are no contaminants or impurities on the FTO layer surface prior to the deposition of the ETL while increasing the hydrophilicity of the FTO layer.

3.1.2 Compact TiO_2 Layer Deposition

Throughout this work, the deposition of the compact anatase-type TiO_2 ETL was performed via 3 different techniques: spray-pyrolysis, spin-coating and sputtering. The methods employed will be briefly summarized in the following subsections. The deposition protocols for the sprayed and spin-coated compact TiO_2 layers was based on previous studies [22, 62] and further optimized at NOEA/INL.

Spray-pyrolysis

This deposition technique involves a precursor solution that is sprayed onto a heated substrate. A precursor solution of isopropanol (7 ml), acetylacetone (0.40 ml), and titanium diisopropoxide bis(acetylacetonate) (0.46 ml) was prepared and stirred for a minute. The SLG/FTO substrates were placed in a hotplate and pre-heated to 450°C. The area corresponding to the electrical contact was protected with glass before the deposition. The substrates were then sprayed for sets of 6 repetitions, with a time gap of 20 seconds between sets. This time interval allowed for the initial substrate temperature to be restored. After the complete consumption of the solution, the samples were subjected to annealing by keeping them at the deposition temperature for 45 minutes. Once the annealing process was complete, the samples were allowed to cool down to a temperature of 150°C, following which they were removed from the hot plate.

Spin-coating

Spin coating is a technique employed for the fabrication of uniform thin films. This approach capitalizes on the principles of centripetal force and surface tension inherent in the solution. In static spin coating, the procedure involves dispensing a small volume of the coating material solution onto the substrate's center. Subsequently, the substrate is rotated at high speeds for a brief duration, typically a few seconds, in order to uniformly distribute the coating material

across its surface. If the substrate rotates while the precursor solution is being deposited, the process is called dynamic spin coating [63].

Due to the sensitivity of some materials to oxygen (for example, Spiro-OMeTAD), the spin coater was placed inside a glovebox, an enclosure designed to maintain an inert atmosphere. For the coating of the c-TiO_2 film, a solution of 2.53 ml of isopropanol and 35 μl of hydrochloric acid (HCl) was prepared by stirring for 15 minutes. A second solution of 2.53 ml of isopropanol and 369 μl of titanium isopropoxide was also stirred for 15 minutes. Finally, the two solutions were mixed and stirred for 20 minutes. 200 μl of the resulting solution was statically spin coated on the SLG/FTO substrate at 4000 rpm for 15 seconds and the deposited film was heated at 120°C for 15 minutes in a hotplate. The samples were then removed from the glovebox and annealed inside a dry oven at 500°C for 30 minutes.

Sputtering

Sputtering is a physical vapor deposition (PVD) technique used to deposit thin films onto substrates. It relies on high-energy gaseous ion bombardment of a target material in a vacuum chamber. This bombardment ejects atoms or molecules from the target's surface, which then travel a short distance and deposit onto the substrate, forming a thin film [64]. One of the particularities of this method is that it allows for the deposition of high-quality large area oxide films [65].

In magnetron sputtering, a magnetic field is introduced near the target material to enhance the sputtering process, as it increases the efficiency of the ejection process by confining the ions close to the target. Usually, an inert gas like argon is used as the ionic source.

The TiO_2 layer was deposited in a Multi-target UHV Sputtering System manufactured by Kenosistec. Since the titanium dioxide material is a dielectric, a radio frequency power source was used at 60W. Argon gas was injected in the chamber with a flow of 20 scm, and the deposition rate was set at 0.137 nm/min.

3.1.3 Mesoporous TiO_2 Layer Deposition

Similarly to the compact TiO_2 layer, the synthesis of a mesoporous titanium dioxide structure was done by spin coating, according to previous studies [22] and optimized at INL. 0.155 g of TiO_2 commercial paste (30 NR-D) was vigorously stirred overnight in 1 ml of ethanol. The solution was then statically spin-coated on top of the already deposited c-TiO_2 layer at 5000

rpm for 10 seconds. Finally, the porous layer was heated in a hotplate at 120°C for 5 minutes, before being submitted to an annealing process at 500°C for 30 minutes inside a dry oven.

3.1.4 $Sb_2(S, Se)_3$ Deposition

The deposition of the $Sb_2(S, Se)_3$ absorber layer is one of the focal points in this work, as achieving good morphological properties is crucial in obtaining good performance of the solar cell.

As mentioned in Chapter 2, hydrothermal synthesis methods are a simple, low-temperature approach, that has been shown to output high-efficiency devices for antimony chalcogenide-based solar cells [17, 43, 46]. Typically, to carry out this process, specialized equipment such as an autoclave reactor and a furnace are necessary. The autoclave is subjected to a specific temperature for a set amount of time and contains a Teflon liner that holds the samples and a precursor solution. A schematics of the as-employed process can be observed in figure 3.2.

First of all, sample preparation required the protection of the FTO contact and the non-conductive backside of the glass substrate, thereby exposing solely a deposition area on top of the TiO_2 layer. Kapton tape was employed, as it can withstand high temperatures and chemical exposure. The prepared samples were aligned at a 60° angle in an in-house designed teflon support (Appendix A, figure A.1), and placed inside the teflon liner (Appendix A, figure A.2a).

For the solution, 0.61383 g of potassium antimonyl tartrate ($C_8H_4K_2O_{12}Sb_2 \cdot xH_2O$), 0.04921 g selenourea (NH_2CSeNH_2), and 1.98544 g of sodium theosulfate pentahydrate ($Na_2S_2O_3 \cdot 5\,H_2O$) were used as the antimony (Sb), selenium (Se) and sulfur (S) sources, respectively. These quantities were chosen based on previous optimization studies performed in literature [17, 43], and were not subject to change throughout this work. After weighing the chemicals on a precision scale, they were completely dissolved in 20 ml of deionized H_2O. Finally, the solution was poured inside the teflon liner, together with the already prepared substrates.

The Teflon liner was sealed inside the autoclave and introduced into a furnace preheated at 120°, for 3 hours. There, the deposition process would occur. Once the predetermined time elapsed, the samples were extracted from the autoclave and thoroughly rinsed with distilled water to eliminate any excess material. The Kapton tape was then peeled off, and the samples were dried with a N_2 gun before being placed in a desiccator for storage.

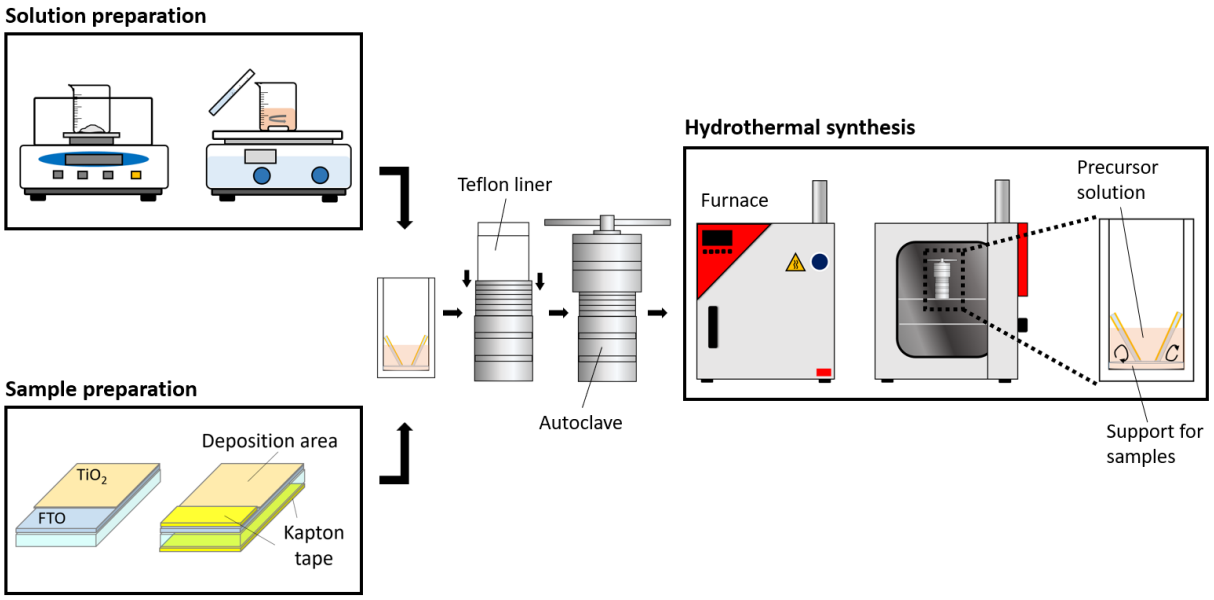

Figure 3.2: Process flow for the hydrothermal synthesis of $Sb_2(S, Se)_3$ thin-films.

3.1.5 NaF Post-Deposition Treatment

To test the effects of a NaF post-deposition treatment on $Sb_2(S, Se)_3$ thin films, a second hydrothermal synthesis was conducted after the deposition of the $Sb_2(S, Se)_3$ absorber layer. In accordance to previous studies [17], a NaF solution was prepared by dissolving 0.0252 g of NaF in 20 ml of deionized H_2O, and, similarly to the process described in figure 3.2, the newly-deposited samples were placed in the solution-filled autoclave. The hydrothermal process lasted for 70 minutes at a constant temperature of 120°C. The conditions of the post-deposition treatment were maintained constant throughout this work.

3.1.6 $Sb_2(S, Se)_3$ Annealing

As mentioned in Chapter 2, the annealing process is of paramount importance, as it allows for the crystallization of the $Sb_2(S, Se)_3$ film. The annealing procedure was conducted in a tubular Rapid Thermal Processing (RTP) oven (figure 3.3), manufactured by Termolab. All the process was controlled through a dedicated software. In order to ensure a controlled atmosphere, the oven was connected to a Busch Zebra RH 0003–0010 B rotary vane pump, capable of ultimate pressures of 6.7×10^{-3} mbar, and had a dedicated N_2 gas line, regulated by a flowmeter. Chamber pressure was monitored using two Pirani gauge sensors, which, combined, allowed for a working range of 1000 mbar to 10^{-4} mbar. The temperature of the samples was controlled using K-type thermocouples.

A representation of the intended annealing cycle can be seen on figure 3.4. The samples were

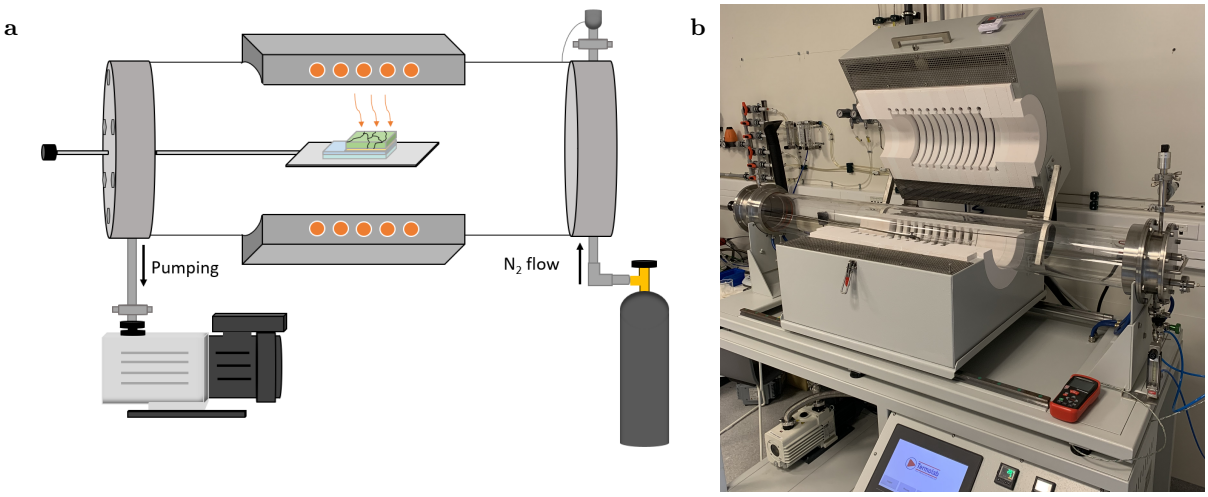

Figure 3.3: **a.** Representation of the annealing configuration used in this work. **b.** Image of the RTP oven used for the annealing process.

placed in the tubular oven with the $Sb_2(S, Se)_3$ film facing upwards, and the chamber was sealed. Before heating, a purge cycle was employed, as to remove contaminants and unwanted gases, such as oxygen and water vapor: the pump was turned on until the ultimate pressure of the system was achieved (approximately 0.1 mbar). The pump was then turned off, and the chamber was filled with 99% purity nitrogen at a flow rate of 1 l/min for 5 minutes. Finally, the N_2 flow was interrupted and the oven was pumped for another 20 minutes, in order to reestablish the base pressure of 0.1 mbar.

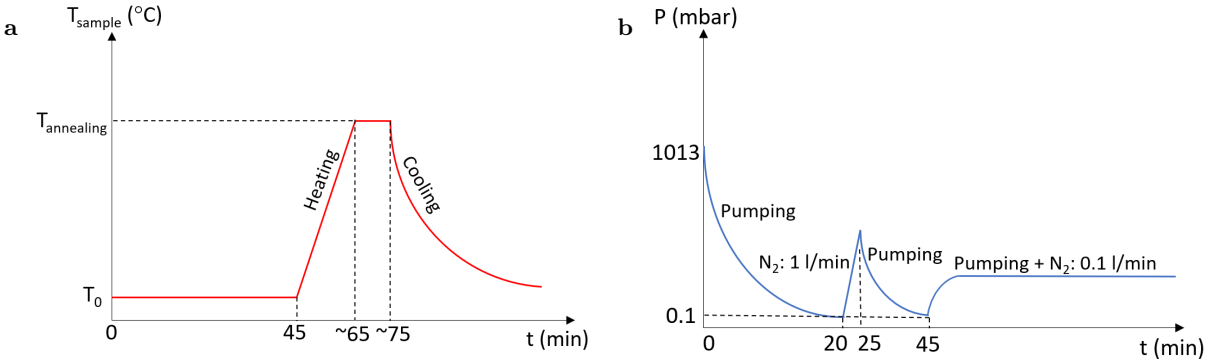

Figure 3.4: **a.** Representation of the sample temperature variation during the annealing process. T_0 is the ambient temperature. **b.** Representation of the chamber pressure variation during the annealing process.

Following the completion of the purge cycle, the heating process of the oven commenced, with an approximate heating rate of 15°C per minute. Once the intended annealing temperature was reached, the samples were kept at that temperature for 10 minutes. Subsequently, the heating

resistors were deactivated, allowing the samples to undergo a gradual and natural cooling process until they reached room temperature. Throughout these temperature stages, a continuous flow of nitrogen gas was maintained, enabled by the vacuum pump and a controlled nitrogen flowrate of 0.1 liters per minute. This allowed for a constant pressure of 2 mbar during the annealing process, which provided us with similar pressure conditions to the ones employed in previous experiments [17, 43]. Finally, ambient pressure was reestablished in the tubular oven by opening the N_2 line, and the samples were removed.

3.1.7 Spiro-OMeTAD Deposition

For the HTL layer, a thin layer of the compound Spiro-OMeTAD was spin-coated on top of the $Sb_2(S, Se)_3$ film inside a glovebox, according to previous studies [22]. For the solution, 102 mg of Spiro-OMeTAD was dissolved in 1.116 ml of chlorobenzene and stirred for a few minutes. After, the already dissolved Spiro-OMeTAD was doped with 40 μl of 4-*tert*-butylpiridine (tBP), 23 μl of bis-(trifluoromethane)sulfonimide lithium salt (Li-TSFI) solution and 10 μl of tris(2-(1H-pyrazol-1-yl)-4-*tert*-butylpyridine)cobalt(III) tri[bis-(trifluoromethane)sulfonimide] (FK209) solution, according to previous studies [22]. Finally, 40 μl of the prepared Spiro-OMeTAD solution was deposited on the substrate, spinning at 4000 rpm for 12 seconds. The final Spiro-OMeTAD film should look smooth and homogeneously distributed.

3.1.8 Au Contacts Deposition

The metallic contacts were deposited by thermal evaporation of a 70 nm gold film. During this process, the source material is heated to a high temperature in a vacuum environment, causing it to undergo evaporation. The high temperature promotes the movement of vapor particles, which converge and deposit directly onto the substrate. Finally, these vapors undergo a transition back to the solid state, forming the thin film [66]. The films were deposited over the Spiro-OMeTAD layer by using a Korvus Technology Hex System, with a deposition rate of 4.5 Å/s. The contact area was defined by a rigid acrylic mask, enabling a film geometry similarly to the one represented in figure 2.4.

3.2 Advanced Characterization of Thin Films

In order to analyze the films at the micro and nanoscopic scale, several characterization techniques have been employed throughout this project. The objective is to comprehend the composition, crystal structure, morphology, and other properties of the deposited $Sb_2(S, Se)_3$

material, and to examine the manner in which these properties impact the performance of the solar cell. We will briefly summarize some of the characterization methods used in this project.

3.2.1 X-Ray Diffraction (XRD)

When X-rays interact with a crystalline substance, a phenomenon known as coherent elastic scattering, or diffraction, may occur. The angle between two parallel incident rays A and B and two lattice planes (hkl), which have a lattice plane separation d_{hkl}, results in a reflected beam of maximum intensity (known as the Bragg peak) if the reflected waves, represented by A' and B' are in phase (figure 3.5). For this to occur, the difference in the path lengths between A and A' and B and B' must be an integer multiple (n) of the wavelength λ [67].

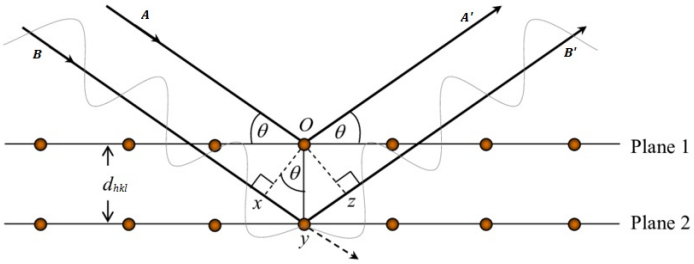

Figure 3.5: Conditions for X-ray diffraction, as described by Bragg's Law (adapted from [68]).

This property of crystals is reflected in Bragg's Law (equation 3.1).

$$n\lambda = 2d_{hkl}\sin\theta \tag{3.1}$$

Usually XRD is performed by fixing the wavelength λ and varying θ. An XRD pattern is obtained by plotting the intensity of the diffracted beams as a function of the diffraction angle. The diffraction pattern offers insights into the crystal structure, size of the crystal, and lattice spacing in the material. Furthermore, a sharper XRD peak (smaller FWHM) is typically indicative of larger crystallite materials, as given by the Debye-Scherrer equation (equation 3.2). XRD spectra of annealed films usually presents an increase in the sharpness of the peaks, demonstrating the effectiveness of annealing in improving the crystallinaty of the material [69].

$$L = \frac{K\lambda}{\beta\cos\theta} \tag{3.2}$$

where K is a dimensionless shape factor, dependent on the shape of the crystallite, λ is the X-ray wavelength, β is the FWHM of the diffraction peak and L is the mean size of the crystallite.

By interpreting Bragg's equation (equation 3.1), we can also see that a shift in XRD pattern towards lower diffraction angles indicates an enlarged lattice constant. This was observed by Tang et al [43] when introducing Selenourea (Se percursor, for reference see table 2.2) in the hydrothermal synthesis of antimony chalcogenide films: the larger ionic radius of the introduced Se^{2-}, when compared to that of S^{2-}, resulted in an larger lattice constant, reflected in a θ shift towards lower angles observed in the diffraction pattern. This means that XRD peaks of the alloy $Sb_2(S,Se)_3$ will be somewhere in between the characteristic diffraction peaks of the binary Sb_2Se_3 and Sb_2S_3 materials, with a shift towards higher angles with decreasing Se/(S+Se) concentration ratio, and a shift towards lower angles with increasing Se/(S+Se) ratio.

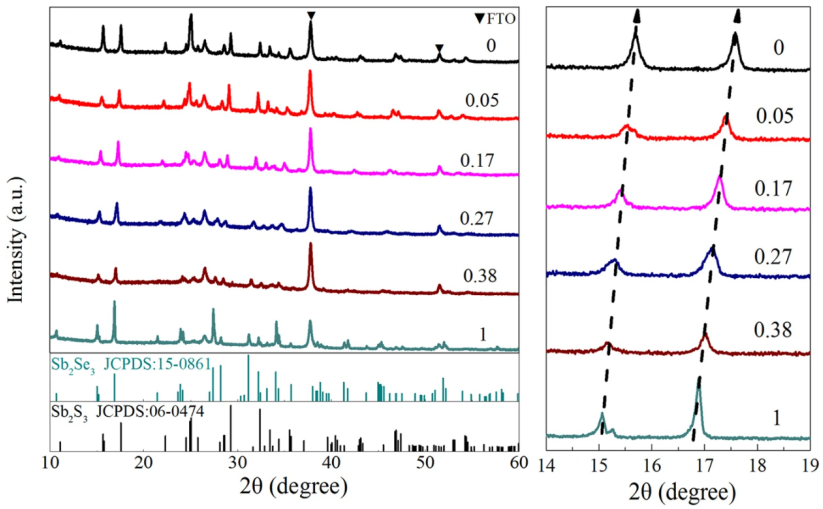

Figure 3.6: XRD pattern of $Sb_2(S,Se)_3$ thin-films for different Se/(S+Se) concentration ratios. We can observe a downwards shift for increasing selenium concentration (from [70]).

As mentioned in Chapter 2, achieving crystal growth with vertical ribbons in relation to the substrate is desirable. This means that antimony chalcogenide absorbers with predominant (hk1) planes have improved carrier transport and, consequently, better device performance [38]. XRD provides a powerful tool to analyze crystal orientation by considering the intensity of peaks corresponding to different planes. The texture coefficient formula provides quantitative information about the preferred orientation of polycrystalline materials by comparing the intensity of a diffraction peak with its reference intensity, this is, the expected intensity of the peak for a sample of randomly oriented crystals.

$$\mathrm{TC}_{h_i k_i l_i} = \frac{\frac{I(h_i k_i l_i)}{I_0(h_i k_i l_i)}}{\frac{1}{n}\sum_{j=1}^{n} \frac{I(h_j k_j l_j)}{I_0(h_j k_j l_j)}} \tag{3.3}$$

Nonetheless, because the $Sb_2(S,Se)_3$ material is an alloy of sulfur and selenium, with variable

concentrations of both, there is no standardized reference card available for this specific compound. Existing reference cards are only available for its binary constituents, namely Sb_2S_3 and Sb_2Se_3. For the overall quantification of the orientation of the $Sb_2(S, Se)_3$ films, the intensity ratio between (hk1) and (hk0) peaks is commonly calculated. This ratio informs us of the relative strength between vertically and horizontally oriented ribbons of a material. It is important to note that this ratio is used for comparative purposes only among samples of the same material, as it does not consider any specific reference orientation.

$$I_{[h_i k_i l_i / h_j k_j l_j]} = \frac{I_{h_i k_i l_i}}{I_{h_j k_j l_j}} \tag{3.4}$$

The diffractograms used throughout this study were obtained in a PANalytical X'Pert PRO MRD equipment (Cu Kα X-ray tube $\lambda = 0.154$ nm, 45 kV, and 40 mA).

3.2.2 Scanning Electron Microscopy (SEM)

Scanning Electron Microscopy (SEM) technique is widely used for imaging of thin film solar cells and has the capability of revealing layer thicknesses, surface morphology, topography and other relevant features of thin film stacks with a resolution of below 1 nm. In SEM, a focused beam of high-energy electrons is directed towards the surface of the sample. Imaging is done by collecting secondary electrons and backscattered electrons, both types being emitted from the film after irradiation. The energy of the incident beam, E_b, regulated via the acceleration voltage, is of particular importance, as it defines the penetration depth, R, of the incident electrons into the sample. The penetration depth can be empirically described by equation 3.5 [71].

$$R = \left(4.28 \times 10^{-2}\right) \cdot \frac{E_b^{1.75}\,(\mathrm{keV})}{\rho\left(\mathrm{g/cm^3}\right)}\ (\mu\mathrm{m}) \tag{3.5}$$

This means that higher acceleration voltages will give information about deeper regions of the films, while lower acceleration voltages provide data about the top of the sample. For this work, surface analysis of Sb2(S,Se)3 films by SEM was performed at acceleration voltages of 1 to 5 keV, providing us with information about the top 200 nm of the thin films.

Imaging can be done by top-view, providing information on sample surface from a "bird's eye view", or by cross-section, which can be done by fracturing a sample perpendicular to its surface, presenting a profile view of the thin-film. By using these two techniques, morphology,

grain size and boundaries can be studied, in conjunction with the characterization of interfaces, layer thickness and even crystallite orientation [71].

During this study, surface morphology and film thickness were studied via top view and cross-section SEM analysis, respectively, performed in a Fei NovaNanoSEM 650 equipment.

3.2.3 Electron X-ray Dispersive Spectroscopy (EDS)

Frequently, scanning electron microscopes are equipped with energy dispersive x-ray detectors that allow for compositional analysis of the thin films.

The quantification of elemental composition can be done by the detection of characteristic X-rays emitted from a sample upon electron-beam irradiation. Briefly, incident electrons can scatter on inner-shell electrons of an atom, ejecting them from the shell. An outer shell electron can then occupy the electron hole left by the ejected electron. The potential energy between the two electronic states can be emitted as X-ray radiation during this transition. Because each atomic element has its own structure, the emitted X-rays are characteristic of that element, allowing for compositional information. Naturally, the intensity of the detected X-ray radiation will be proportional to the atomic quantities present in the analyzed volume [71].

Nevertheless, this technique suffers from some limitations. Although overall analytical accuracy is near $\pm 2\%$, this value usually increases for lighter elements, being inaccurate for elements with $Z < 11$ [72]. Furthermore, good practice requires that the acceleration voltage should be no less than twice the highest excitation energy of any element detected in the measured sample. This means that for higher acceleration voltages, electron penetration will increase (equation 3.5), worsening spatial resolution, as the electron beam tends to spread out more [73]. For example, for $Sb_2(S, Se)_3$, a minimal acceleration voltage of 10 to 15 kV should be used, in order to measure the intensity of the Lα emission lines of antimony and selenium, as well as the intensity of the Kα and Lα lines of sulfur.

3.2.4 X-ray Photoelectron Spectroscopy (XPS)

Based on the photoelectric effect, this characterization technique uses X-ray photons to ionize surface atoms of the sample and analyze the kinetic energy of the photoelectrons. Because the binding energy of the ejected core electrons are characteristic for each element, XPS provides a tool for the identification of the chemical species present on the sample's surface [74]. For semiconducting materials, this interaction can be described by equation 3.6, considering that

the emission of photoelectron is as elastic process. Equation 3.6 relates the kinetic energy of the ejected photoelectron, E_K, with the energy of the incident radiation, $h\nu$, the binding energy of the emitted electron, with respect to the Fermi energy level, E_b, and the work function of the material, Φ, which is just the difference between the vacuum level and the Fermi energy level.

$$E_K = h\nu - \phi - E_b \tag{3.6}$$

A XPS spectrum is usually composed by several peaks, corresponding to a specific orbital of a species. Because the ejected photoelectrons have a short travel path before suffering from inelastic scattering processes, XPS is a surface sensitive technique, essentially providing information about the first 10 nm of the sample surface [74]. The area under each peak (A_i) is proportional to the amount of substance present in the analyzed region, allowing for a compositional study of the sample surface. Nevertheless, it is first necessary to normalize the signal by accounting for various physical and instrumental factors that disturb the measurements. A Relative Sensitivity Factor (R.S.F.) is introduced in order to normalize each peak. The atomic percentage of each element (Q_i) can be determined by using equation 3.7.

$$Q_i = \frac{\frac{A_i}{(R.S.F.)_i}}{\sum_{j=0}^{N} \frac{A_j}{(R.S.F.)_j}} \times 100\ (\%) \tag{3.7}$$

If we want to determine the ratio of two elements, equation 3.7 becomes simply:

$$\frac{Q_i}{Q_j} = \frac{\frac{A_i}{(R.S.F.)_i}}{\frac{A_j}{(R.S.F.)_j}} \times 100\ (\%) \tag{3.8}$$

XPS analysis can also provide some information about the electronic properties of the analyzed film. Near the 0 eV binding energy, the XPS spectrum presents an intensity of 0 counts/s as no electrons are being ejected. As the binding energy increases, the intensity tends to increase linearly, corresponding to the Fermi edge region of the spectrum. The difference between the Fermi energy level (E_F) and the valence band maximum (E_v) can be estimated by intercepting the linear fit of the Fermi edge with the binding energy axis. To have a complete description of the electronic properties of the analyzed film, the work function, Φ, and the bandgap of the material, E_g, must be determined by the Ultraviolet Photoelectron Spectroscopy (UPS) and Reflection Electron Energy Loss (REELS) technique, respectively. Unfortunately, for this work, neither could be used, and the electronic analysis was limited to the determination of the E_F-E_v value.

For the XPS analysis, a ESCALAB 250Xi system, manufactured by Thermo Fisher Scientific was used. The peak analysis was performed by using the Avantage 5.988 software, and the XPS spectra was calibrated by centering the C 1s peak at the 284.8 eV binding energy.

3.2.5 Spectrophotometry

Ultraviolet-Visible-Near Infrared (UV-Vis-NIR) spectrophotometry is a simple characterization technique that allows for the study of the optical properties of thin films, namely, transmittance, absorption and reflectance behavior to ultraviolet, visible and near-infrared wavelengths of light. By analyzing the obtained spectrum, it is possible to obtain other properties of thin films.

For this study, a Perkin Elmer Lambda 950 spectrophotometer was used, with a similar configuration to the one seen in figure 3.7a. This apparatus uses two identical beams emitted by an halogen light source towards an integrating sphere detector. To ensure calibration and accurate measurements, the first beam interacts with a reference Spectralon material. The second beam is directed towards the sample. By comparing the response of the sample with the response of the reference material, normalized sepctra can be obtained. In this work, relative transmittance was measured for wavelengths ranging from 300 nm to 1200 nm, with a 2 nm step. Absorbance can be easily determined from the transmittance measurements by employing the well-known Beer-Lambert Law (equation 3.9).

$$T = \frac{I}{I_0} = e^{-\alpha L} \Leftrightarrow \alpha = \frac{1}{L} ln\left(\frac{1}{T}\right) \tag{3.9}$$

Where I is the intensity of the transmitted beam, I_0 is the intensity of the incident beam, α is the absorption coefficient and L is the thickness of the sample.

One of the main applications of UV-Vis-NIR spectrophotometry in thin films is the determination of the optical bandgap (E_g). In an ideal spectrum of a perfect direct bandgap semiconductor, there is minimal absorption of photons with energies below the bandgap, and a sudden and significant increase in absorption is observed for photons with energies above the bandgap. The determination of a semiconductor's bandgap using its optical properties relies on the Tauc method, which assumes that the energy-dependent absorption coefficient α can be mathematically described by equation 3.10 [75].

$$(\alpha \cdot h\nu)^{1/\gamma} = B\left(h\nu - E_{\mathrm{g}}\right) \tag{3.10}$$

In equation 3.10, $h\nu$ is the energy of the incident photon, in eV, and B is a constant. The γ factor will be 1/2 if we are considering direct bandgap transitions and 2 if the transitions are indirect in nature. The bandgap can be simply determined by solving equation 3.10 for E_g when $(\alpha \cdot h\nu)^{1/\gamma} = 0$, which can be done graphically by plotting the function $f(h\nu) = (\alpha \cdot h\nu)^{1/\gamma}$. However, equation 3.10 assumes that the measured absorbance is null for photon energies lower than the bandgap. This is generally not true, since intensity is affected not only by absorbance, but by reflectance and scattering as well, which are usually dependent on the morphology of the analyzed sample. These effects are often observed by a non-zero baseline. For this reason, a more correct way of obtaining the optical bandgap value is to draw a tangent to the baseline and considering it as the line corresponding to zero absorbance [76].

It should be noted that in graded thin films, where the composition varies with depth, the bandgap value is not uniform across the sample. In such cases, high-energy photons are absorbed by the wide bandgap materials, and only photons with energy lower than the narrowest bandgap are transmitted (figure 3.7b). Hence, when fitting the Tauc plot, the determined bandgap corresponds to the narrowest bandgap present in the film [77]. The relative concentration of selenium and sulfur in $Sb_2(S, Se)_3$ thin films will directly affect the bandgap value. Studies have shown that increasing the relative selenium to sulfur concentration will cause an upshift to the valence band, while keeping the conduction band unchanged [43]. These results indicate that there is a decreasing trend in the bandgap with higher selenium concentrations, and that the bandgap obtained through UV-Vis-NIR spectrophotometry corresponds to the region of the film with the highest Se/(S+Se) ratio.

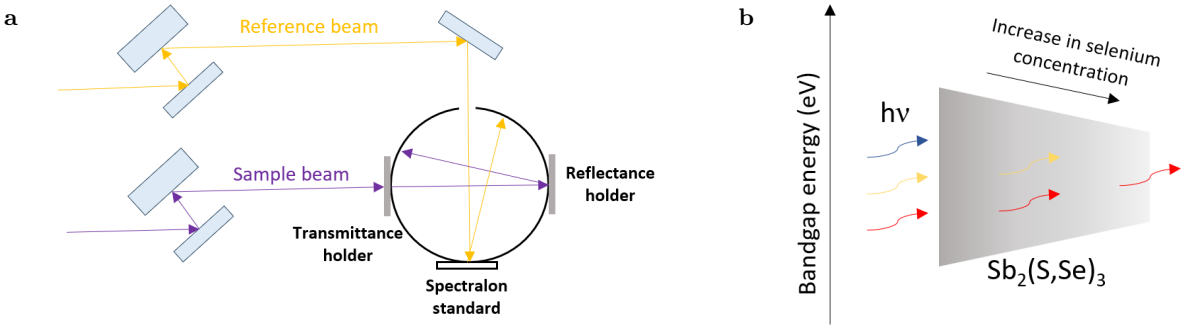

Figure 3.7: **a.** Configuration of the UV-Vis-NIR spectrophotometer used for transmittance measurements. **b.** Absorption process of photons in a graded $Sb_2(S, Se)_3$ thin film.

4 Results and Discussion

Having presented an overview on the current state of the art of thin film antimony chalcogenides, followed by an outline of the experimental methods employed, the following chapter aims to present some of the results obtained through the course of the experimental work developed at INL. Furthermore, the results and their implications will be compared with the existing literature in a critical manner. Before the fabrication of complete photovoltaic devices, we focused on the study of the $Sb_2(S, Se)_3$ absorber layer. The following sections will concentrate on the efforts made to enhance the properties of this layer by studying different growth variables, while constructing a guideline for the deposition of these thin films. The impact of this parameters will be assessed by using the different characterization techniques described at the end of Chapter 3. At the end of this chapter, the obtained results will be applied in the fabrication of complete photovoltaic devices.

4.1 Preliminary Deposition Studies of $Sb_2(S, Se)_3$ Thin Films

In order to address the state of the deposition process, some initial samples were fabricated according to the methods described in Chapter 3: SLG/FTO substrates were prepared and cleaned, and a compact TiO_2 ETL was deposited by spray-pyrolysis. This deposition method of the ETL layer was used as the standard in this work. Subsequently, the $Sb_2(S, Se)_3$ absorber layer was synthesized on top of the SLG/FTO/TiO_2 substrate. Additionally, half the fabricated $Sb_2(S, Se)_3$ were annealed for 10 minutes at an arbitrary 300°C temperature. This allowed us to have an initial idea of the impact of the annealing process on the properties of the deposited antimony chalcogenide films.

4.1.1 Morphology

The as-prepared films were firstly analyzed in SEM, using a 5 kV acceleration voltage, allowing for a surface study of the films. Figure 4.1 shows top-view and cross-sectional images of as-

deposited and annealed $Sb_2(S, Se)_3$ films, prepared by the previously described hydrothermal method.

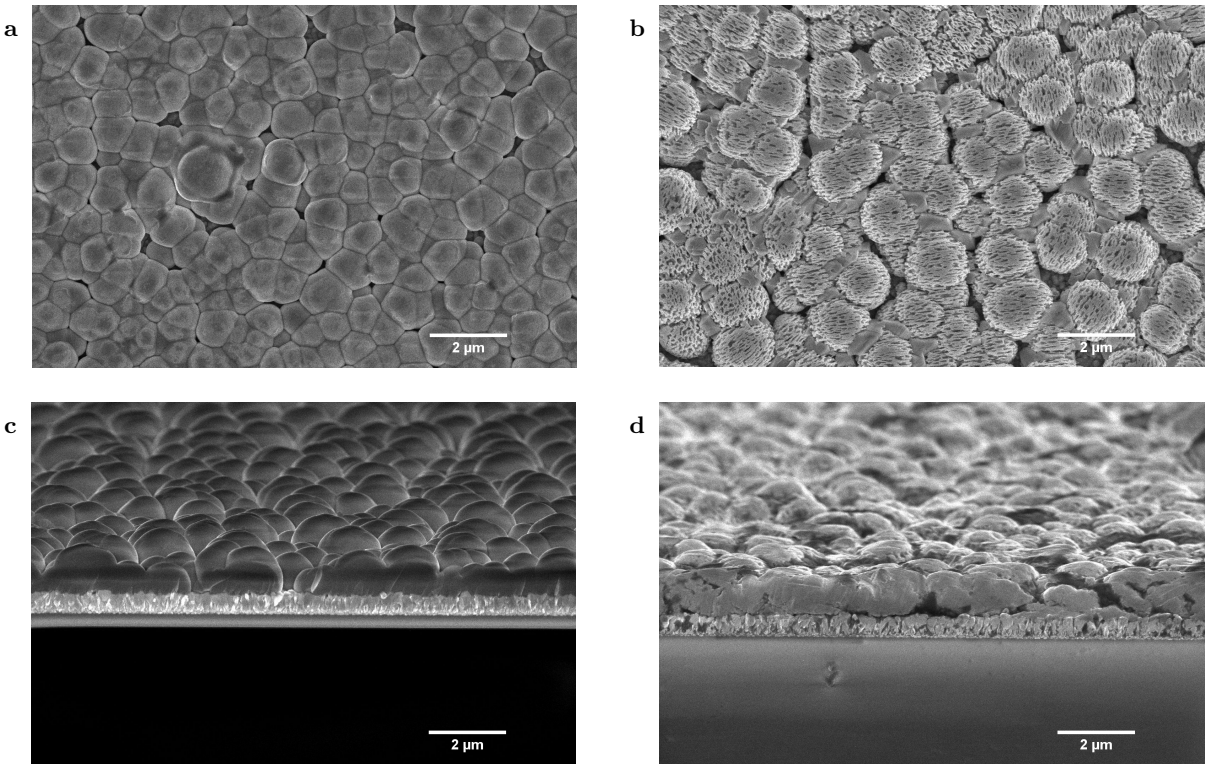

Figure 4.1: **a.** Top-view SEM image of amorphous $Sb_2(S, Se)_3$. **b.** Top-view SEM image of $Sb_2(S, Se)_3$ annealed at 300°C. **c.** Tilted cross-sectional image of amorphous $Sb_2(S, Se)_3$. **d.** Tilted cross-sectional image of $Sb_2(S, Se)_3$ annealed at 300°C.

Figure 4.1 illustrates that the films are formed by well-defined grains, with clear grain boundaries. At first view, the as-deposited films are composed by hemispherical grains, that seem to merge with the introduction of the annealing process. This is likely caused by the horizontal expansion of $(Sb_4(S, Se)_6)_n$ ribbons resulting from increased surface diffusion, as represented in figure 4.2c [57]. Because the films are formed by hemispherical grains, they are not uniform in thickness. Average values for grain size and thickness are presented in the box plots of figures 4.2a and 4.2b. Grain sizes were determined by measuring the diameters of each grain, as usually described in the literature. Thickness measurements were performed on several points of the cross-sectional imagery (figures 4.1c and 4.1d). As we can observe, annealing tends to decrease overall thickness, while promoting grain growth and a flatter surface, owing to the already mentioned surface diffusion process. Film thickness variations may also be attributed to the evaporation of sulfur and selenium from the film's surface during annealing, as reported in previous studies [57, 61].

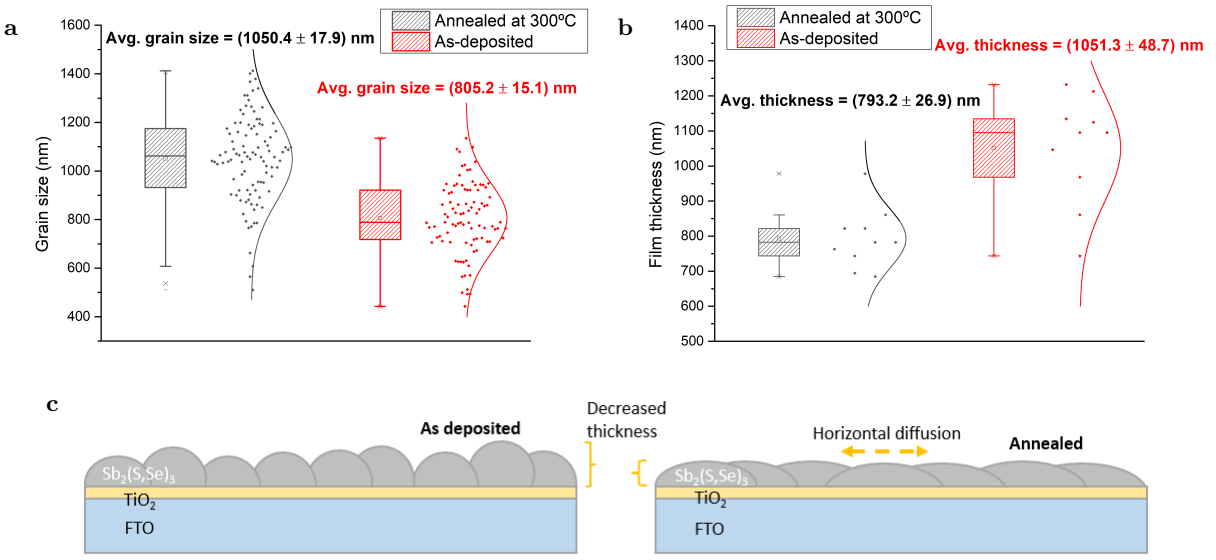

Figure 4.2: **a.** **b.** Box plot of grain-size and film thickness for as-deposited and annealed $Sb_2(S, Se)_3$ films. **c.** Representation of the horizontal grain expansion of $Sb_2(S, Se)_3$ films, as a result of the annealing process.

Nevertheless, some undesired characteristics were observed. First of all, undefined crystals in between the $Sb_2(S, Se)_3$ grains formed with the annealing process, which could indicate a secondary phase. Secondly, the films present holes and voids, affecting the performance of final photovoltaic devices, as they can contribute to the formation of shunt paths between the ETL and HTL [78].

4.1.2 Composition

To assess the composition of the $Sb_2(S, Se)_3$ material, as well as the secondary phase observed on the films, EDS analysis was performed at 20 kV acceleration voltage, and the results are presented in tables 4.1 and 4.2. Two points of analysis were chosen, corresponding to the two phases with different morphologies present in the film. Point 1 was analyzed, revealing a real stoichiometry of the film of $Sb_2(S_{0.71}, Se_{0.29})_3$. Point 2, however, showed a much higher oxygen concentration. This may indicate that the darker secondary phase crystals observed in SEM images are the result of the oxidation of the sample surface during annealing. As mentioned in Chapter 2, the formation of oxides affects the chemical states of the annealed film, introducing trap levels that act as recombination centers for the photogenerated charge carriers.

Due to the fact that the oxides were only observed in samples that were annealed, a thorough investigation was conducted on the RTP oven used for the annealing process. As previously mentioned, maintaining an inert atmosphere during annealing is paramount, since oxidation

Table 4.1: Atomic ratios of the identified elements in point 1.

Element	Atomic ratio (%)
O	11.62
Sb	32.42
Se	16.13
S	39.22

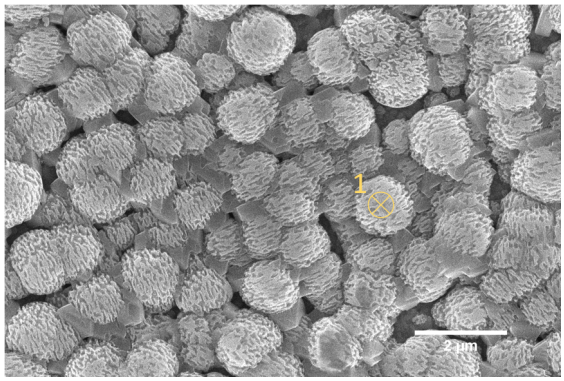

Figure 4.3: Top-view SEM of $Sb_2(S, Se)_3$ for EDS scan, with indication of the analyzed point 1.

Table 4.2: Atomic ratios of the identified elements in point 2.

Element	Atomic ratio (%)
O	44.37
Sb	30.21
Se	6.65
S	18.77

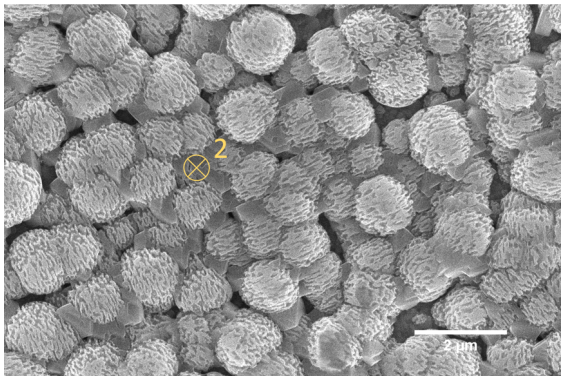

Figure 4.4: Top-view SEM of $Sb_2(S, Se)_3$ for EDS scan, with indication of the analyzed point 2.

rate increases with temperature. A leak test using an helium detector found several leaks in the feeding tubes of the N_2 line, leading to the contamination of the line with oxygen. The RTP oven was fixed by changing the original fittings with appropriate vacuum fittings, as reported in Appendix B.

Figure 4.5 shows SEM top-view images of samples annealed before and after the RTP oven fix. As we can observe, the sample annealed after repairing the N_2 feeding line does not show the identified oxide crystals. Furthermore, the $Sb_2(S, Se)_3$ grains present a smoother morphology, which is a positive trait for thin film solar cells.

To confirm the elimination of the oxides, EDS was first performed on several points of the sample annealed after fixing the RTP oven. As we can see from table 4.3, the oxygen content dropped abruptly after the leaks of the RTP oven were repaired, when compared to previous

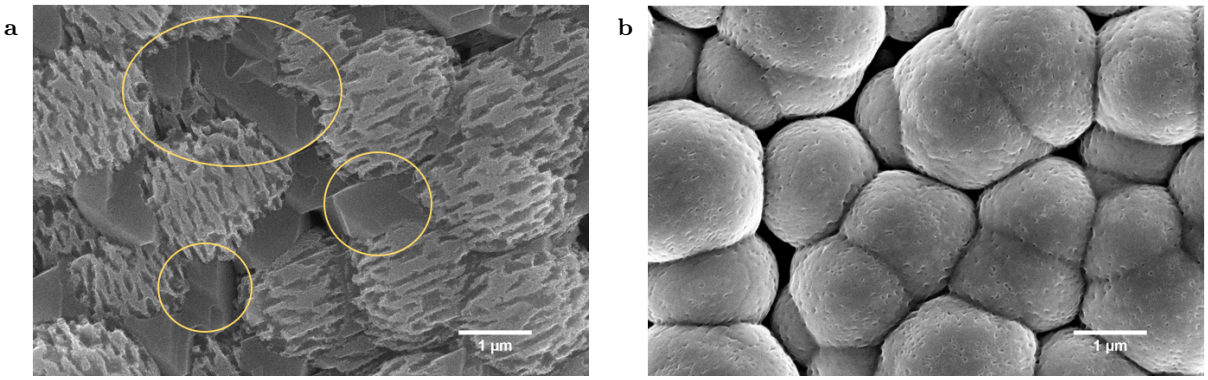

Figure 4.5: **a.** Top-view SEM of a $Sb_2(S, Se)_3$ film, annealed at 300°C, before the RTP oven fix. **b.** Top-view SEM of a $Sb_2(S, Se)_3$ film, annealed at 300°C, after the RTP oven fix.

samples (table 4.2). This result emphasizes the importance of maintaining a oxygen-free atmosphere during the annealing step. Furthermore, it seems that the crystals identified in figure 4.5a correspond to a secondary oxidation phase of the $Sb_2(S, Se)_3$ material that forms during the recrystallization process at high temperatures in the presence of oxygen contaminants.

Table 4.3: Atomic ratios of the identified elements in the $Sb_2(S, Se)_3$ sample annealed at 300ºC after the RTP oven fix.

Element	Atomic ratio (%)
O	3.25
Sb	43.55
Se	11.35
S	41.86

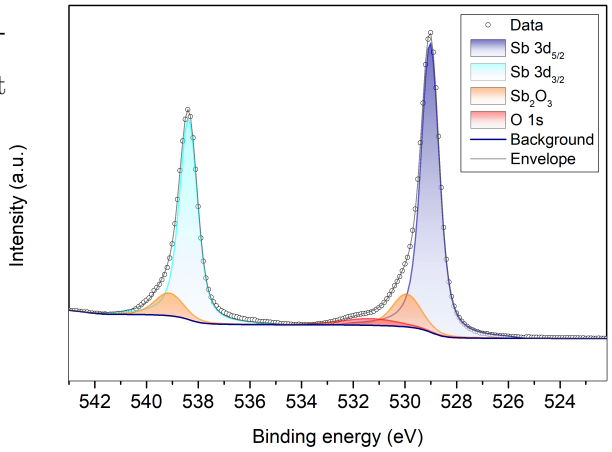

Figure 4.6: Zone of the XPS survey on the annealed sample after the RTP oven fix, showing negligible presence of oxygen.

Finally, the surface of the films was analyzed by the XPS technique. Figure 4.6 shows no significant presence of oxygen, which is represented by the O 1s peak at a binding energy of around 531 eV. A small peak can be found at 530 and 539 eV corresponding to the Sb_2O_3 phase. Completely eradicating this phase from the surface of the film is virtually impossible, since the antimony-based material reacts with atmospheric oxygen even at low temperatures, resulting in slow, natural oxidation, and subsequent formation of a residual amount of Sb_2O_3 [58]. Oxygen

presence during the annealing step will likely cause the replacement of S^{2-} and Se^{2-} ions by the O^{2-} in the lattice [79]. Due to the sensitivity of the antimony chalcogenide materials to the presence of oxygen at high temperatures, we conclude that maintaining an inert atmosphere during the annealing process is crucial in order to obtain pure $Sb_2(S, Se)_3$.

4.2 Annealing Temperature Optimization

After being able to produce a contaminant-free $Sb_2(S, Se)_3$ film, a annealing temperature optimization study was performed. Annealing provides a thermodynamic force to promote crystallization, grain growth and release internal stresses in the as-deposited $Sb_2(S, Se)_3$. Annealing treatment optimization studies have been performed in the past, although most of these studies were only descriptive in nature and always performed on $CdS/Sb_2(S, Se)_3$ [43, 61]. Furthermore, annealing conditions may vary from system to system. For example, the annealing process may have different outcomes depending if it was performed in an hotplate or tubular oven.

The experimental details of the implemented annealing treatment can be consulted in Chapter 3. In this study, the as-deposited $Sb_2(S, Se)_3$ was annealed at 250°C, 300°C, 350°C and 400°C, and the resulting samples were investigated to understand the impact of the annealing temperature on the structural, morphological and optoelectronic characteristics of the films.

4.2.1 Morphology

SEM analysis was first performed to assess the morphology of the annealed films. Figure 4.7 shows top-view imagery of the $Sb_2(S, Se)_3$ layer annealed at 250°C, 300°C, 350°C and 400°C. At annealing temperatures of 250°C and 300°C, minimal variations are observed in the morphology of the film. However, as the annealing temperature is raised to 350°C, the grains start to coalesce, resulting in a denser and more compact film structure. Subsequently, at an annealing temperature of 400°C, the grains exhibit signs of deterioration, characterized by the loss of well-defined boundaries and their characteristic rounded morphology. Additionally, the film shows an increase in the size of voids or holes present within the structure. This is likely due to the excessive expansion of the film and evaporation of material for high annealing temperatures [55]. Naturally, this is detrimental, as the increase of structural defects will act as recombination centers in the film. Furthermore, a rough surface will hinder the quality of the interface with the subsequent HTL, due to poor contact between layers.

A cross-sectional view of the samples further emphasizes these changes. As we can observe in

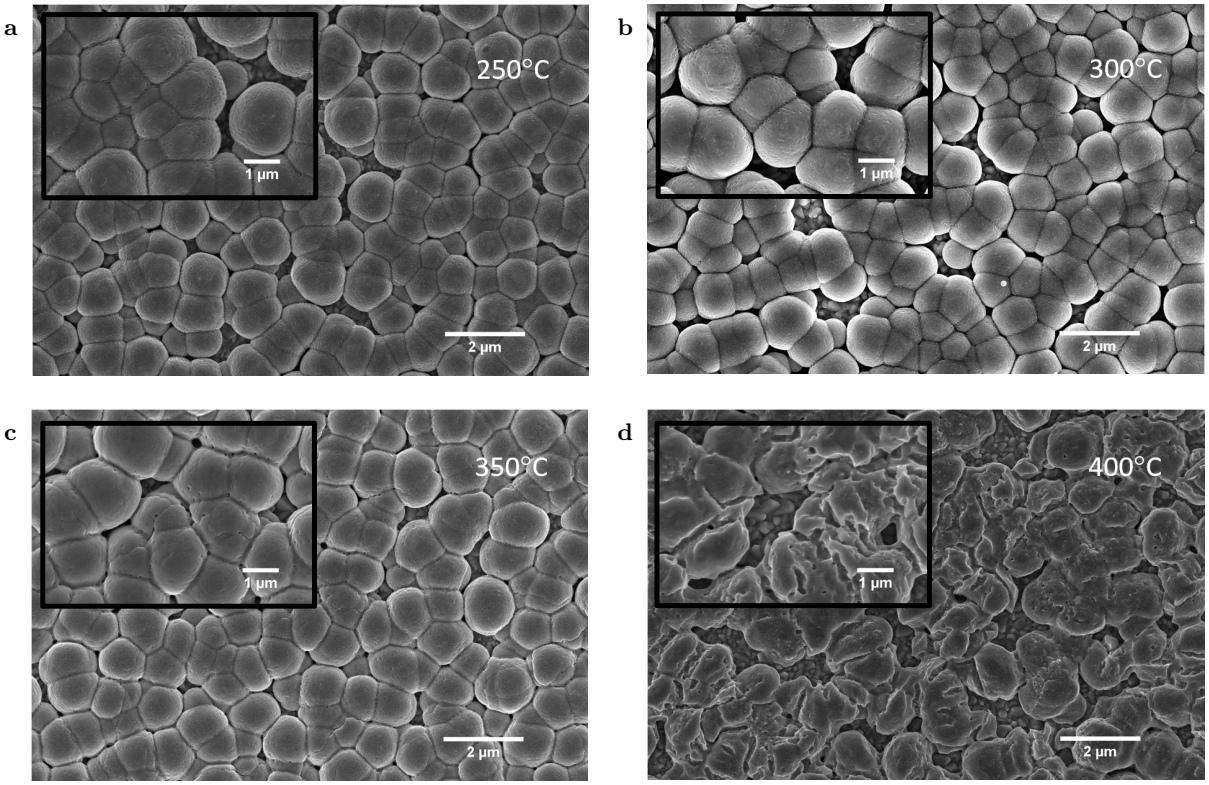

Figure 4.7: Top-view SEM of $Sb_2(S, Se)_3$ annealed at **a.** 250°C **b.** 300°C **c.** 350°C **d.** 400°C.

figure 4.8, the annealed films present beneficial vertical crystal growth, especially for a 350°C annealing temperature. Furthermore, increasing the temperature for 400°C causes the deterioration of the films, with very rough morphology and uneven thickness, which is awful for planar solar cells.

Figure 4.9 shows the distribution of grain size and film thickness with annealing temperature. For 400°C, grain size could not be accurately measured as there are no well-defined grain boundaries. It can be observed that the film thickness exhibits a decreasing trend with increasing temperature. This behavior can be attributed to the aforementioned horizontal diffusion process and the potential evaporation of material from the film's surface. The increasing thermal energy contributes to higher atomic mobility, thereby facilitating the diffusion of atoms across the film surface in accordance with Fick's laws of diffusion. Moreover, surface tension usually decreases with temperature, due to a reduction in intermolecular cohesive forces [80], which may contribute to a more compact and thinner film. Finally, due to the relatively low melting point of Sb_2S_3 and Sb_2Se_3 (table 2.1), material evaporation becomes more significant as the temperature rises, further contributing to the lower thickness of the films.

Overall, we can conclude that the 350°C annealing temperature seems to present the more

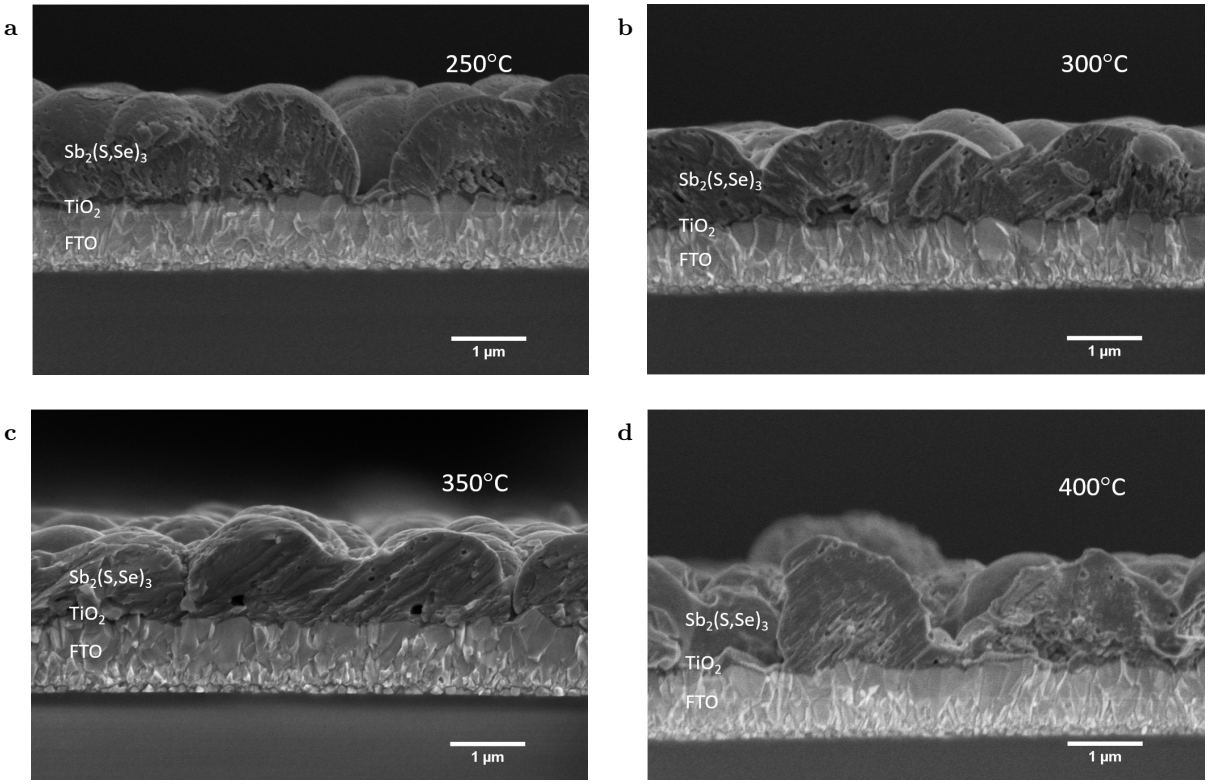

Figure 4.8: Cross-sectional SEM of $Sb_2(S, Se)_3$ annealed at **a.** 250°C **b.** 300°C **c.** 350°C **d.** 400°C.

compact and uniform morphology, with large grains and well-defined grain boundaries.

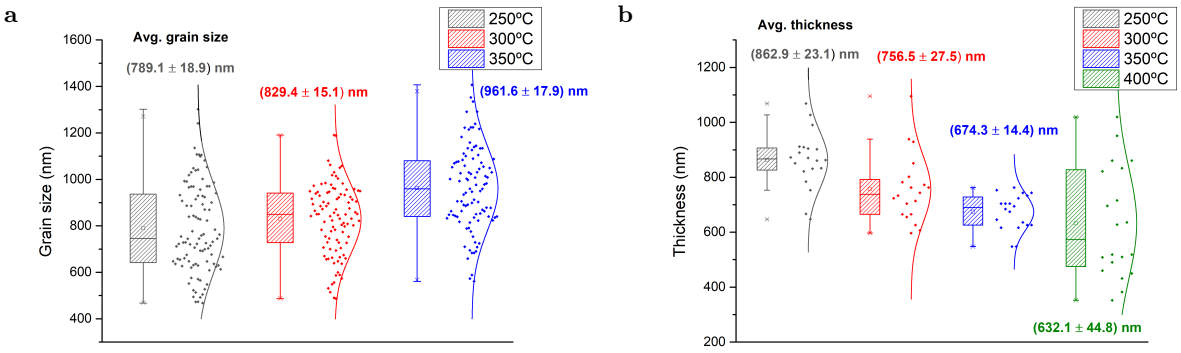

Figure 4.9: Annealing temperature influence on: **a.** grain size and **b.** film thickness of the $Sb_2(S, Se)_3$ thin films.

4.2.2 Crystallinity

The quasi-one-dimensional (quasi-1D) structure of antimony chalcogenide films offers opportunities to enhance carrier transport by manipulating the orientation of the crystallites. Although it does not give a definitive answer about the predominant crystal growth in the films, vertically

oriented grains, likely corresponding to (hk1) planes, can already be seen in the cross-sectional images of the films annealed at 350°C (figure 4.8). To understand the impact of the annealing temperature on crystallite size and orientation, Bragg-Brentano XRD analysis was performed. Figure 4.10a shows the X-ray diffractogram, with 2θ expanding from 10 to 35 degrees. This range contains the main diffraction peaks for the $Sb_2(S, Se)_3$ material. As stated in Chapter 3, the $Sb_2(S, Se)_3$ peaks usually occur in-between the reference diffraction angles of the Sb_2S_3 and Sb_2Se_3 cards. Unfortunately, no $Sb_2(S, Se)_3$ reference cards exist, as the relative selenium and sulfur content is variable. For this reason, the standard Sb_2S_3 JCPDS 42-1393 and Sb_2Se_3 JCPDS 15-0861 cards were used as reference for the identification of the diffraction peaks.

As can be seen in figure 4.10a, diffraction peaks corresponding to the standard crystal planes of the antimony chalcogenide materials appear after annealing and are in accordance with the reference cards. The XRD results further show that the as-deposited films present very low crystallinity, with no $Sb_2(S, Se)_3$ peaks being identified. These results further emphasize the necessity of an annealing procedure after the low-temperature hydrothermal synthesis.

Crystallite size can be obtained from the Debye-Scherrer equation (equation 3.2). In this study, a shape factor of $K = 0.94$ was utilized to account for spherical crystallites, along with the characteristic Cu kα wavelength, $\lambda = 0.154$ nm. Gaussian functions were employed to fit the Full Width at Half Maximum (FWHM) values of all peaks in the diffractogram. The value of the crystallite size averaged over all peaks for each annealing temperature can be seen in figure 4.11a. As expected, crystal size tends to increase with annealing temperature, especially for the higher 350°C and 400°C temperatures [81]. This is in agreement with the morphological changes observed in figure 4.9. Larger crystal sizes are beneficial for photovoltaic performance, due to reduced grain boundaries and defects, that may act as recombination centers, enhancing the diffusion length of charge carriers.

Figure 4.10 shows some portions of the diffractogram that contain the most intense (hk0) and (hk1) peaks (in bold), which are normally used to study crystal orientation in $Sb_2(S, Se)_3$ films [43, 61]. Although the (121) plane is not commonly used, the intensity of this peak was to great to be ignored, especially for the 400°C annealing temperature. Deconvolution of the peaks was performed and they were fitted with Gaussian functions, allowing us to estimate their intensity. Based on equation 3.4, the relative intensity ratio between (hk1) and (hk0) planes was calculated (figure 4.11b). By comparing the intensity ratios between annealing temperatures, we can assess the impact of this parameter on crystallite orientation.

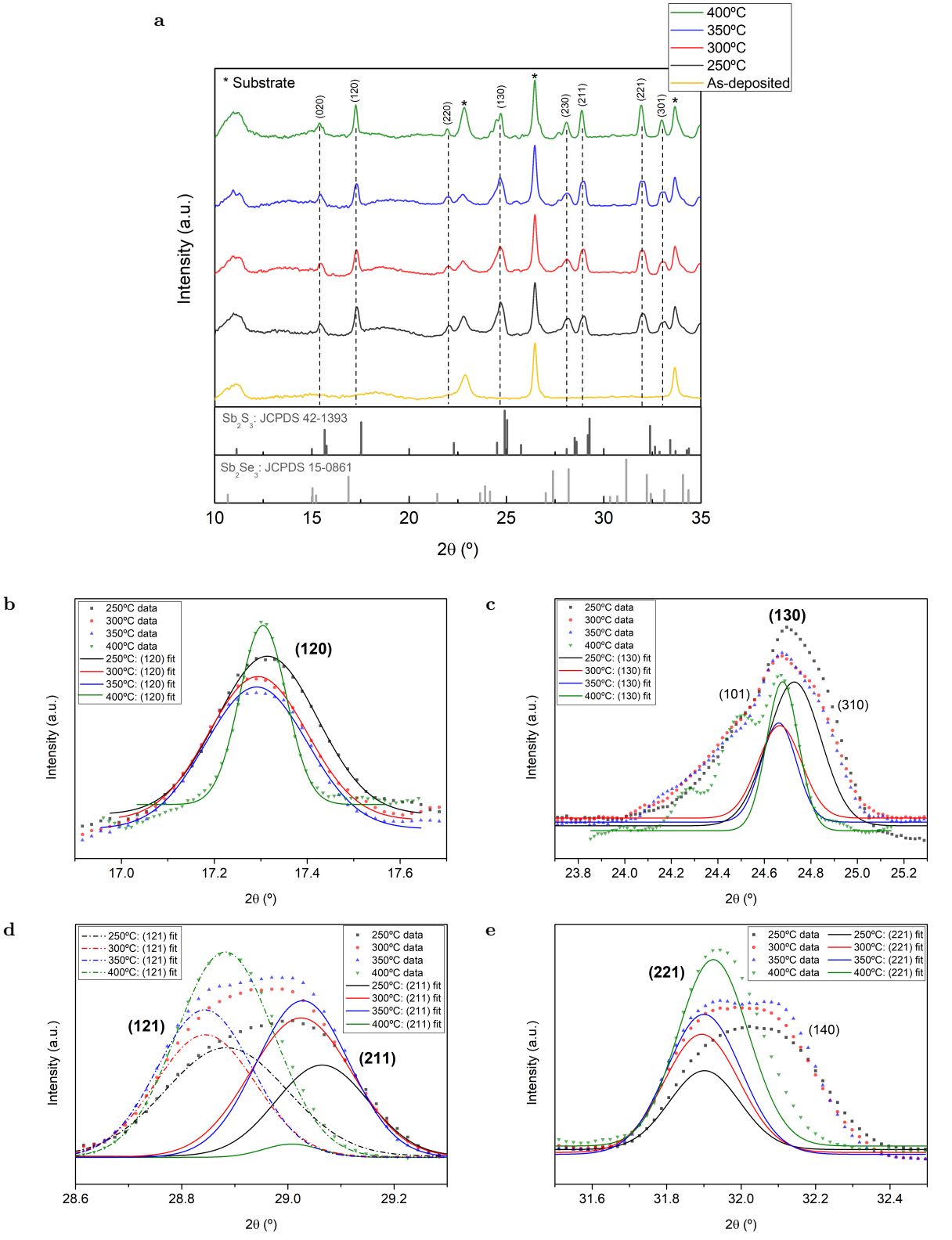

Figure 4.10: **a.** Diffractogram of the as-deposited and annealed films for annealing temperatures of 250°C, 300°C, 350°C and 400°C, with Sb_2S_3 and Sb_2Se_3 references. Gaussian fit of the XRD data for the different annealing conditions of the **b.** (120) peak **c.** (130) peak **d.** (121) and (211) peaks **e** (221) peak.

In terms of crystal orientation, it appears that the 350°C annealing temperature exhibits more favorable vertical growth of crystalline grains relative to the substrate. This is evidenced by higher (hk1)/(hk0) intensity ratios for most plane pairs, with only two exceptions. For 250°C and 300°C, lower crystallinity and a more horizontal configuration of crystallites will decrease the diffusion length of charge carriers, by introducing defects and promoting transport through grain boundaries. Increasing the annealing temperature from 300°C to 350°C results in a subtle reduction in the intensity of the (hk0) peaks and a concurrent enhancement in the intensity of the (hk1) peaks, indicating a relative shift towards vertical crystal planes. Although for the 400°C temperature the (221) peak is quite intense, demonstrating a great presence of this crystal plane in the film, the almost disappearance of the very favorable (211) peak (figure 2.3) will certainly affect charge transport in the absorber layer. Furthermore, for this temperature, the films suffer from a great presence of the (120) and (130) planes, which is not ideal.

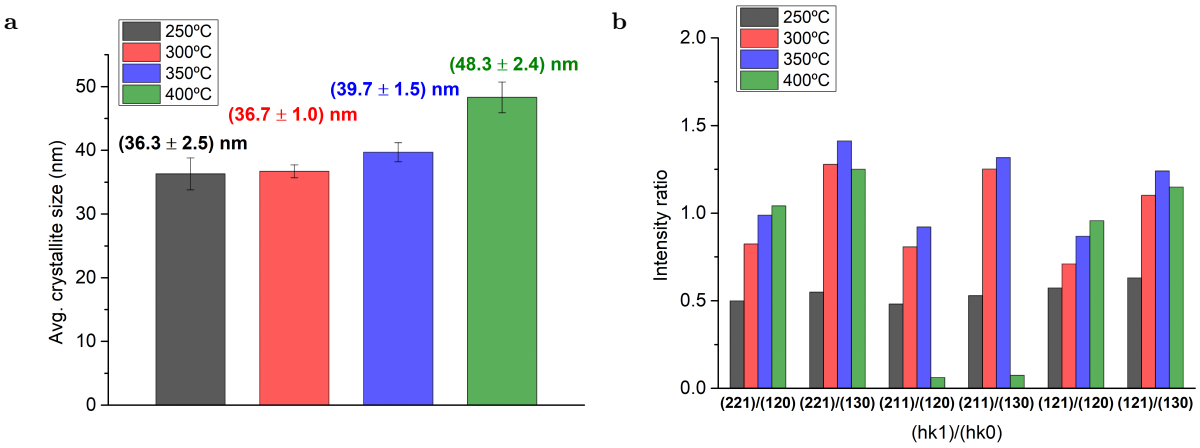

Figure 4.11: **a.** Annealing temperature influence on crystallite size **b.** Intensity ratios for the main (hk1) and (hk0) planes for different annealing temperatures.

4.2.3 Optical Bandgap

In order to obtain the bandgap of the $Sb_2(S,Se)_3$ films, transmission data was obtained from UV-Vis-NIR measurements. Tauc plots for $\gamma = 1/2$ (direct bandgap) and $\gamma = 2$ (indirect bandgap) were drawn for amorphous and annealed films by using equation 3.10. Figure 4.12 shows both plots with the linear fits and respective bandgaps obtained through the Tauc method, as explained in Chapter 3.

As we can observe from figure 4.12, the linear region corresponding to the absorption edge can be clearly identified. In addition, deviations from linearity at the low energy end of this edge can be associated with defect absorption states, denominated as an Urbach tail [82].

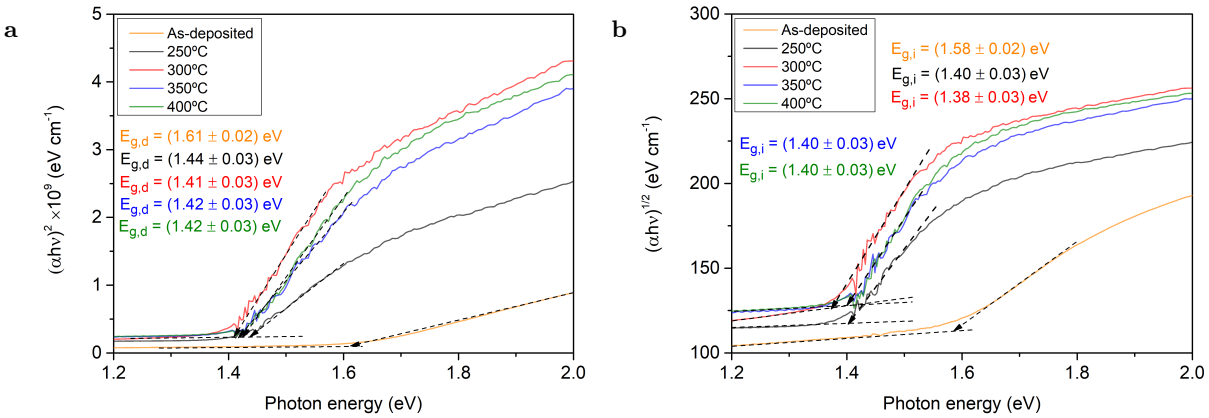

Figure 4.12: Tauc plots of the as-deposited and annealed films for the determination of the **a.** direct bandgap ($\gamma = 1/2$) **b.** indirect bandgap ($\gamma = 2$).

Both for $\gamma = 1/2$ and $\gamma = 2$, the Tauc plot provides good fits in the linear region, indicating that the fabricated $Sb_2(S, Se)_3$ has direct and indirect transitions. Furthermore, the difference between the direct and indirect bandgap energies ($\Delta\,(E_{g,d} - E_{g,i})$) is small for all conditions, which is in agreement with theoretical calculations for the band structure of antimony chalcogenide materials [83]. This indicates that the $Sb_2(S, Se)_3$ film has a flat band structure. Flat electronic bands in Sb_2S_3 and Sb_2Se_3 are associated with improved light absorption due to an high density of states near the valence and conduction band extremes [84]. Finally, the band structure of the antimony chalcogenide materials is indicative of its anisotropy. Theoretical calculations determined that the electronic bands are flatter along the [100] and [010] directions, corresponding to higher effective masses for charge carriers, as described by equation 4.1 (where $\hbar$ is the reduced Planck's constant and $\frac{d^2E_k}{dk^2}$ is the second derivative of the energy function of the particle in momentum space). Conversely, the bands demonstrate higher curvature (increased dispersion) along the [001] direction, indicating facilitated charge transport [83].

$$m^* = \pm\hbar^2 \left(\frac{d^2 E_k}{dk^2} \right)^{-1} \tag{4.1}$$

The direct and indirect bandgap remain overall constant for all annealing temperatures, indicating that augmenting this parameter for temperatures higher than 250°C does not influence the absorption edge of the material. Nonetheless, we can observe a drastic decrease in bandgap after the annealing process. This may be interpreted by the improvement of crystalline quality and structural order caused by the annealing process, leading to well-defined energy bands and a narrower bandgap [85]. This results confirm the transition from low to high crystalinity with annealing, which is in accordance to the XRD results.

4.2.4 Composition

The composition of the $Sb_2(S, Se)_3$ material has a considerable impact on the properties of the film. Namely, achieving a suitable Se/(S+Se) atomic ratio allows for bandgap tuning, a compact morphology and suitable crystal orientation [43]. To assess the composition of the annealed films, as well as its sensitivity to the temperature of the annealing process, XPS and EDS were performed. While XPS is a surface technique, providing accurate measurements of element quantification at the top nanometers of the film, EDS allows for a bulk-level composition study.

Figure 4.13 shows the XPS region corresponding to the S 2p and Se 2p orbitals. The Se/(S+Se) atomic ratio was determined by considering the peaks S $2p_{3/2}$ and Se $2p_{3/2}$, as they are the more intense peaks, allowing for less error in the measurements. The Se/(S+Se) atomic ratios were determined from the fittings by using equation 3.8.

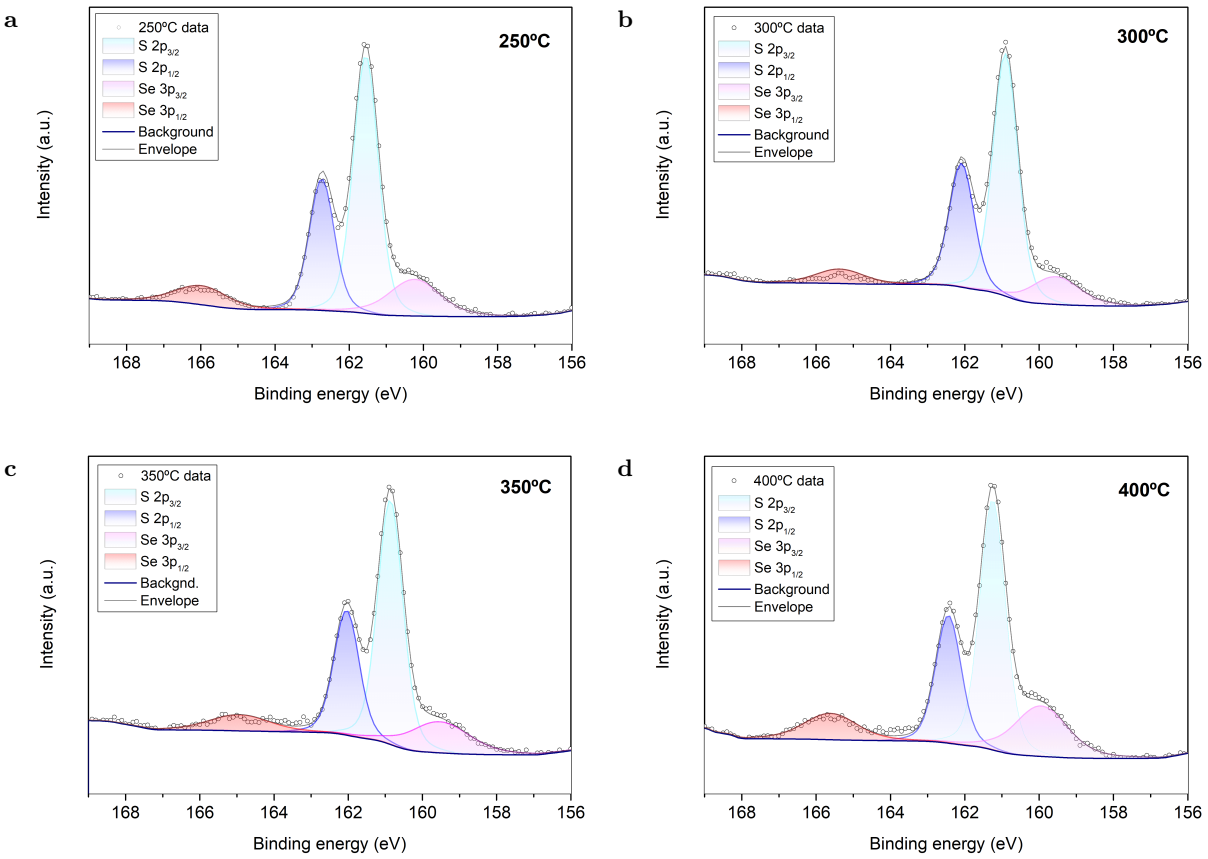

Figure 4.13: XPS region of the S 2p and Se 3p peaks of $Sb_2(S, Se)_3$ annealed at **a.** 250°C **b.** 300°C **c.** 350°C **d.** 400°C.

Moreover, EDS was performed on all samples at an acceleration voltage of 15 kV, allowing for

a deeper composition analysis of the films. Finally, through analysis of the previously obtained UV-Vis-NIR data, it is possible to estimate the Se/(S+Se) atomic ratio, as the optical bandgap of the hydrothermally deposited $Sb_2(S, Se)_3$ only depends on this parameter, as demonstrated on previous studies [43]. Yang et al [70] showed that the direct bandgap of $Sb_2(S_{1-x}, Se_x)_3$ materials can be described by equation 4.2, where x is the Se/(S+Se) atomic ratio.

$$E_g(x) = 0.118x^2 - 0.662x + 1.621\text{eV} \tag{4.2}$$

Table 4.4 and figure 4.14 show the Se/(S+Se) ratio obtained through the different characterization techniques. Firstly, it is possible to observe that we obtain significant differences in concentration depending on the characterization technique used. As previously mentioned, XPS and EDS are surface and bulk techniques, respectively. This indicates that the $Sb_2(S, Se)_3$ material is not uniform, suggesting a lower selenium concentration at the surface of the film that increases as we penetrate in depth. Moreover, the bandgap obtained from the UV-Vis measurements is the lowest in the film, as explained in Chapter 3. By analyzing equation 4.2, we can conclude that the direct bandgap decreases with increasing Se concentration, meaning that the UV-Vis values presented in table 4.4 correspond to the highest Se/(S+Se) ratios in the films.

Table 4.4: Values for the Se/(S+Se) atomic ratios with annealing temperature.

	Annealing temperature (ºC)			
	250	300	350	400
XPS: Se/(S+Se) (%)	9.5	7.6	10	13.4
EDS: Se/(S+Se) (%)	19.1	21.3	23.4	24.7
UV-Vis: Se/(S+Se) (%)	30.5	33.9	32.2	32.2

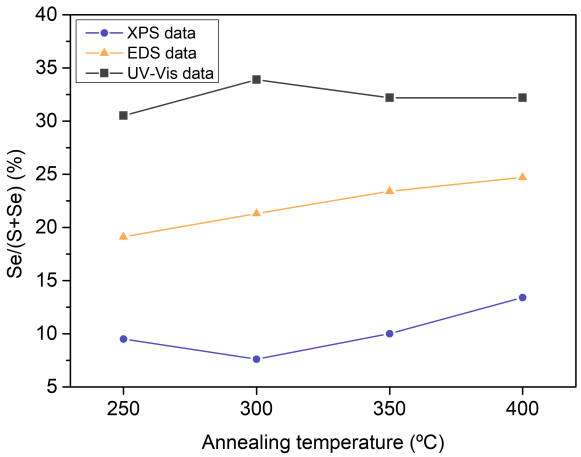

Figure 4.14: Graphical comparison of the Se/(S+Se) atomic ratios with annealing temperature.

The obtained results indicate the formation of a S/Se gradient in the prepared films by the hydrothermal method. Zhao et al [17] stated that, as growth progresses, the selenium concentration tends to decrease and is gradually replaced by sulfur ions in the lattice. This creates a steep

gradient from the bottom to the top of the film, which explains the much higher concentration of sulfur determined by the XPS technique. This gradient should have a detrimental impact on charge transport, as it will cause an internal electric field that obstructs hole transport and creates recombination centers in the absorber layer [44].

Naturally, this gradient should have a significant impact on the band structure of the $Sb_2(S, Se)_3$ thin films. Increasing the selenium concentration will cause an upshift of the valence band, while maintaining the conduction band unaltered [43]. This should have an impact on band alignment, namely with the HTL layer.

Furthermore, we can observe that, for higher annealing temperatures, the selenium concentration tends to increase for the XPS and EDS data, while for the UV-Vis estimation, the Se/(S+Se) ratio tends to be somewhat independent from temperature, as the determined bandgap is overall constant (figure 4.12). This results can be interpreted by the evaporation of material from the surface of the gradient film. For higher temperatures, the increased evaporation rate of the shallower sulfur-rich region will expose a zone with a higher concentration of selenium, as represented in figure 4.15. This conclusion is supported by the reduced thickness with increasing annealing temperature, as presented in figure 4.9b. Finally, because this modifications occur at more superficial layers, the deeper layers near to the substrate are not affected by evaporation. This is in agreement with the relatively temperature independent Se/(S+Se) ratios estimated from the UV-Vis measurements, indicating that the highest selenium concentration should be located at the bottom of the film.

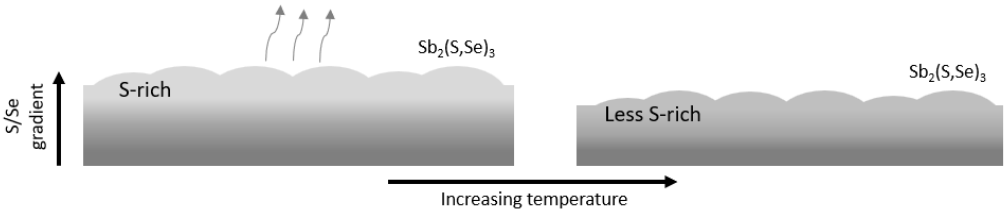

Figure 4.15: Schematics of the evaporation process of material from the surface of the film for high annealing temperatures, exposing a less S-rich region.

In particular, for the 400°C annealing temperature, the extreme evaporation of material increases the voids present in the films, as can be clearly seen in figures 4.7d and 4.8d. This exposes the Se-rich inner regions, which explains the higher concentration of this element detected from the XPS and EDS techniques.

Based on these results, we can conclude that for higher annealing temperatures, the evaporation of sulfur from the film's surface produces a more homogeneous layer, which is beneficial for charge transport in antimony chalcogenide materials. Moreover, it is possible to infer that controlled evaporation of gradient $Sb_2(S,Se)_3$, and subsequent production of more uniform films may have a significant impact on band alignment, in particular with the HTL layer. By optimizing the band structure of the $Sb_2(S,Se)_3$/HTL interface through sulfur etching of the surface layers, it was possible to obtain increased efficiencies in PV devices [17]. Nevertheless, if the evaporation is extreme due to an excessive temperature, the films may deteriorate, as shown by figures 4.7d and 4.8d.

Overall, the results of this study indicates that annealing $TiO_2/Sb_2(S,Se)_3$ films at a 350°C temperature produces the best characteristics for applications in solar cells. Firstly, films annealed at 350°C present the best morphology, with a more compact and uniform grain structure, with a flatter surface. Moreover, crystallite orientation along the [hk1] direction is optimized for this temperature, which is beneficial for charge extraction. Finally, the controlled evaporation of sulfur from the upper layers of the gradient film produced a more homogeneous material, without compromising its morphology. This was the optimal annealing temperature attained in literature for most of the previous studies dealing with $CdS/Sb_2(S,Se)_3$ structures [43, 61], which may indicate that the optimal annealing temperature for $Sb_2(S,Se)_3$ materials is independent of the substrate where it is grown.

4.3 NaF Post-Deposition Treatment

To study the effects of a post-deposition treatment with NaF, a second hydrothermal synthesis was conducted on test samples, according to the procedures described in Chapter 3. A NaF solution post-treatment has been shown to improve the performance of $Sb_2(S,Se)_3$ solar cells by passivating defects at the surface of the film, while promoting better band alignment with the subsequent HTL layer [17].

Firstly, SEM analysis was performed to see if the NaF PDT would influence the morphology of the deposited films, although no apparent impact were observed, as shown in figure 4.16. Nevertheless, the thickness of the NaF treated samples seems to slightly decrease with respect to control samples. This may indicate that the second hydrothermal process with the alkaline NaF solution removes some of the $Sb_2(S,Se)_3$ material from the top layers.

In terms of XRD studies, no significant changes were observed in crystallinity, nor crystal

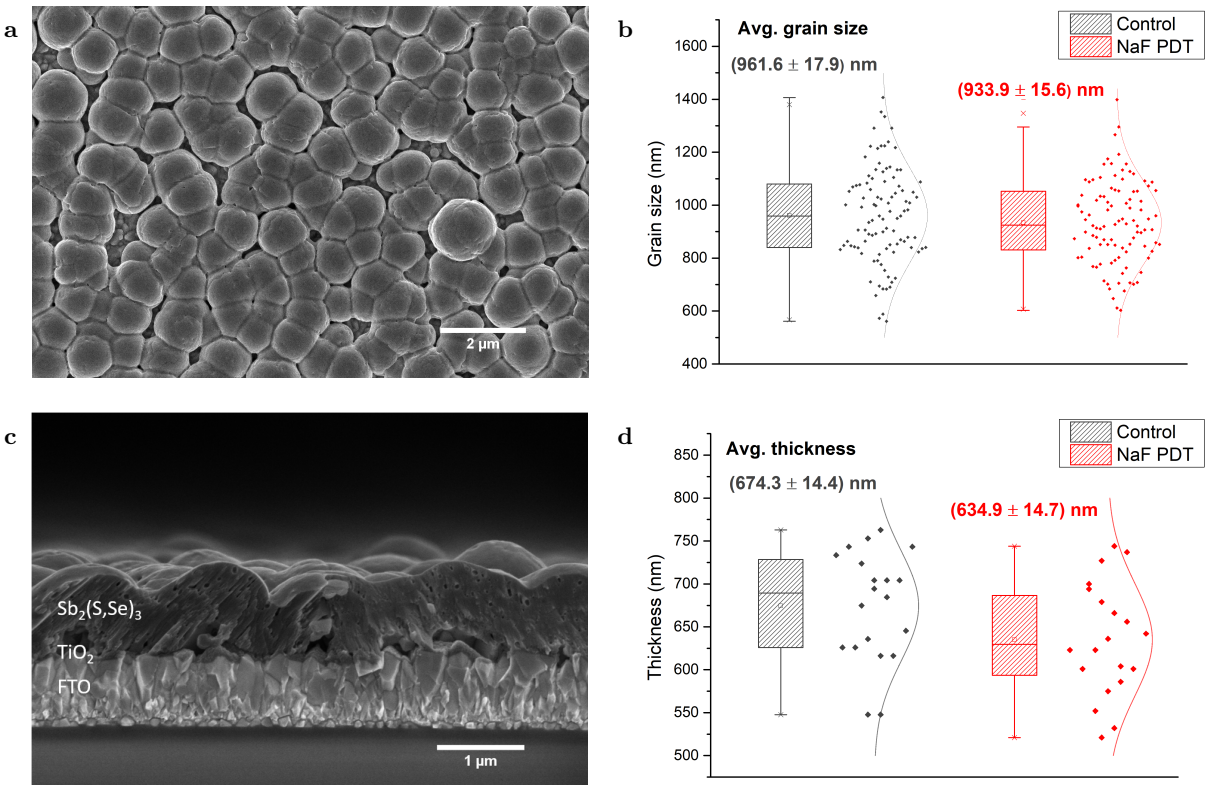

Figure 4.16: **a.** Top-view SEM image of the NaF treated $Sb_2(S,Se)_3$ sample **b.** Grain size comparison for control and NaF treated $Sb_2(S,Se)_3$ **c.** Cross-section SEM image of the NaF treated $Sb_2(S,Se)_3$ sample **d.** Film thickness comparison for control and NaF treated $Sb_2(S,Se)_3$.

orientation. However, the NaF PDT should have an impact on sample composition, as described in the previous study [17]. In parallel to the previous annealing optimization study, NaF treated samples were produced for every annealing temperature and compared to the control samples. Once again, XPS analysis was performed on several points of the NaF treated samples. To study the Se/(S+Se) atomic ratio, the region of the XPS survey corresponding to the S 2p and Se 2p orbitals was once again analyzed, as shown in figure 4.17.

Table 4.5 and figure 4.18 show the Se/(S+Se) atomic ratio determined for the NaF and control samples. It is possible to observe that the NaF PDT produces an increase in the selenium concentration, independently of the annealing condition. Furthermore, because the NaF PDT process is conducted before the annealing step, it should have a direct impact on the as-deposited $Sb_2(S,Se)_3$. It is curious to note that the increasing selenium concentration with annealing temperature subsists even for the NaF treated samples, which indicates that the effects of the NaF treatment and a follow-up annealing step are independent.

These results are in agreement with previous studies of NaF treatments based on chemical

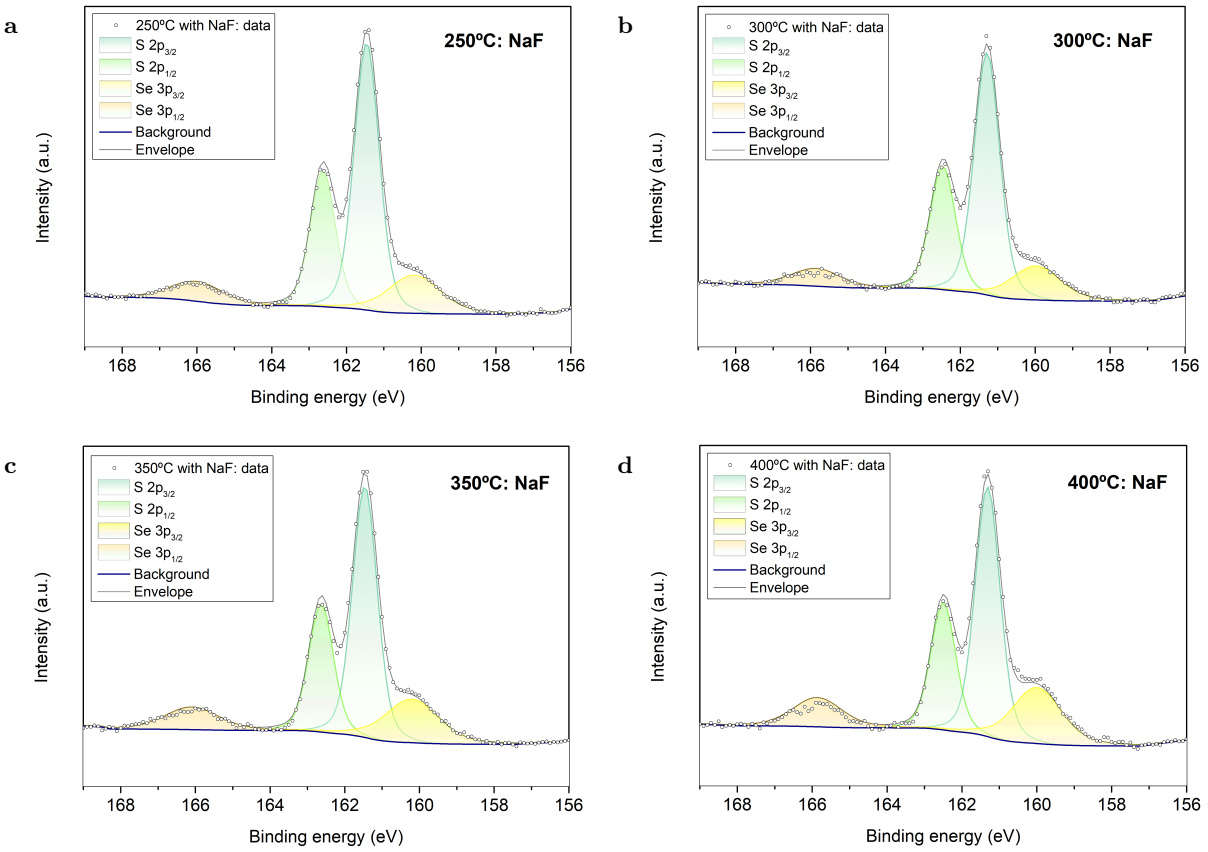

Figure 4.17: XPS region of the S 2p and Se 3p peaks of the NaF treated $Sb_2(S,Se)_3$ samples, followed by annealing at **a.** 250°C **b.** 300°C **c.** 350°C **d.** 400°C.

Table 4.5: Values for the Se/(S+Se) atomic ratios for control and NaF PDT samples.

	Annealing temperature (°C)			
	250	300	350	400
Control: Se/(S+Se) (%)	9.5	7.6	10	13.4
NaF PDT: Se/(S+Se) (%)	10	9.8	11.9	14.9

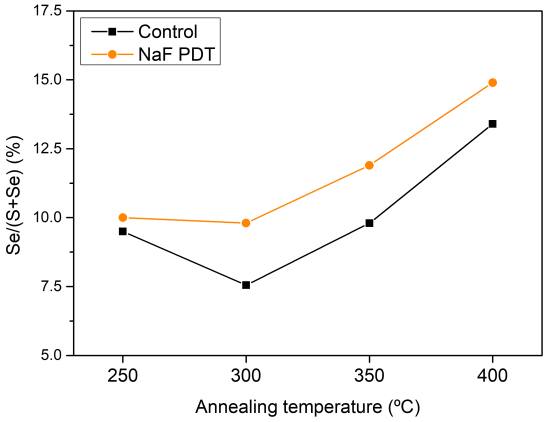

Figure 4.18: Graphical comparison of the Se/(S+Se) atomic ratios for control and NaF treated $Sb_2(S,Se)_3$.

solution processes [17]. It has been shown that antimony chalcogenides can dissolve in alkaline solutions [86, 87]. This indicates that the increased Se/(S+Se) atomic ratio should be caused by the chemical etching of the sulfur-rich top layers of the $Sb_2(S,Se)_3$ films. Moreover, this conclusion is further supported by the reduced thickness observed for the NaF treated samples

(figure 4.16d).

In a similar way to the previously discussed evaporation mechanism caused by the annealing step, the chemical dissolution of the sulfur-rich top layers of the $Sb_2(S,Se)_3$ material should produce a mild composition gradient in the film. The higher Se concentration near the Spiro-OMeTAD/$Sb_2(S,Se)_3$ interface will cause an upshift of the valence band, while maintaining the conduction band constant, as schematized in figure 4.20a. Consequently, a more favorable valence band alignment may form between the absorber and HTL layers. The elimination of the energy barriers that would otherwise form in steep gradient $Sb_2(S,Se)_3$ will facilitate hole transport, while reducing the likelihood of recombination at the interface.

The Fermi edge region of the XPS survey was analyzed for each NaF treated sample and compared with the respective control sample, as shown in figure 4.19. Unfortunately, it was not possible to perform the UPS technique in order to determine the exact values for the Fermi energy level and valence band maximum. Nonetheless, it is observable that the difference between the Fermi energy level and valence band maximum increases for all NaF treated samples. If we take into account that the NaF PDT produces the previously described upshift in valence band, it is possible to infer that an increased $\Delta = E_F - E_V$ will be caused by a larger upshift in the Fermi energy level.

By analyzing the XPS determined Se/(S+Se) ratios from table 4.5 and by using equation 4.2, the bandgap of the $Sb_2(S,Se)_3$ films can be estimated (table 4.6). As we can observe, the NaF PDT seems to transform the mostly p-type $Sb_2(S,Se)_3$ films in intrinsic or even slightly n-type semiconductors. This upshift in the Fermi energy level of the system is associated with a V_{OC} improvement for $Sb_2(S,Se)_3$ solar cells [87]. The splitting of the Fermi energy level of the absorber layer into quasi Fermi energy levels (E_{Fp} for holes and E_{Fn} for electrons) occurs due to non-equilibrium conditions caused by photon excitation and promotion of electron and holes to the conduction and valence bands, respectively (figure 4.20b). Near the HTL/$Sb_2(S,Se)_3$ interface, the absorber's E_{Fp} aligns with the HTL's E_{Fp} [88]. Subsequently, for an upshift in the Fermi energy level, the difference between E_{Fn} and E_{Fp} will increase, resulting in a V_{OC} improvement, according to equation 4.3.

$$V_{\mathrm{OC}} = (1/q)\,(E_{\mathrm{Fn}} - E_{\mathrm{Fp}}) \tag{4.3}$$

where q is the carrier's charge and E_{Fp} and E_{Fn} are the quasi Fermi energy levels for holes and electrons, respectively.

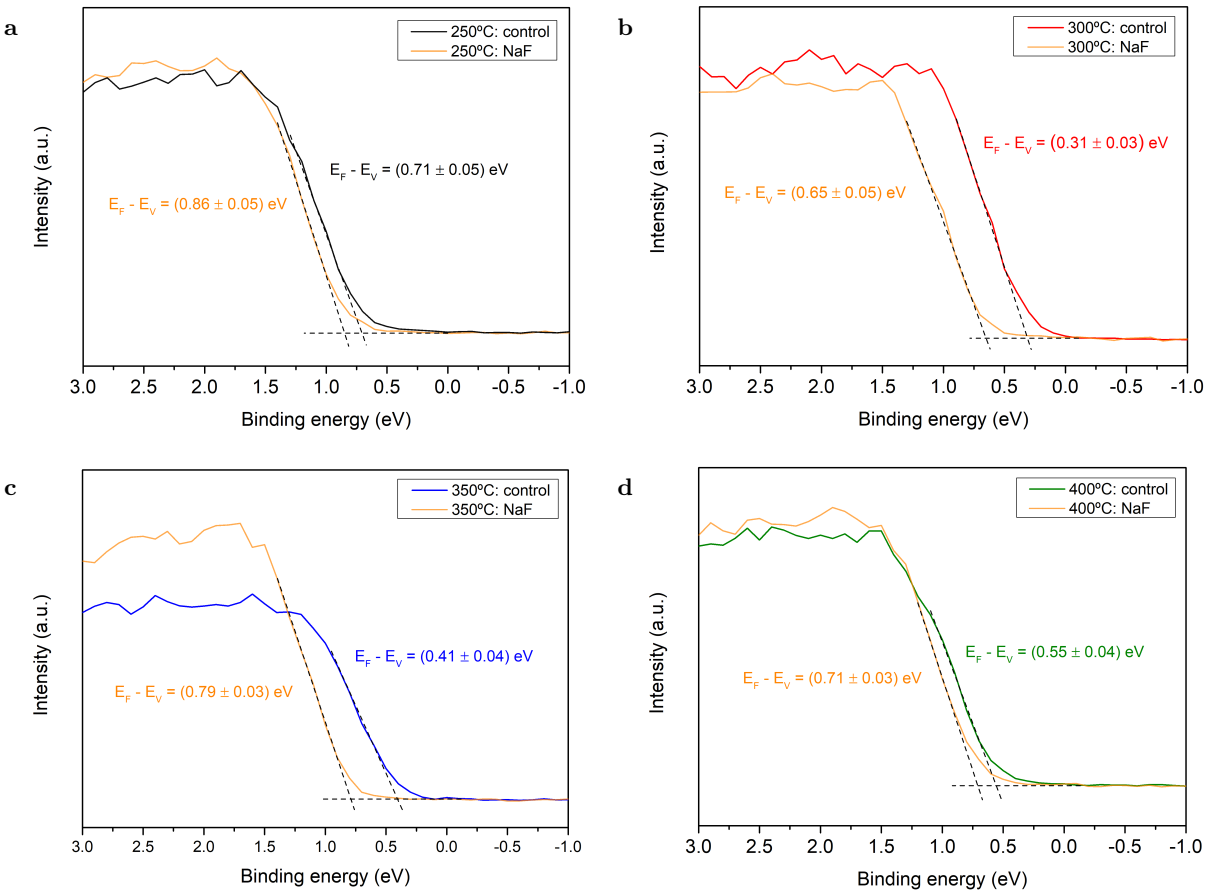

Figure 4.19: Fermi edge region of the XPS survey and determination of $E_F - E_V$ for control and NaF treated samples, followed by annealing at **a.** 250°C **b.** 300°C **c.** 350°C **d.** 400°C.

Table 4.6: Values for the estimated bandgaps, $E_F - E_V$ and $E_C - E_F$ based on the determined XPS data for the different annealing conditions and NaF treatment. $E_F - E_V$ and $E_C - E_F$ correspond to the energy differences between the Fermi level and valence band maximum, and conduction band minimum and Fermi level, respectively.

		Estimated bandgap (eV)	E_F-E_V (eV)	E_C-E_F (eV)
Sample type	250°C	1.56	0.71	0.85
	NaF PDT: 250°C	1.55	0.86	0.69
	300°C	1.57	0.31	1.26
	NaF PDT: 300°C	1.56	0.65	0.91
	350°C	1.56	0.41	1.15
	NaF PDT: 350°C	1.54	0.79	0.75
	400°C	1.53	0.55	0.98
	NaF PDT: 400°C	1.52	0.71	0.81

The observed rise in Fermi energy level may be associated with the reduction or passivation

of deep level defects in the absorber layer, due to the addition of Na^+. This is in accordance with previous studies, both for antimony chalcogenides [17], as well as other types of absorber materials, such as CIGS [89]. Nonetheless, more detailed characterization studies must be done in order to validate this hypothesis.

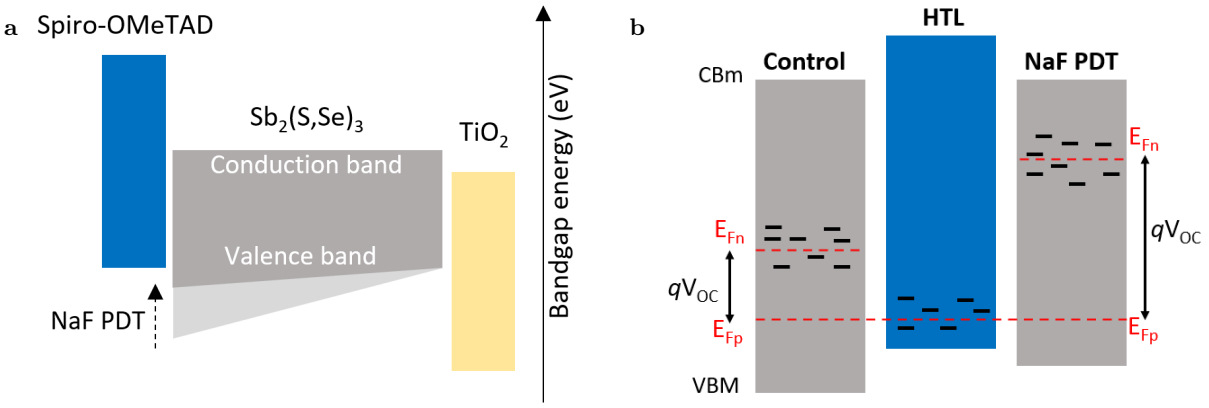

Figure 4.20: **a.** Schematic representation of the NaF-PDT on the band structure of the prepared $Sb_2(S, Se)_3$. **b.** Band alignment diagram at the interface of $Sb_2(S, Se)_3$ and the HTL, representing a potential V_{OC} improvement.

Overall, a NaF PDT has a non-negligible impact on the band structure and band alignment at the HTL/$Sb_2(S, Se)_3$ interface, seemingly having a beneficial effect. However, more detailed characterization studies are needed, as knowledge of the involved mechanisms is still rudimentary. Furthermore, because the improvements in compositional gradient are mainly due to the etching effect of the NaF alkaline solution, it is still unclear if the herein employed hydrothermal-based treatment is effective in other types of metal chalcogenide solar cells, which may be assessed by conducting further studies.

4.4 Influence of the TiO_2 ETL on the $Sb_2(S, Se)_3$ Absorber Layer

By now, this work was able to improve several parameters of the in-house hydrothermal deposition process of $Sb_2(S, Se)_3$ films. Namely, oxide contaminants were eliminated from the surface of the films. Furthermore, the annealing process was optimized for a temperature of 350°C and the NaF PDT showed potential for improving the quality of the film.

The choice of an appropriate ETL layer is of extreme importance, since it can influence the quality of the deposited absorber layer. Usually, the deposition of $Sb_2(S, Se)_3$ through the hydrothermal process is conducted on top of a CdS layer. However, for this work, a TiO_2 ETL

layer was chosen since it presents several advantages over the CdS material. Unlike the Cd-based material, it is non-toxic and has a larger bandgap, preventing absorption losses at the ETL layer.

Nevertheless, the prepared $TiO_2/Sb_2(S,Se)_3$ samples present some undesirable characteristics, in particular, with respect to the morphology of the antimony sulfoselenide layer. As can be seen in figures 4.7 and 4.16a, the deposited films present several holes and voids. This increases the risk for the formation of shunt paths, as the HTL layer may enter in direct contact with the ETL material, decreasing the shunt resistance of the final solar device and creating current leakage [78]. Curiously, this problem is not usually seen in previous studies of $CdS/Sb_2(S,Se)_3$ solar cells prepared by the hydrothermal method, which may indicate that the choice of ETL could critically influence the morphology of the prepared absorber layer.

In order to obtain a more compact film structure, several tests were done on the TiO_2 layer. Firstly, a UVO cleaning treatment was tested on the TiO_2 layer. This procedure has been shown to remove organic residues from the surface of substrates, while improving the conductivity at the interface of TiO_2-based perovskite solar cells [90]. Furthermore, contact angle tests performed at INL showed that this cleaning procedure can improve the hydrophilicity of the TiO_2 substrate (figure 4.21), which may have a positive impact on the deposited $Sb_2(S,Se)_3$, since the solvent used in the hydrothermal process is DI water. For these study, the UVO cleaning procedure was performed for 15 minutes at 150°C.

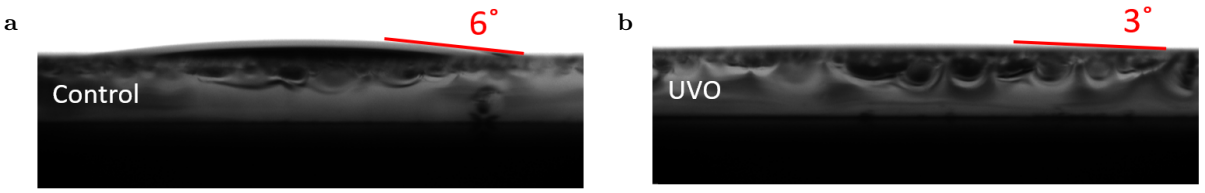

Figure 4.21: Contact angle test images of TiO_2 substrates **a.** as-prepared **b.** with UVO treatment.

The top-view SEM images of control $Sb_2(S,Se)_3$ and UVO test samples are presented in figure 4.22. The UVO cleaning treatment seems to slightly improve the compactness of the absorber film, likely due to the cleaning of organic residues from the substrate. Nevertheless, the observed differences in morphology are small and voids can still be observed in the $Sb_2(S,Se)_3$ film deposited on UVO treated TiO_2. Although the UVO treatment does not provide a definitive solution, it should still be adopted for the preparation of final solar cell devices, as it at least provides a clean substrate surface for the following depositions.

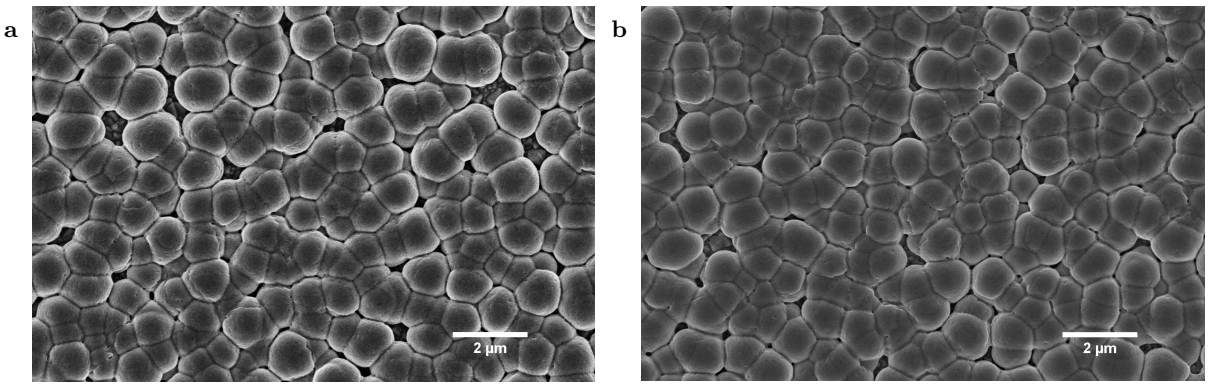

Figure 4.22: Top-view SEM images of $Sb_2(S, Se)_3$ films deposited on **a.** as-prepared TiO_2 **b.** UVO treated TiO_2.

Until now, the ETL layer had been deposited by a simple spray-pyrolysis method, described in Chapter 3. However, different deposition methods may affect the homogeneity and smoothness of the prepared TiO_2 ETL layer. Smoother substrates provide a more stable surface for film growth, resulting in better adhesion between layers [91] [92]. For these reasons, samples were prepared by synthesizing the compact TiO_2 layer through 3 different deposition methods available at INL: spray-pyrolysis, spin-coating and sputtering. Furthermore, a fourth type of sample was prepared by employing a mesoporous TiO_2 layer on top of the spin-coated compact ETL. Mesoporous TiO_2 has been shown to serve as an effective scaffold in perovskite solar cells. Its porous nature and large contact area provides increased nucleation sites for the adhesion of the subsequent layer [93]. These characteristics may be useful if the objective is to improve the compactness of the absorber film. Finally, the TiO_2 layers were cleaned by the UVO step and the $Sb_2(S, Se)_3$ films were grown and annealed at the optimized 350°C, on top of the 4 substrate types. The experimental details for all the employed deposition methods of the compact and mesoporous TiO_2 layers can be found in Chapter 3.

Figure 4.23 shows the top-view SEM images of the prepared $Sb_2(S, Se)_3$ on top of the different substrates. As it is possible to observe, the antimony sulfoselenide film deposited on top of the spin-coated titanium dioxide layer presents a much more compact structure than the films deposited on top of sprayed or sputtered TiO_2, with a substantial decrease of holes. This effect may be caused by the relatively planar titanium dioxide surface enabled by the spin-coating technique, providing a more adequate surface for subsequent depositions [94]. Nonetheless, the spin-coated $TiO_2/Sb_2(S, Se)_3$ samples suffer from non-uniform coverage, as can be seen even at the naked eye (figure A.3a, Appendix A), indicating that the areas of more favorable nucleation sites are not evenly distributed.

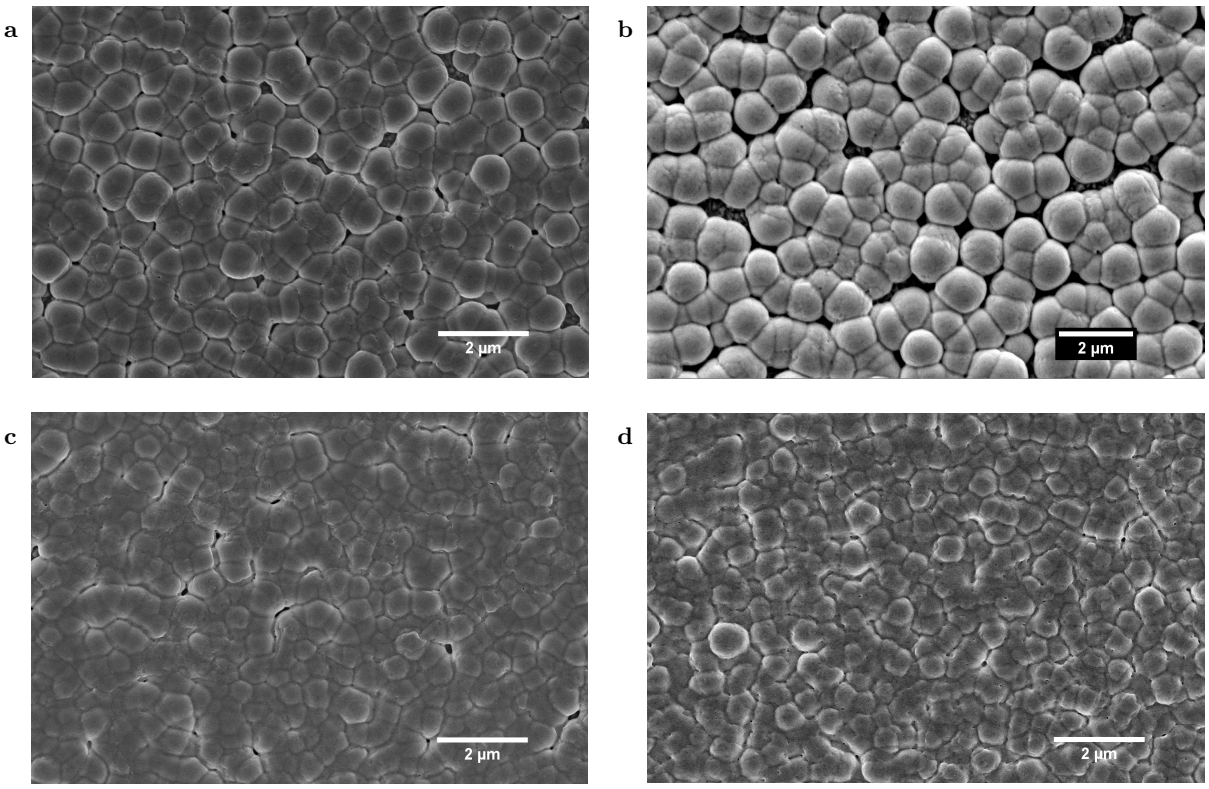

Figure 4.23: Top-view SEM images of $Sb_2(S,Se)_3$ deposited on **a.** TiO_2 prepared by spray-pyrolysis **b.**TiO_2 prepared by sputtering **c.**TiO_2 prepared by spin-coating **d.** mesoporous TiO_2.

The introduction of a mesoporous titanium dioxide structure enables a totally compact $Sb_2(S,Se)_3$ structure, definitely eliminating all the holes and voids previously observed. Furthermore, it provides uniform surface coverage of the entire substrate, as it can be seen in figure A.3b, Appendix A, and was further confirmed by SEM analysis of different points of the samples. The porous TiO_2 structure seems to act as a scaffold, providing a large surface area for the nucleation of the deposited grains. However, the subsequent larger interface between the ETL and active layer may increase the amount of recombination centers for charge carriers. Furthermore, as can be observed in figure 4.23d, the deposited absorber layer presents less defined grain boundaries, also originating grains with sizes bellow 200 nm, which could be caused by the rough nature of the porous titanium structure.

Still regarding the morphology of the deposited films, grain size was measured for the antimony chalcogenide films on top of the different substrates. The films grown on UVO-treated spray pyrolysis TiO_2 present roughly the same grain size as the previous samples annealed at 350°C, without the UVO process (figure 4.9a). Furthermore, not many changes were observed between the antimony chalcogenide material deposited on sprayed and sputtered titanium. In fact, these two substrates originated the films with larger grain sizes, but also with the highest density of

voids. Due to the larger amount of empty spaces, the as deposited grains have more room to grow during the annealing process, resulting in large, well-defined spherical grains. However, the compact spin-coated and mesoporous TiO_2 substrates produce $Sb_2(S, Se)_3$ films with much smaller grains, around half the size of the titanium dioxide ETL samples deposited by the other methods. This differences owe to the compactness of the deposited films, unlike the spray and sputtered samples. The almost void-free deposited antimony chalcogenide layer has less room to grow during the annealing step, consequently originating reduced grains.

To assess if the substrate deposition type had and influence on crystallite growth, XRD analysis of the antimony chalcogenide films was performed. As can be seen in figure 4.24a, the correct indexing of the peaks could be performed for all substrates. In fact, few conclusions could be drawn from the XRD analysis of the diffraction peaks, as no important tendency was observed. Figure 4.24b shows that the sprayed titanium dioxide substrate seems to promote a slightly more crystalline absorber film when compared to the other samples, even though the differences are small and could be inside the error margin. Regarding crystal orientation, no clear tendency was observed for the (hk1)/(hk0) intensity ratios (figure 4.24c). Consequently, there is no deposition method of the TiO_2 ETL that produces a preferably oriented or crystalline $Sb_2(S, Se)_3$ absorber layer. This indicates that the main influencing factor of crystal growth and orientation is the annealing step. Nonetheless, it is curious to note that the UVO-treated spray $TiO_2/Sb_2(S, Se)_3$ sample presents a significant increase in the average crystallite size when compared to the samples analyzed for the 350°C annealing temperature, without the UVO procedure (figure 4.11a). This result may indicate that a clean substrate is beneficial for the crystallinity of the deposited films, promoting crystallite growth.

In conclusion, some changes in morphology can be observed by varying the deposition method of the titanium ETL. In fact, while a compact ETL substrate deposited by sputtering or spray-pyrolysis results in a less compact absorber layer, synthesizing by spin coating allows for the formation of more compact areas of the $Sb_2(S, Se)$ material, even though the surface coverage at a macroscopic scale is not uniform. Furthermore, the introduction of a mesoporous layer on top of the traditional compact ETL provides with a scaffold for the growth of the antimony chalcogenide grains, providing with a very compact structure at a macro and nanoscopic level. Finally, the introduction of a UVO treatment after the ETL deposition allows for a more suitable substrate, leading to a slightly more compact absorber structure and, as preliminary studies indicate, a favorable foundation for crystal growth.

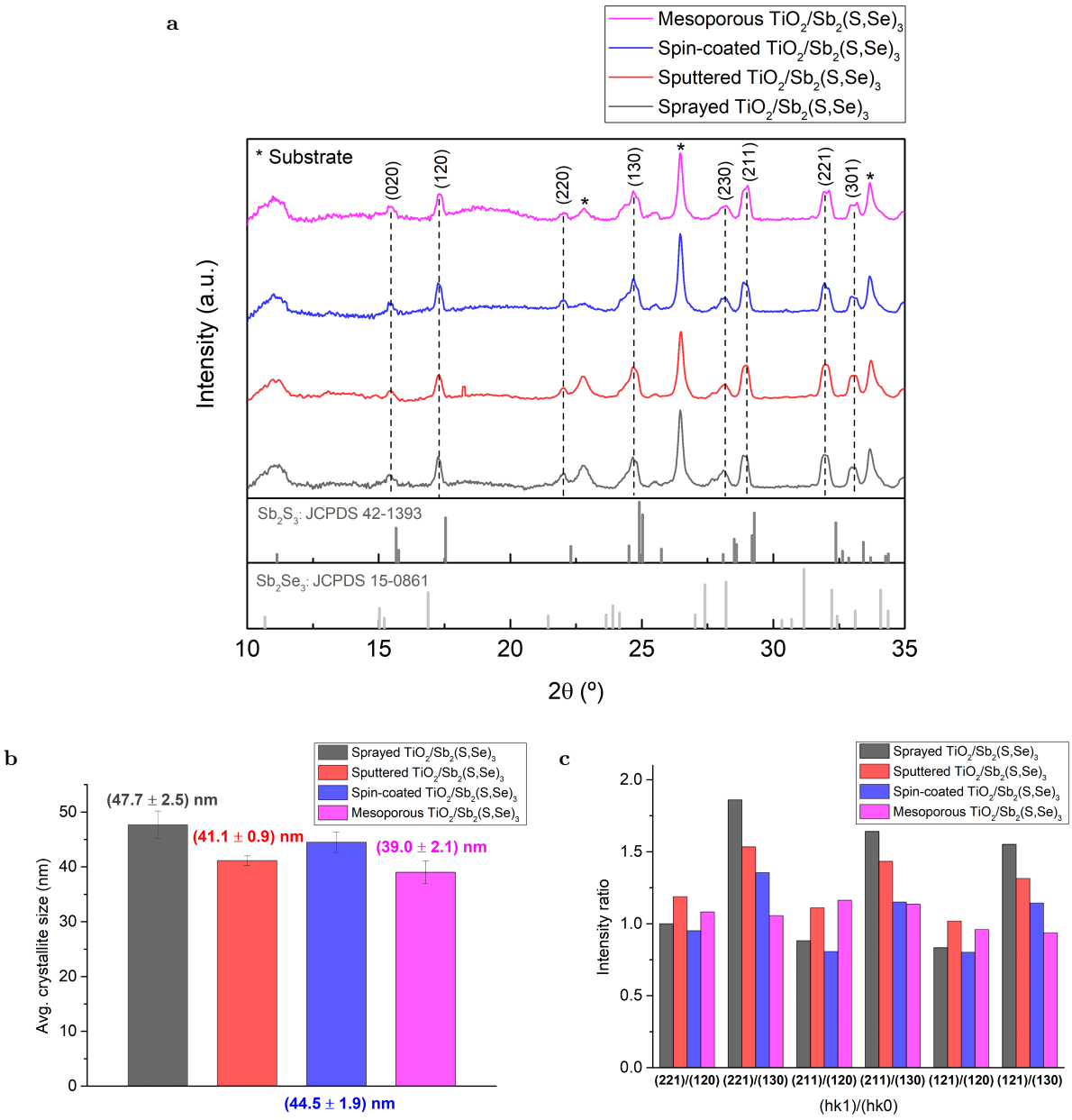

Figure 4.24: **a.** Diffractogram of $Sb_2(S, Se)_3$ films prepared on different TiO_2 substrates **b.** Crystallite size for the $Sb_2(S, Se)_3$ films prepared on different TiO_2 substrates. **c.**Intensity ratios for the main (hk1) and (hk0) planes for different TiO_2 substrates.

The non-uniform coverage and somewhat irregular surface of the deposited absorber film should arise from adhesion issues between the TiO_2 and $Sb_2(S, Se)_3$ materials. Studies employing the hydrothermal synthesis method for the preparation of Sb_2S_3 solar cells on non-toxic TiO_2 substrates faced some issues in achieving an homogeneous layer, mainly due to incompatibility between the naked TiO_2 and the antimony chalcogenide material [78, 95]. It is likely that, in our case, the TiO_2 substrate offered few nucleation sites due to the lattice mismatch between the two materials, inducing high interface energy and a resulting island-shaped $Sb_2(S, Se)_3$ film. This

problem is somewhat solved with the introduction of a scaffold mesoporous layer, where the ETL surface is functionalized due to the introduction of a large surface area structure. Nonetheless, the mismatch at the interface should still affect the extraction of charge carriers.

4.5 Photovoltaic Devices Fabrication and Results

To analyze the impact of the different substrate deposition methods on the performance of complete solar cells, as well as test the performance of the herein optimized structure, 16 devices were fabricated by finishing the samples with the addition of the Spiro-OMeTAD HTL and the gold contact, as represented in figure 2.4. Four complete PV devices were fabricated for each of the previously discussed TiO_2 substrate deposition methods.

After the fabrication of the devices, current density-voltage (J-V) curve measurements were done under a properly calibrated AM1.5G spectrum from a Oriel LSH-7320 ABA LED solar simulator. Unfortunately, only 10 of the 16 solar cell devices presented non-negligible efficiencies. Figure 4.25 shows the J-V curve parameters obtained for each cell. As we can see, the average achieved PCE was very poor, with no device surpassing the 0.4% efficiency mark (figure 4.26a). This reduced efficiency is accompanied by deficient J_{SC} and FF values, and a lacking V_{OC}. These results contrast with the champion $Sb_2(S,Se)_3$ device, which was also prepared by the hydrothermal method, although over a CdS substrate (table 4.7).

These deficient electrical parameters are likely attributed to the poor chemical bridge between the TiO_2 and $Sb_2(S,Se)_3$ layers. This hypothesis would explain the low J_{SC}, which is affected by the high density of defects at the interface and subsequent recombination of the photogenerated charge carriers. The EQE for the best cell (figure 4.26b) barely surpasses the 40% mark for all wavelengths, which is further indication of poor charge separation.

Furthermore, as can be seen in the cross-sectional images of the cells (figure 4.27), shunt paths formed due to direct contact between the ETL and HTL, which is caused by the presence of voids in the $Sb_2(S,Se)_3$ films, mainly observed for the sputtered and sprayed TiO_2 substrate samples. The presence of shunt paths leads to current leakage that does not contribute to the power output of the PV cell. This problem is well reflected in the low obtained shunt resistance (table 4.7), indicating that there is unintended low-resistance pathways that bypass the active photovoltaic region. Curiously, due to the formation of a compact $Sb_2(S,Se)_3$ film, these unwanted bridges are not observed in the samples with a mesoporous ETL, which is reflected in a higher R_{sh} and subsequent decrease in current leakage. However, the introduction of the mesoporous TiO_2

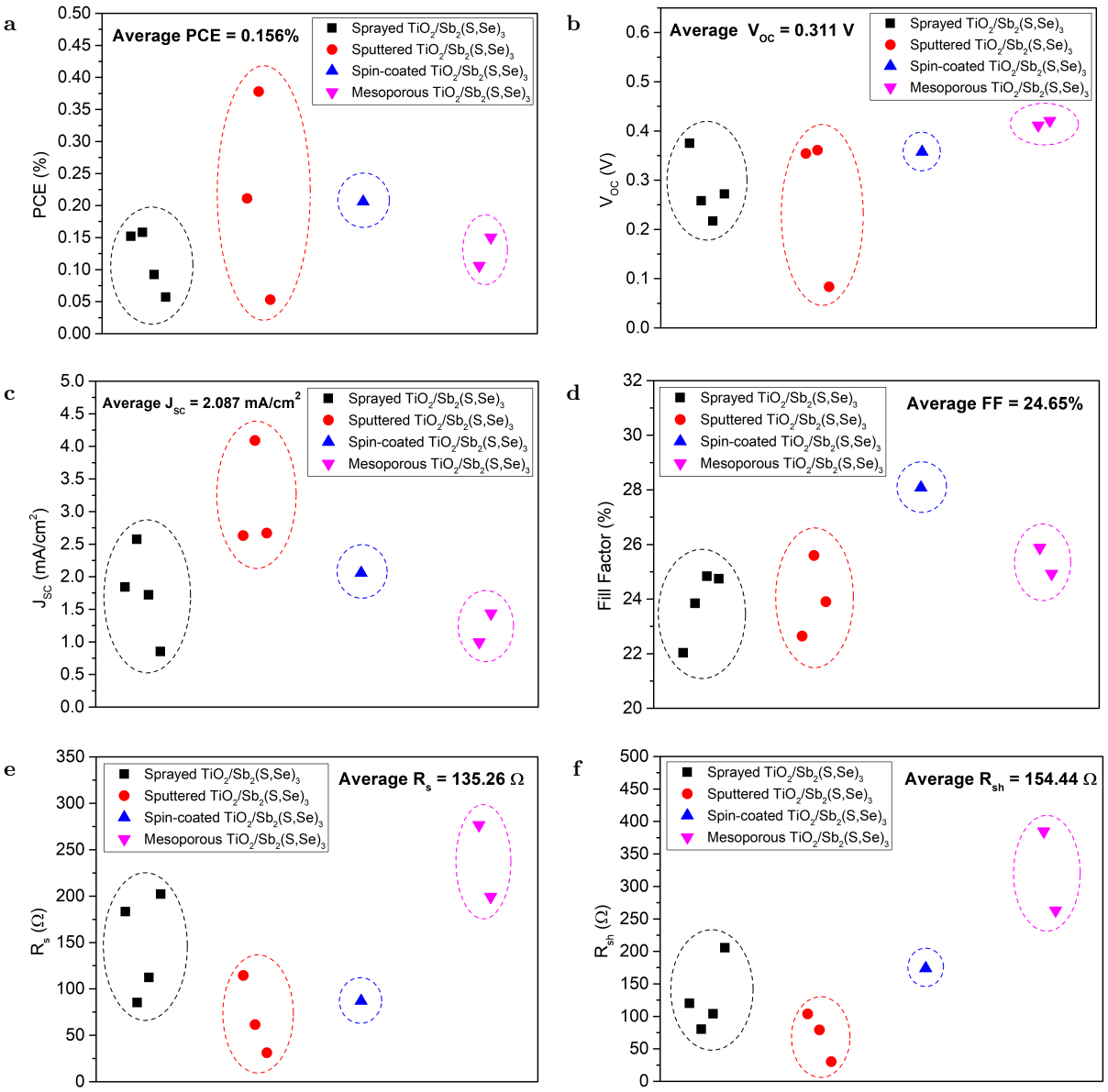

Figure 4.25: Values of **a.** PCE **b.** V_{OC} **c.** J_{SC} **d.** FF **e.** R_s **f.** R_{sh} for the non-negligeble efficiency $Sb_2(S,Se)_3$ solar devices prepared at INL.

layer also increases the series resistance of the devices, as can be seen in figure 4.25e. This effect is detrimental for charge extraction and has been reported as a potential downside of the introduction of an additional porous structure [96].

Finally, the results obtained for the electrical parameters are coherent with the morphology of the $Sb_2(S,Se)_3$ material deposited on the different substrates. By observing figure 4.23, we can see that a greater presence of voids in the films is reflected in a low R_{sh}, which is almost 10 times smaller for the sputtered TiO_2 samples than for the mesoporous TiO_2 ones (figure 4.25f). While the introduction of an additional mesoporous layer may reduce the formation of shunt paths, it

will affect charge extraction, as previously explained, resulting in high R_s and the poorest J_{SC} of all the tested solar devices.

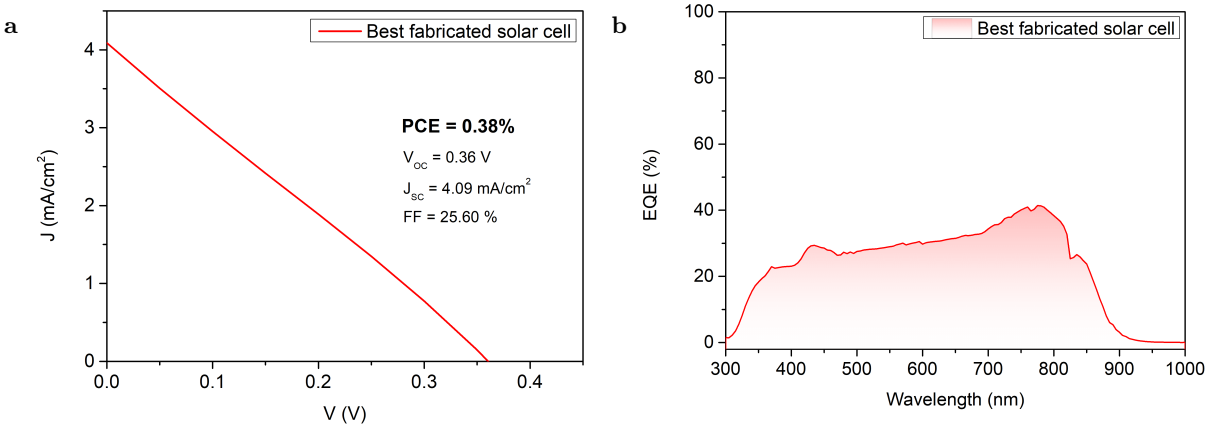

Figure 4.26: **a.** J-V curve and **b.** EQE curve of the highest PCE fabricated solar cell.

Table 4.7: Electrical parameters for the best in-house fabricated solar cell, and comparison with the performance of a TiO_2/Sb_2S_3 solar cell [78] and the champion $CdS/Sb_2(S,Se)_3$ solar cell, both prepared by the hydrothermal method.

	V_{OC} (V)	J_{SC} (mA/cm^2)	FF (%)	R_s (Ω)	R_{sh} (Ω)	PCE (%)
Best in-house fabricated cell	0.36	4.09	25.60	61.57	79.15	0.38
TiO_2/Sb_2S_3 cell [78]	0.25	7.22	28.76	330.00	495.50	0.53
$CdS/Sb_2(S,Se)_3$ cell [44]	0.63	25.27	67.35	50.34	1.02×10^4	10.75

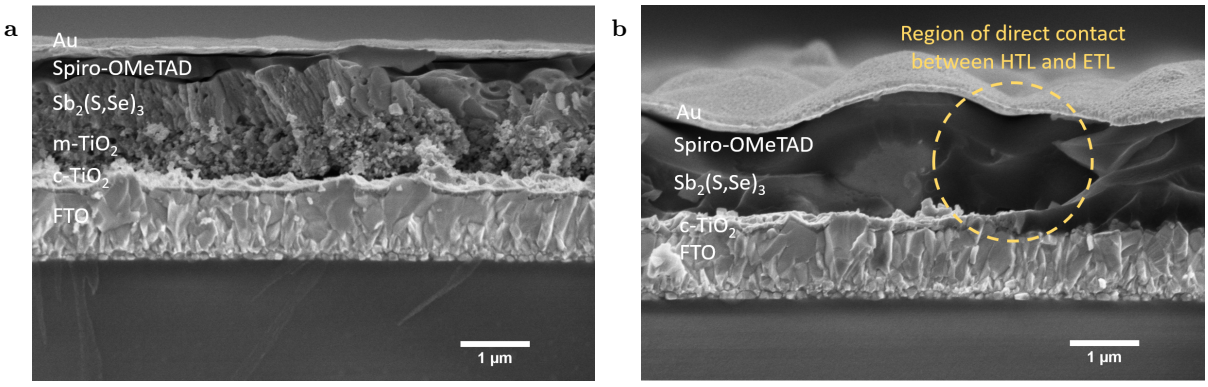

Figure 4.27: Cross-section SEM images of **a.** $Sb_2(S,Se)_3$ solar cell with a c-TiO_2 + m-TiO_2 ETL **b.** $Sb_2(S,Se)_3$ solar cell with a c-TiO_2 ETL deposited by spray-pyrolysis.

Antimony chalcogenide solar cells using a Cd-free TiO_2 ETL have been successfully prepared in the past [32, 97, 98]. Nonetheless, none of these cells were fabricated via the novel hydrothermal method. Lin et al [78] and Zhang et al [95] experimented with the fabrication of Sb_2S_3 solar cells

using a naked TiO_2, but the performance of the prepared devices was poor (table 4.7). In both studies, a sulfur-containing material had to be deposited on top of the TiO_2 film, in order to functionalize the ETL. Due to the presence of sulfur nucleation sites, a much better Sb_2S_3 film could be formed. Our study expands these results for the alloy $Sb_2(S, Se)_3$, indicating that the absorber film prepared through the hydrothermal method cannot effectively nucleate on pristine TiO_2 due to the lack of an appropriate chemical bridge between the two materials.

4.6 TiO_2 vs CdS as a Foundation for the Hydrothermally Deposited $Sb_2(S, Se)_3$ Films

Antimony chalcogenide solar cells are usually prepared by the hydrothermal method on CdS substrates [17, 41, 43, 44], but the choice of ETL is rarely explained. Due to the poor results obtained for the solar cells based on a $TiO_2/Sb_2(S, Se)_3$ junction, some $CdS/Sb_2(S, Se)_3$ samples were prepared. Around 50 nm CdS films were deposited at the Laboratory for Nanostructured Solar Cells by the chemical bath deposition (CBD) method. Following the preparation of the CdS ETL, the antimony sulfoselenide films were prepared via the hydrothermal method and annealed at 350°C. Unfortunately, no complete solar devices were fabricated. Nonetheless, this brief study allows us to compare the effects of the two different ETLs on some properties of the hydrothermally grown antimony chalcogenide material.

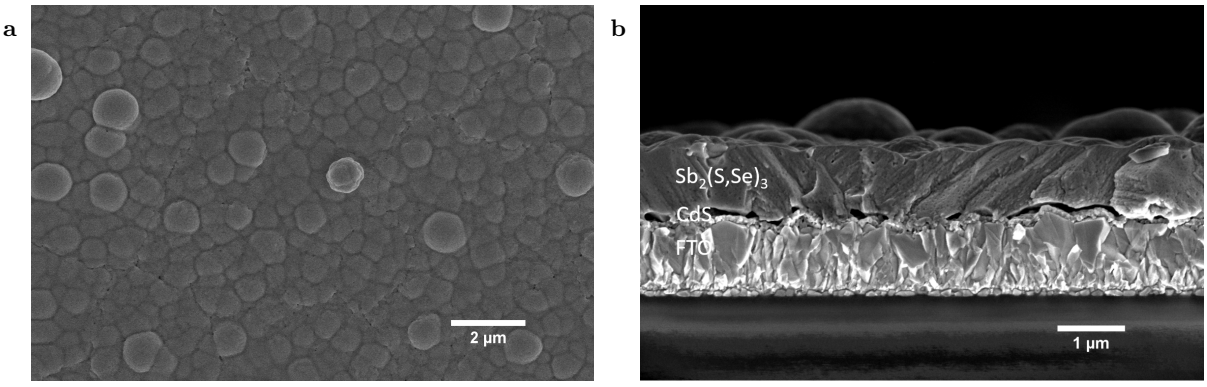

Figure 4.28: **a.** Top-view SEM images of a $CdS/Sb_2(S, Se)_3$ sample **b.** Cross-section SEM images of a $CdS/Sb_2(S, Se)_3$ sample.

Figure 4.28 shows the top-view and cross-section SEM images of the prepared $CdS/Sb_2(S, Se)_3$ samples. By comparing with figures 4.23 and 4.7 we can conclude that the CdS substrate promotes a very compact antimony sulfoselenide film. Unlike some of the tested TiO_2 layers, no voids can be detected, which eliminates the formation of the shunt paths seen in figure 4.27b.

Furthermore, the cross section analysis of the samples (figure 4.28b) shows the formation of a much flatter $Sb_2(S, Se)_3$ material, denoting the ability of the CdS layer to promote more uniform films. Average grain size was determined by measuring 100 different grains, while film thickness was obtained by measuring 20 different points in the cross-sectional imagery. Curiously, the CdS substrate seems to promote smaller grains when compared with the sprayed and sputtered $TiO_2/Sb_2(S, Se)_3$ samples, with the average size being (686.7 ± 12.3) nm. This result is likely caused by the more compact nature of the as-deposited film, with less room for grain growth, which also observed when introducing a mesporous TiO_2 layer (figure 4.23d). With respect to film thickness, the average was determined to be (581.2 ± 10.5) nm, which is almost 100 nm thinner than the film deposited on a TiO_2 substrate and annealed at 350°C (figure 4.9b).

Finally, XRD analysis of the $CdS/Sb_2(S, Se)_3$ samples was performed in order to test the influence of the substrate in crystal size and orientation. Figure 4.29a shows the diffractogram of the prepared $CdS/Sb_2(S, Se)_3$ sample. As expected, the same diffraction peaks were observed, corresponding to orthorhombic $Sb_2(S, Se)_3$.

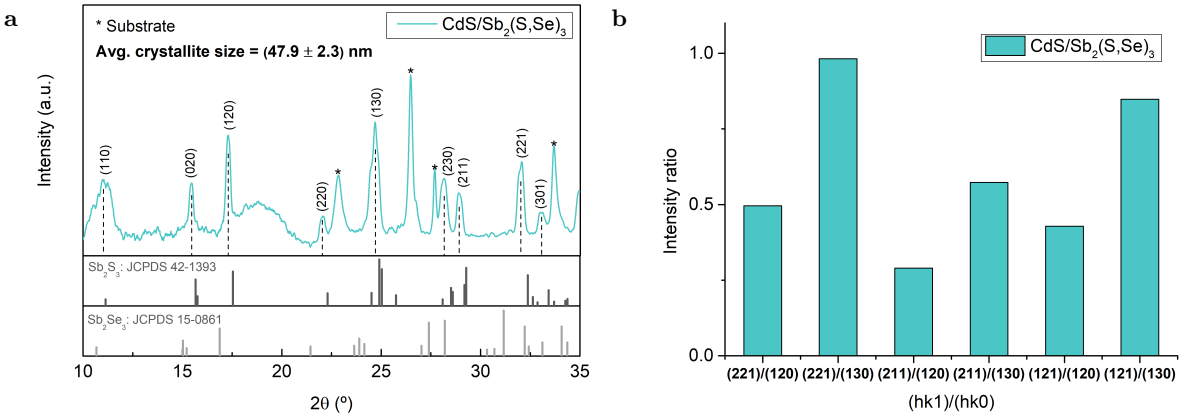

Figure 4.29: **a.** Diffractogram of the $Sb_2(S, Se)_3$ film prepared on a CdS substrate **b.** Intensity ratios for the main (hk1) and (hk0) planes of the $Sb_2(S, Se)_3$ film prepared on a CdS substrate.

Firstly, no noticeable differences were observed in crystallinity, as crystal size is mostly dependent on the annealing temperature [61]. However, by comparing the diffraction peak intensity ratios (figures 4.24c and 4.29b), we can conclude that, independently of the deposition method, the TiO_2 substrate promotes better layering of the $Sb_2(S, Se)_3$ material along the (hk1) directions, with almost a 100% increase for some (hk1)/(hk0) ratios. These results show the potential of the TiO_2 material for promoting vertical crystal growth. Hence, functionalizing a $TiO_2/Sb_2(S, Se)_3$ structure, enabling for a better quality absorber film, may be an interesting approach for future studies, as not only is the titanium dioxide a non-toxic material, but also

seems to significantly improve the orientation of the prepared $Sb_2(S, Se)_3$ films.

In summary, the CdS substrate seems to promote a better quality antimony chalcogenide film, with a substantially more flat and compact structure than the samples that use a c-TiO_2 layer as an ETL. Since the hydrothermal method largely depends on the substrate, this conclusion likely arises from the fact that the CdS layer possesses sulfur atoms, forming Sb-S bonds during the nucleation process of the $Sb_2(S, Se)_3$ material. The chemical bridge between layers will mitigate the recombination of photogenerated charge carriers at the interface, thereby facilitating a more efficient extraction. This mechanism was first proposed for a $Zn(O, S)/Sb_2S_3$ interface [78] and the conclusions can likely be extrapolated for a $CdS/Sb_2(S, Se)_3$ structure. However, the replacement of the CdS ETL in thin film solar cells is necessary due to its toxicity, and Cd-free alternatives must be sought for improved environmental compatibility. This study has shown that the cheap and abundant TiO_2 cannot be directly used as a foundation for the hydrothermal growth of antimony chalcogenides. Hence, in order to functionalize this material, further research must be conducted. For example, the introduction of a thin seed layer of a compound such as Sb_2S_3 between the ETL and absorber layer has been shown to increase the quality of the subsequently deposited film [95, 99]. An alternative may be the introduction of a non-toxic, sulfur-containing buffer layer on top of the titanium dioxide ETL, which has been shown to act as a bridge for the growth of the antimony chalcogenide material [78].

5 Conclusion and Future Work

The work developed throughout this thesis aimed to improve some parameters of the hydrothermal preparation method of antimony sulfoselenide thin films for application in PV devices. The quality of the prepared films was then assessed through a variety of characterization methods available at INL. More importantly, this work intended to act as a stepping-stone for the future development of the hydrothermal deposition method, as it is a promising but still underdeveloped technique.

Preliminary studies focused on producing a contaminant-free film. Antimony chalcogenides are oxygen sensitive materials. Ensuring an inert atmosphere during the annealing step was found to be critical, as the films quickly oxidize under high temperatures.

After obtaining a pure $Sb_2(S, Se)_3$ material, an annealing optimization study was performed. As-deposited samples were annealed at 250°C, 300°C, 350°C and 400°C, for a duration of 10 minutes. XRD results showed that the annealing process promoted the crystallization of the films. Furthermore, the samples annealed at 350°C showed a better morphology and crystal orientation, while also presenting a less steep S/Se gradient than films annealed at lower temperatures. On the other hand, increasing the annealing temperature to 400°C originates a rough film morphology, with non-optimal crystal layering.

The effects of a NaF PDT step were also studied. Results showed that the addition of NaF to as-deposited $Sb_2(S, Se)_3$ causes the etching of the sulfur-rich upper layers of the film, hence promoting a mild composition gradient and subsequent improved band alignment with the HTL layer, which is in accordance with previous studies [17]. Finally, an upshift in the Fermi energy level was observed for the NaF treated samples, which is usually associated with a V_{OC} improvement [46, 87]. These results lead us to believe that a NaF PDT should have a beneficial impact on the efficiency of $Sb_2(S, Se)_3$ solar cells. Nevertheless, more studies are needed to validate this hypothesis, focusing on the fabrication of complete PV devices.

Lastly, several deposition methods of the compact TiO_2 ETL were tested, in order to obtain a more compact $Sb_2(S,Se)_3$ film. The introduction of a mesoporous layer was also studied. Although the porous structure allowed for an uniform and compact antimony sulfoselenide material, the final solar devices suffered from poor electrical parameters and low PCE. Overall, the pristine TiO_2 layer is not an appropriate ETL for the hydrothermal growth of $Sb_2(S,Se)_3$ films, due to the lack of an appropriate chemical bridge between the two materials, resulting in the formation of shunt paths and poor charge extraction. A CdS ETL promotes a much more compact structure, due to the presence of sulfur nucleation sites, resulting in the champion $CdS/Sb_2(S,Se)_3$ solar cells reported in literature [17, 43, 44, 46].

In conclusion, the hydrothermal deposition process for the preparation of antimony chalcogenides is an inexpensive, simple and versatile method that has proven to be effective in the fabrication of high quality $Sb_2(S,Se)_3$ thin films for solar cell applications. However, this technique still heavily relies on the use of a toxic CdS layer as a substrate for the growth of the absorber layer. Hence, in order to integrate an environmentally compatible ETL, such as TiO_2, further studies must be conducted, focusing on the introduction of seed layers that can promote the growth of the antimony chalcogenides.

This study did not focus on the parameters related to the hydrothermal method itself. For example, film thickness is directly related to the duration of the hydrothermal synthesis. Usually, the reported $Sb_2(S,Se)_3$ films can have variable thicknesses, presenting good results for films as thin as 200 nm [44]. However, optimization studies for other solution-based methods, such as CBD, have reported 350 nm [100] and 500 nm [101] as an ideal thickness. Furthermore, film thickness has a direct impact on the series resistance of the solar cells [43] and few articles focusing on this parameter have been published. Hence, a film thickness optimization study may be conducted, by varying the deposition time of the hydrothermal process.

Bibliography

[1] REN23, *Renewables 2023 Global Status Report - Energy Supply*. 2023.

[2] V. M. Fthenakis, *Chapter IV-1-A - Overview of Potential Hazards*. Academic Press, third edition ed., 2018.

[3] F. ISE, "Photovoltaics report," 2023.

[4] T. D. Lee and A. U. Ebong, "A review of thin film solar cell technologies and challenges," *Renewable and Sustainable Energy Reviews*, vol. 70, pp. 1286–1297, 2017.

[5] M. Nakamura, K. Yamaguchi, Y. Kimoto, Y. Yasaki, T. Kato, and H. Sugimoto, "Cd-free $Cu(In, Ga)(Se, S)_2$ thin-film solar cell with record efficiency of 23.35%," *IEEE Journal of Photovoltaics*, vol. 9, pp. 1863–1867, 11 2019.

[6] M. A. Green, E. D. Dunlop, G. Siefer, M. Yoshita, N. Kopidakis, K. Bothe, and X. Hao, "Solar cell efficiency tables (version 61)," *Progress in Photovoltaics: Research and Applications*, vol. 31, pp. 3–16, 2023.

[7] T. Matsui, K. Maejima, A. Bidiville, H. Sai, T. Koida, T. Suezaki, M. Matsumoto, K. Saito, I. Yoshida, and M. Kondo, "High-efficiency thin-film silicon solar cells realized by integrating stable a-Si:H absorbers into improved device design," *Japanese Journal of Applied Physics*, vol. 54, p. 08KB10, 8 2015.

[8] A. Zakutayev, "Brief review of emerging photovoltaic absorbers," *Current Opinion in Green and Sustainable Chemistry*, vol. 4, pp. 8–15, 2017. 4 Novel materials for energy production and storage 2017.

[9] A. Mavlonov, T. Razykov, F. Raziq, J. Gan, J. Chantana, Y. Kawano, T. Nishimura, H. Wei, A. Zakutayev, T. Minemoto, X. Zu, S. Li, and L. Qiao, "A review of Sb_2Se_3 photovoltaic absorber materials and thin-film solar cells," 5 2020.

[10] E. Batzelis, G. Anagnostou, C. Chakraborty, and B. C. Pal, "Computation of the Lambert W function in photovoltaic modeling," 2 2019.

[11] A. Luque and S. Hegedus, *Handbook of photovoltaic science and engineering*. John Wiley & Sons, 2011.

[12] B. Ríos-Ramirez and P. K. Nair, "On the stability of operation of antimony sulfide selenide thin film solar cells under solar radiation," *physica status solidi (a)*, vol. 215, p. 1800479, 12 2018.

[13] K. Zeng, D.-J. Xue, and J. Tang, "Antimony selenide thin-film solar cells," *Semiconductor Science and Technology*, vol. 31, p. 063001, 6 2016.

[14] R. Kondrotas, C. Chen, and J. Tang, "Sb_2S_3 solar cells," *Joule*, vol. 2, pp. 857–878, 5 2018.

[15] S. Barthwal, R. Kumar, and S. Pathak, "Present status and future perspective of antimony chalcogenide (Sb_2X_3) photovoltaics," *ACS Applied Energy Materials*, vol. 5, pp. 6545–6585, 6 2022. doi: 10.1021/acsaem.2c00420.

[16] Y. Zhou, M. Leng, Z. Xia, J. Zhong, H. Song, X. Liu, Bo, J. Zhang, J. Chen, K. Zhou, J. Han, Y. Cheng, and J. Tang, "Solution-processed antimony selenide heterojunction solar cells," *Advanced Energy Materials*, vol. 4, p. 1301846, 6 2014.

[17] Y. Zhao, S. Wang, C. Jiang, C. Li, P. Xiao, R. Tang, J. Gong, G. Chen, T. Chen, J. Li, and X. Xiao, "Regulating energy band alignment via alkaline metal fluoride assisted solution post-treatment enabling $Sb_2(S,Se)_3$ solar cells with 10.7% efficiency," 2021.

[18] A. Polman, M. Knight, E. C. Garnett, B. Ehrler, and W. C. Sinke, "Photovoltaic materials: Present efficiencies and future challenges," *Science*, vol. 352, p. aad4424, 2016.

[19] C. Chen, W. Li, Y. Zhou, C. Chen, M. Luo, X. Liu, K. Zeng, B. Yang, C. Zhang, J. Han, and J. Tang, "Optical properties of amorphous and polycrystalline Sb_2Se_3 thin films prepared by thermal evaporation," *Applied Physics Letters*, vol. 107, p. 043905, 7 2015.

[20] Y. Zhou, L. Wang, S. Chen, S. Qin, X. Liu, J. Chen, D. Xue, M. Luo, Y. Cao, Y. Cheng, E. Sargent, and J. Tang, "Thin-film Sb_2Se_3 photovoltaics with oriented one-dimensional ribbons and benign grain boundaries," *Nature Photonics*, vol. 9, pp. 409–415, 1 2015.

[21] L. Guo, B. Zhang, Y. Qin, D. Li, L. Li, X. Qian, and F. Yan, "Tunable quasi-one-dimensional ribbon enhanced light absorption in Sb_2Se_3 thin-film solar cells grown by close-space sublimation," *Solar RRL*, vol. 2, p. 1800128, 10 2018.

[22] M. Saliba, J.-P. Correa-Baena, C. M. Wolff, M. Stolterfoht, N. Phung, S. Albrecht, D. Neher, and A. Abate, "How to make over 20% efficient perovskite solar cells in regular (n–i–p) and inverted (p–i–n) architectures," *Chemistry of Materials*, vol. 30, pp. 4193–4201, 7 2018. doi: 10.1021/acs.chemmater.8b00136.

[23] H. Lei, J. Chen, Z. Tan, and G. Fang, "Review of recent progress in antimony chalcogenide-based solar cells: materials and devices," *Solar Rrl*, vol. 3, no. 6, p. 1900026, 2019.

[24] K. Bruening, B. Dou, J. Simonaitis, Y.-Y. Lin, M. F. A. M. van Hest, and C. J. Tassone, "Scalable fabrication of perovskite solar cells to meet climate targets," *Joule*, vol. 2, pp. 2464–2476, 2018.

[25] J. Zhang, R. Kondrotas, S. Lu, C. Wang, C. Chen, and J. Tang, "Alternative back contacts for Sb_2Se_3 solar cells," *Solar Energy*, vol. 182, pp. 96–101, 2019.

[26] F. D. B. Sánchez, M. T. S. Nair, and P. K. Nair, "Optimum chemical composition of antimony sulfide selenide for thin film solar cells," *Applied Surface Science*, vol. 454, pp. 305–312, 2018.

[27] D.-B. Li, X. Yin, C. R. Grice, L. Guan, Z. Song, C. Wang, C. Chen, K. Li, A. J. Cimaroli, R. A. Awni, D. Zhao, H. Song, W. Tang, Y. Yan, and J. Tang, "Stable and efficient CdS/Sb_2Se_3 solar cells prepared by scalable close space sublimation," *Nano Energy*, vol. 49, pp. 346–353, 2018.

[28] C. Anrango-Camacho, K. Pavón-Ipiales, B. A. Frontana-Uribe, and A. Palma-Cando, "Recent advances in hole-transporting layers for organic solar cells," *Nanomaterials*, vol. 12, p. 443, 1 2022.

[29] F. M. Rombach, S. A. Haque, and T. J. Macdonald, "Lessons learned from spiro-ometad and ptaa in perovskite solar cells," *Energy Environmental Science*, vol. 14, pp. 5161–5190, 2021.

[30] G. Tumen-Ulzii, T. Matsushima, and C. Adachi, "Mini-review on efficiency and stability of perovskite solar cells with Spiro-OMeTAD hole transport layer: Recent progress and perspectives," *Energy Fuels*, vol. 35, pp. 18915–18927, 12 2021. doi: 10.1021/acs.energyfuels.1c02190.

[31] Mamta, K. K. Maurya, and V. N. Singh, "Enhancing the performance of an Sb_2Se_3-based solar cell by dual buffer layer," *Sustainability*, vol. 13, 2021.

[32] Y. Wang, R. Tang, L. Huang, C. Qian, W. Lian, C. Zhu, and T. Chen, "Post-treatment of TiO_2 film enables high-quality Sb_2Se_3 film deposition for solar cell applications," *ACS Applied Materials Interfaces*, vol. 14, pp. 33181–33190, 2022. PMID: 35820105.

[33] Y. Zeng, J. Huang, J. Li, K. Sun, U. A. Shah, H. Deng, X. Zhang, C. Sha, C. Qian, H. Song, and X. Hao, "Comparative study of TiO_2 and CdS as the electron transport layer for Sb_2S_3 solar cells," *Solar RRL*, vol. 6, p. 2200435, 10 2022.

[34] F. U. Hamelmann, "Transparent conductive oxides in thin film photovoltaics," *Journal of Physics: Conference Series*, vol. 559, p. 012016, 11 2014.

[35] A. Way, J. Luke, A. D. Evans, Z. Li, J.-S. Kim, J. R. Durrant, H. K. H. Lee, and W. C. Tsoi, "Fluorine doped tin oxide as an alternative of indium tin oxide for bottom electrode of semi-transparent organic photovoltaic devices," *AIP Advances*, vol. 9, p. 085220, 8 2019.

[36] N. Spalatu, R. Krautmann, A. Katerski, E. Karber, R. Josepson, J. Hiie, I. O. Acik, and M. Krunks, "Screening and optimization of processing temperature for Sb_2Se_3 thin film growth protocol: Interrelation between grain structure, interface intermixing and solar cell performance," *Solar Energy Materials and Solar Cells*, vol. 225, p. 111045, 2021.

[37] V. Akshay, S. Benny, and S. V. Bhat, "Solution-processed antimony chalcogenides based thin film solar cells: A brief overview of recent developments," *Solar Energy*, vol. 241, pp. 728–737, 7 2022.

[38] Z. Li, X. Liang, G. Li, H. Liu, H. Zhang, J. Guo, J. Chen, K. Shen, X. San, W. Yu, R. E. I. Schropp, and Y. Mai, "9.2%-efficient core-shell structured antimony selenide nanorod array solar cells," *Nature Communications*, vol. 10, p. 125, 2019.

[39] P. Fan, G.-J. Chen, S. Chen, Z.-H. Zheng, M. Azam, N. Ahmad, Z.-H. Su, G.-X. Liang, X.-H. Zhang, and Z.-G. Chen, "Quasi-vertically oriented Sb_2Se_3 thin-film solar cells with open-circuit voltage exceeding 500 mv prepared via close-space sublimation and selenization," *ACS Applied Materials Interfaces*, vol. 13, pp. 46671–46680, 10 2021. doi: 10.1021/acsami.1c13223.

[40] X. Wen, C. Chen, S. Lu, K. Li, R. Kondrotas, Y. Zhao, W. Chen, L. Gao, C. Wang, J. Zhang, G. Niu, and J. Tang, "Vapor transport deposition of antimony selenide thin film solar cells with 7.6% efficiency," *Nature Communications*, vol. 9, p. 2179, 2018.

[41] D. Liu, R. Tang, Y. Ma, C. Jiang, W. Lian, G. Li, W. Han, C. Zhu, and T. Chen, "Direct hydrothermal deposition of antimony triselenide films for efficient planar heterojunction solar cells," *ACS Applied Materials and Interfaces*, vol. 13, pp. 18856–18864, 4 2021.

[42] S. Li, H. Shen, J. Chen, Y. Jiang, L. Sun, A. Raza, and Y. Xu, "Effect of selenization temperature on the properties of Sb_2Se_3 thin films and solar cells by two-step method," *Journal of Materials Science: Materials in Electronics*, vol. 30, pp. 19871–19879, 11 2019.

[43] R. Tang, X. Wang, W. Lian, J. Huang, Q. Wei, M. Huang, Y. Yin, C. Jiang, S. Yang, G. Xing, S. Chen, C. Zhu, X. Hao, M. A. Green, and T. Chen, "Hydrothermal deposition of antimony selenosulfide thin films enables solar cells with 10% efficiency," *Nature Energy*, vol. 5, pp. 587–595, 8 2020.

[44] X. Chen, B. Che, Y. Zhao, S. Wang, H. Li, J. Gong, G. Chen, T. Chen, X. Xiao, and J. Li, "Solvent-assisted hydrothermal deposition approach for highly-efficient $Sb_2(S, Se)_3$ thin-film solar cells," *Advanced Energy Materials*, 4 2023.

[45] M. M. Nicolás-Marín, J. R. González-Castillo, O. Vigil-Galán, and M. Courel, "The state of the art of $Sb_2(S, Se)_3$ thin film solar cells: current progress and future prospect," *Journal of Physics D: Applied Physics*, vol. 55, p. 303001, 7 2022.

[46] X. Wang, R. Tang, C. Jiang, W. Lian, H. Ju, G. Jiang, Z. Li, C. Zhu, and T. Chen, "Manipulating the electrical properties of $Sb_2(S, Se)_3$ film for high-efficiency solar cell," *Advanced Energy Materials*, vol. 10, p. 2002341, 10 2020.

[47] "Influence of alkali element post-deposition treatment on the performance of the CIGS solar cells on flexible stainless steel substrates," *Materials Letters*, vol. 302, p. 130410, 2021.

[48] P. Jackson, D. Hariskos, R. Wuerz, O. Kiowski, A. Bauer, T. M. Friedlmeier, and M. Powalla, "Properties of $Cu(In, Ga)Se_2$ solar cells with new record efficiencies up to 21.7%," *physica status solidi (RRL) - Rapid Research Letters*, vol. 9, pp. 28–31, 1 2015.

[49] P. Jackson, R. Wuerz, D. Hariskos, E. Lotter, W. Witte, and M. Powalla, "Effects of heavy alkali elements in $Cu(In, Ga)Se_2$ solar cells with efficiencies up to 22.6%," *physica status solidi (RRL) – Rapid Research Letters*, vol. 10, pp. 583–586, 8 2016.

[50] J. Dong, Y. Liu, Z. Wang, and Y. Zhang, "Boosting v_{OC} of antimony chalcogenide solar cells: A review on interfaces and defects," *Nano Select*, vol. 2, pp. 1818–1848, 10 2021.

[51] Y. C. Choi, D. U. Lee, J. H. Noh, E. K. Kim, and S. I. Seok, "Highly improved Sb_2S_3 sensitized-inorganic–organic heterojunction solar cells and quantification of traps by deep-level transient spectroscopy," *Advanced Functional Materials*, vol. 24, pp. 3587–3592, 2014.

[52] T. Fukumoto, T. Moehl, Y. Niwa, M. K. Nazeeruddin, M. Grätzel, and L. Etgar, "Effect of interfacial engineering in solid-state nanostructured Sb_2S_3 heterojunction solar cells," *Adv. Energy Mater*, vol. 3, no. 1, pp. 29–33, 2013.

[53] Q. Ye, Y. Xu, W. Chen, S. Yang, J. Zhu, and J. Weng, "Enhanced photovoltaic performance of Sb_2S_3-sensitized solar cells through surface treatments," *Applied Surface Science*, vol. 440, pp. 294–299, 2018.

[54] C. Chen, K. Li, S. Chen, L. Wang, S. Lu, Y. Liu, D. Li, H. Song, and J. Tang, "Efficiency improvement of Sb_2Se_3 solar cells via grain boundary inversion," *ACS Energy Letters*, vol. 3, pp. 2335–2341, 10 2018. doi: 10.1021/acsenergylett.8b01456.

[55] C. Gao, J. Huang, H. Li, K. Sun, Y. Lai, M. Jia, L. Jiang, and F. Liu, "Fabrication of Sb_2S_3 thin films by sputtering and post-annealing for solar cells," *Ceramics International*, vol. 45, pp. 3044–3051, 2 2019.

[56] F. Haque, N. K. Elumalai, M. Wright, M. A. Mahmud, D. Wang, M. B. Upama, C. Xu, and A. Uddin, "Annealing induced microstructure engineering of antimony tri-selenide thin films," *Materials Research Bulletin*, vol. 99, pp. 232–238, 3 2018.

[57] P. S. Pawar, R. Nandi, K. R. E. Neerugatti, J. Y. Cho, and J. Heo, "Hydrothermal growth of Sb_2S_3 thin films on molybdenum for solar cell applications: Effect of post-deposition annealing," *Journal of Alloys and Compounds*, vol. 898, 3 2022.

[58] A. Shongalova, M. R. Correia, B. Vermang, J. M. V. Cunha, P. M. P. Salomé, and P. A. Fernandes, "On the identification of Sb_2Se_3 using raman scattering," *MRS Communications*, vol. 8, pp. 865–870, 2018.

[59] M. B. Costa, F. W. de Souza Lucas, and L. H. Mascaro, "Thermal treatment effects on electrodeposited Sb_2Se_3 photovoltaic thin films," *ChemElectroChem*, vol. 4, pp. 2507–2514, 10 2017.

[60] M. Kamruzzaman, C. Liu, A. K. M. F. U. Islam, and J. A. Zapien, "A comparative study on the electronic and optical properties of Sb_2Se_3 thin film," *Semiconductors*, vol. 51, pp. 1615–1624, 12 2017.

[61] S. Rijal, A. Adhikari, R. A. Awni, C. Xiao, D.-B. Li, B. Dokken, A. Ellingson, E. Flores, S. S. Bista, D. Pokhrel, S. Neupane, R. E. Irving, A. B. Phillips, K. Jungjohann, C.-S. Jiang, M. Al-Jassim, R. J. Ellingson, Z. Song, and Y. Yan, "Post-annealing treatment on hydrothermally grown antimony sulfoselenide thin films for efficient solar cells," *Solar RRL*, vol. 7, p. 2201009, 2 2023.

[62] A. Möllmann, D. Gedamu, P. Vivo, R. Frohnhoven, D. Stadler, T. Fischer, I. Ka, M. Steinhorst, R. Nechache, F. Rosei, S. G. Cloutier, T. Kirchartz, and S. Mathur, "Highly compact TiO_2 films by spray pyrolysis and application in perovskite solar cells," *Advanced Engineering Materials*, vol. 21, p. 1801196, 4 2019.

[63] S. Nandy and K. H. Chae, *17 - Chemical synthesis of ferrite thin films*, pp. 309–334. Woodhead Publishing, 2023.

[64] D. M. Mattox, *Chapter 1 - Introduction*, pp. 1–24. William Andrew Publishing, second edition ed., 2010.

[65] M. Dawber, *2 - Sputtering techniques for epitaxial growth of complex oxides*, pp. 31–45. Woodhead Publishing, 2015.

[66] A. Bashir, T. I. Awan, A. Tehseen, M. B. Tahir, and M. Ijaz, *Chapter 3 - Interfaces and surfaces*, pp. 51–87. Elsevier, 2020.

[67] P. Wurfel and U. Wurfel, *Physics of solar cells : from basic principles to advanced concepts*. Wiley-VCH, 2009.

[68] E. Thomas, "Crystal growth and the search for highly correlated ternary intermetallic antimonides and stannides," 2 2006.

[69] D. Negi, R. Shyam, and S. R. Nelamarri, "Role of annealing temperature on structural and optical properties of $MgTiO_3$ thin films," *Materials Letters: X*, vol. 11, p. 100088, 2021.

[70] B. Yang, D.-J. Xue, M. Leng, J. Zhong, L. Wang, H. Song, Y. Zhou, and J. Tang, "Hydrazine solution processed Sb_2S_3, Sb_2Se_3 and $Sb_2(S_{1x}Se_x)_3$ film: molecular precursor identification, film fabrication and band gap tuning," *Scientific Reports*, vol. 5, p. 10978, 6 2015.

[71] D. Abou-Ras, M. Nichterwitz, M. J. Romero, and S. S. Schmidt, *Electron Microscopy on Thin Films for Solar Cells*. John Wiley Sons, Ltd, 2011.

[72] J. Hamuyuni, M. O. Daramola, and O. O. Oluwasina, *Energy-Dispersive X-Ray Spectroscopy: Theory and Application in Engineering and Science*. John Wiley Sons, Ltd, 2017.

[73] S. J. B. Reed, *Electron probe microanalysis*. Springer US, 1995.

[74] V. Hoffmann, D. Klemm, V. Efimova, C. Venzago, A. A. Rockett, T. Wirth, T. Nunney, C. A. Kaufmann, and R. Caballero, *Elemental Distribution Profiling of Thin Films for Solar Cells*. Wiley, 3 2011.

[75] P. Makuła, M. Pacia, and W. Macyk, "How to correctly determine the band gap energy of modified semiconductor photocatalysts based on uv–vis spectra," *The Journal of Physical Chemistry Letters*, vol. 9, pp. 6814–6817, 12 2018.

[76] Z. Chen and T. Jaramillo, "The use of uv-visible spectroscopy to measure the band gap of a semiconductor," *Department of Chemical Engineering, Stanford University Edited by Bruce Brunschwig*, vol. 9, p. 19, 2017.

[77] Y. Lu, K. Li, X. Yang, S. Lu, S. Li, J. Zheng, L. Fu, C. Chen, and J. Tang, "Htl-free $Sb_2(S, Se)_3$ solar cells with an optimal detailed balance band gap," *ACS Applied Materials Interfaces*, vol. 13, pp. 46858–46865, 10 2021.

[78] W. Lin, W.-T. Guo, L. Yao, J. Li, L. Lin, J.-M. Zhang, S. Chen, and G. Chen, "Zn(O, S) buffer layer for in situ hydrothermal Sb_2S_3 planar solar cells," *ACS Applied Materials Interfaces*, vol. 13, pp. 45726–45735, 2021. PMID: 34520174.

[79] Živković, N. Štrbac, D. Živković, D. Grujičić, and B. Boyanov, "Kinetics and mechanism of Sb_2S_3 oxidation process," *Thermochimica Acta*, vol. 383, pp. 137–143, 2002.

[80] H. Kou, W. Li, X. Zhang, N. Xu, X. Zhang, J. Shao, J. Ma, Y. Deng, and Y. Li, "Temperature-dependent coefficient of surface tension prediction model without arbitrary parameters," *Fluid Phase Equilibria*, vol. 484, pp. 53–59, 2019.

[81] W. Wang, X. Wang, G. Chen, L. Yao, X. Huang, T. Chen, C. Zhu, S. Chen, Z. Huang, and Y. Zhang, "Over 6fabricated via in situ hydrothermal growth and postselenization," *Advanced Electronic Materials*, vol. 5, p. 1800683, 2019.

[82] F. Urbach, "The long-wavelength edge of photographic sensitivity and of the electronic absorption of solids," *Physical Review*, vol. 92, pp. 1324–1324, 12 1953.

[83] F. Toshiaki, K. Koichi, T. Ken, and O. Toshiatsu, "The fundamental absorption edge and electronic structure in Sb_2S_3," *Journal of the Physical Society of Japan*, vol. 56, pp. 3734–3739, 1987.

[84] L. Yu, R. S. Kokenyesi, D. A. Keszler, and A. Zunger, "Inverse design of high absorption thin-film photovoltaic materials," *Advanced Energy Materials*, vol. 3, pp. 43–48, 2013.

[85] E. Gnenna, N. Khemiri, M. I. Alonso, and M. Kanzari, "Optical characterization of Sb_2S_3 vacuum annealed films by uv–vis–nir spectroscopy and spectroscopic ellipsometry: Determining the refractive index and the optical constants," *Optik*, vol. 268, p. 169740, 2022.

[86] R. H. Arntson, F. W. Dickson, and G. Tunell, "Stibnite (Sb_2S_3) solubility in sodium sulfide solutions," *Science*, vol. 153, pp. 1673–1674, 1966.

[87] C. Wang, S. Lu, S. Li, S. Wang, X. Lin, J. Zhang, R. Kondrotas, K. Li, C. Chen, and J. Tang, "Efficiency improvement of flexible Sb_2Se_3 solar cells with non-toxic buffer layer via interface engineering," *Nano Energy*, vol. 71, p. 104577, 2020.

[88] S. Z. Haider, H. Anwar, and M. Wang, "Theoretical device engineering for high-performance perovskite solar cells using cuscn as hole transport material boost the efficiency above 25vol. 216, p. 1900102, 6 2019.

[89] Y. Wang, L. Shasha, and Z. Li, "Review on incorporation of alkali elements and their effects in $Cu(In, Ga)Se_2$ solar cells," *Journal of Materials Science Technology*, vol. 96, 8 2021.

[90] Z. Wang, J. Fang, Y. Mi, X. Zhu, H. Ren, X. Liu, and Y. Yan, "Enhanced performance of perovskite solar cells by ultraviolet-ozone treatment of mesoporous TiO_2," *Applied Surface Science*, vol. 436, pp. 596–602, 2018.

[91] J. Li, L. Huang, J. Hou, X. Wu, J. Niu, G. Chen, J. Gong, Y. Kong, and X. Xiao, "Effects of substrate orientation and solution movement in chemical bath deposition on $Zn(O, S)$ buffer layer and $Cu(In, Ga)Se_2$ thin film solar cells," *Nano Energy*, vol. 58, pp. 427–436, 2019.

[92] C. Wang, D. Zhuang, M. Zhao, Y. Li, L. Dong, H. Wang, J. Wei, and Q. Gong, "Surface modifications of CIGS absorbers and their effects on performances of CIGS solar cells," *Ceramics International*, vol. 47, pp. 34508–34513, 2021.

[93] R. K. Battula, G. Veerappan, P. Bhyrappa, C. Sudakar, and E. Ramasamy, "Stability of $MAPbI_3$ perovskite grown on planar and mesoporous electron-selective contact by inverse temperature crystallization," *RSC Advances*, vol. 10, pp. 30767–30775, 2020.

[94] N.-T. Nguyen, "Chapter 4 - fabrication technologies," 2012.

[95] L. Zhang, W. Lian, X. Zhao, Y. Yin, T. Chen, and C. Zhu, "Sb2s3 seed-mediated growth of low-defect Sb_2S_3 on a TiO_2 substrate for efficient solar cells," *ACS Applied Energy Materials*, vol. 3, pp. 12417–12422, 12 2020.

[96] L. Che, Y. Guo, C. Liao, X. Sheng, Z. Zeng, Z. Liu, and C. Cai, "One-step fabrication of effective mesoporous layer consisted of self-assembled MgO/TiO_2 core/shell nanoparticles for mesostructured perovskite solar cells," *Materials Research Express*, vol. 6, p. 086440, 5 2019.

[97] C. Wu, W. Lian, L. Zhang, H. Ding, C. Jiang, Y. Ma, W. Han, Y. Li, J. Zhu, T. Chen, and C. Zhu, "Water additive enhanced solution processing of alloy $Sb_2(S_{1-x}Se_x)_3$-based solar cells," *Solar RRL*, vol. 4, p. 1900582, 2020.

[98] Y. Zhang, J. Li, G. Jiang, W. Liu, S. Yang, C. Zhu, and T. Chen, "Selenium-graded $Sb_2(S_{1x}Se_x)_3$ for planar heterojunction solar cell delivering a certified power conversion efficiency of 5.71

[99] Y. Deng, H. Liu, H. Wang, Y. Song, W. Li, L. Zhu, X. Xie, S. Xiao, and H. Chen, "Carbon-based $Sb_2(S, Se)_3$ solar cells," *Inorganics*, vol. 11, p. 159, 4 2023.

[100] S. Li, S. Lu, Y. Lu, J. Xue, K. Li, C. Chen, and J. Tang, "Efficient $Sb_2(S, Se)_3$ solar cells via monitorable chemical bath deposition," *Journal of Materials Chemistry A*, vol. 10, pp. 11625–11635, 2022.

[101] J. Zhao, X. Li, J. Lin, X. Zhao, M. Ishaq, S. Chen, Z. Zheng, Z. Su, X. Zhang, and G. Liang, "Unveiling the influence mechanism of absorber thickness on efficient $Sb_2(S, Se)_3$ solar cells through controlled chemical bath deposition," *Available at SSRN 4532473*.

Appendix A

Supporting Figures

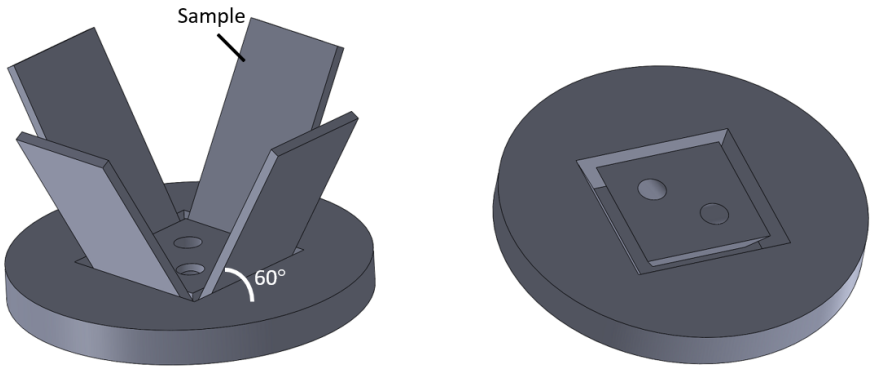

Figure A.1: Schematics of the hydrothermal support designed at INL by Vitor Lopes, allowing the preparation of 4 samples at a time.

a

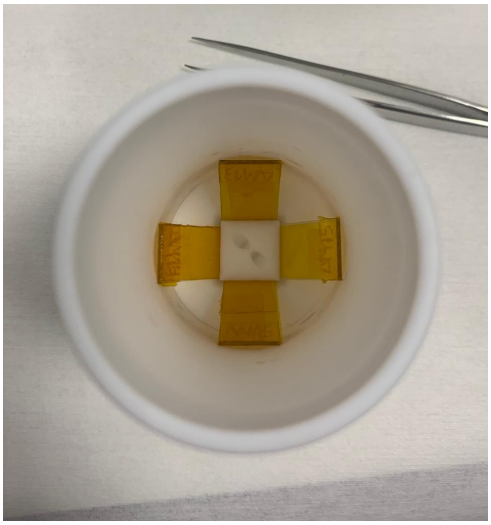

b

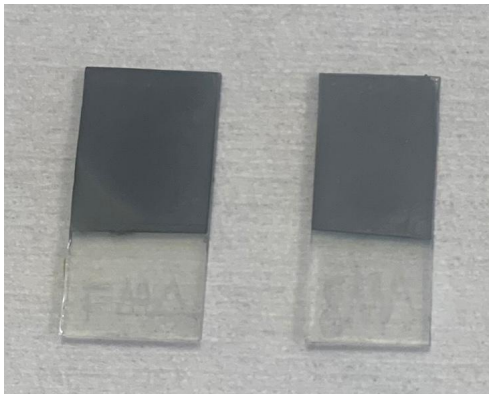

Figure A.2: **a.** Image of the teflon aligner with the substrates prepared for the hydrothermal process. **b.** $Sb_2(S,Se)_3$ samples on a sprayed TiO_2 substrate after the hydrothermal synthesis.

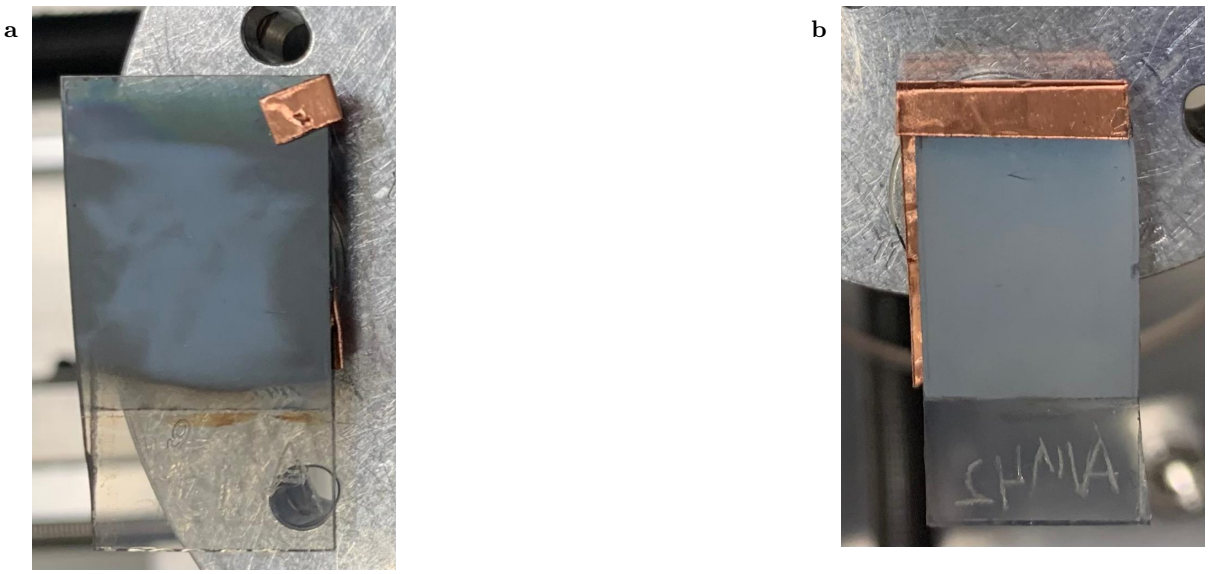

Figure A.3: Final $Sb_2(S, Se)_3$ samples on a **a.** spin-coated c-TiO_2 layer **b.** spin-coated c-TiO_2 + mesoporous TiO_2 substrate.

Appendix B

RTP oven repair

Initial studies of the annealing process of the $Sb_2(S, Se)_3$ material determined that the ultimate pressure achieved during pumping by the Rapid Thermal Processing (RTP) oven was not sufficient, stabilizing at around 2 mbar. Hence, a leak test using an helium detector was performed. While in pumping, helium gas was injected in the suspected leak points and a mass spectrometer was used to detect the presence of helium inside the chamber. The main leak points were identified and can be seen in figure B.1a. The presence of leaks were attributed to the faulty generic fittings, not appropriate for vacuum settings. The fittings were replaced by 1/4 inch male connectors fabricated by Swagelok (figure B.1b). The resulting changes allowed for a 20 fold improvement of vacuum conditions, with ultimate pressures achieving 0.1 mbar.

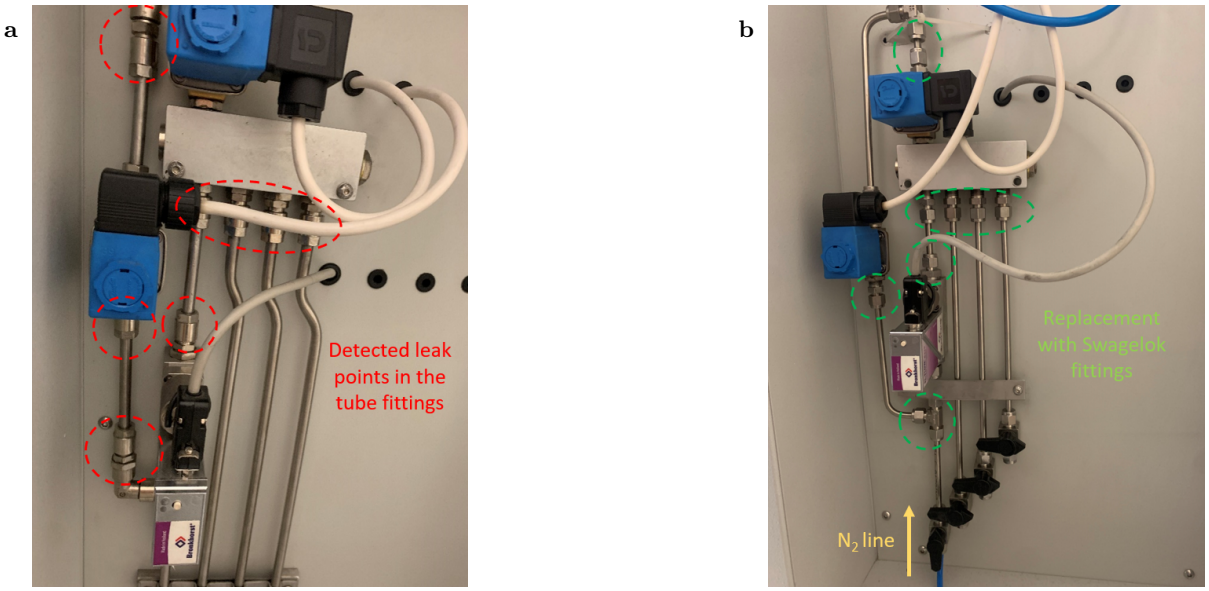

Figure B.1: **a.** Image of the gas feeding lines of the RTP oven with the identification of the main leak points. **b.** Image of the gas feeding lines of the RTP oven after replacement of the faulty fittings with vacuum appropriate Swagelok fittings.